



Publicly Accessible Penn Dissertations


Summer 8-12-2011

Energy Transport and Conversion in Semiconductor Nanocrystal Solids

Dong Kyun Ko

University of Pennsylvania, dkyun@seas.upenn.edu

Follow this and additional works at: <http://repository.upenn.edu/edissertations>

 Part of the [Nanotechnology Fabrication Commons](#), [Power and Energy Commons](#), and the [Semiconductor and Optical Materials Commons](#)

Recommended Citation

Ko, Dong Kyun, "Energy Transport and Conversion in Semiconductor Nanocrystal Solids" (2011). *Publicly Accessible Penn Dissertations*. 360.

<http://repository.upenn.edu/edissertations/360>

This paper is posted at ScholarlyCommons. <http://repository.upenn.edu/edissertations/360>

For more information, please contact libraryrepository@pobox.upenn.edu.

Energy Transport and Conversion in Semiconductor Nanocrystal Solids

Abstract

Solids constructed with single and multicomponent nanocrystal represent an exciting new form of condensed matter, as they can potentially capture not only the quantum features of the individual building blocks but also novel collective properties that arise from coupling of nanocrystal components. In this thesis, measurement and interpretation of temperature-dependent thermopower in semiconductor nanocrystal solids are used to elucidate the Fermi energy level and the density of state distribution. The physical understating of temperature dependence of thermopower is, in turn, utilized to develop a powerful tool with which to monitor doping in PbTe nanocrystal solids with different concentrations of Ag₂Te nanocrystal dopants. Combining the temperature-dependent thermopower and electrical conductivity measurements provides a unique electronic spectroscopy tool with which to reveal the carrier distribution and dynamics in semiconductor nanocrystal solids.

Degree Type

Dissertation

Degree Name

Doctor of Philosophy (PhD)

Graduate Group

Materials Science & Engineering

First Advisor

Christopher B. Murray

Keywords

semiconductor nanocrystals, quantum dots, artificial atoms, artificial solids, nanocrystal solids, thermopower, Seebeck coefficient

Subject Categories

Materials Science and Engineering | Nanotechnology Fabrication | Power and Energy | Semiconductor and Optical Materials

ENERGY TRANSPORT AND CONVERSION IN SEMICONDUCTOR NANOCRYSTAL SOLIDS

Dong-Kyun, Ko

A DISSERTATION

in

MATERIALS SCIENCE AND ENGINEERING

Presented to the Faculties of the University of Pennsylvania in Partial
Fulfillment of the Requirements for the Degree of Doctor of Philosophy

2011

Christopher B. Murray, Richard Perry University Professor of Chemistry and
Materials Science and Engineering

Supervisor of Dissertation

Russell J. Composto, Professor of Materials Science and Engineering, Bioengineering,
Chemical and Biomolecular Engineering

Graduate Group Chairperson

Dissertation Committee

Cherie R. Kagan, Professor of Electrical and Systems Engineering, Materials Science and
Engineering, and Chemistry

Peter K. Davies, Professor and Chair of Materials Science and Engineering

Jennifer Lukes, Associate Professor and Graduate Group Chair of Mechanical Engineering
and Applied Mechanics

**ENERGY TRANSPORT AND CONVERSION IN
SEMICONDUCTOR NANOCRYSTAL SOLIDS**

COPYRIGHT

2011

Dong-Kyun, Ko

To my wife & my parents

Acknowledgements

It is my pleasure to acknowledge those who helped me along the way to completion of this thesis. The foremost appreciation goes to Professor Chris Murray: a pioneer who has invented this area and a teacher who has trained me as a thinker, a scientist, and an engineer. I am also grateful to my fellow labmates (Tom, Danielle, Vicky, David, TJ, Xing & Jun Chen, and Yu-wen, to name a few) who have nourished my mind with daily joy, laughter, and beyond. I have to mention all the opportunities and benefits provided from my collaborators have made me who I am today. Most importantly, I like to tell my parents: I want to thank all that you have given me, I am a chip off the old block. There are lists and lists of people in my mind I am greatly indebt to and will not forget to personally thank each one of them till my last day in Philly. Lastly, my sincere acknowledgement goes to my thesis committee for their scientific insight and supportive mentoring.

“Learning is finding out what you already know.

Doing is demonstrating that you know it.

Teaching is reminding others that they know just as well as you.

You are all learners, doers, teachers.”

-Richard Bach

Illusions: The Adventures of a Reluctant Messiah

ABSTRACT

**ENERGY TRANSPORT AND CONVERSION IN
SEMICONDUCTOR NANOCRYSTAL SOLIDS**

Dong-Kyun, Ko

Thesis advisor: Dr. Christopher B. Murray

Solids constructed with single and multicomponent nanocrystal represent an exciting new form of condensed matter, as they can potentially capture not only the quantum features of the individual building blocks but also novel collective properties that arise from coupling of nanocrystal components. In this thesis, measurement and interpretation of temperature-dependent thermopower in semiconductor nanocrystal solids are used to elucidate the Fermi energy level and the density of state distribution. The physical understating of temperature dependence of thermopower is, in turn, utilized to develop a powerful tool with which to monitor doping in PbTe nanocrystal solids with different concentrations of Ag₂Te nanocrystal dopants. Combining the temperature-dependent thermopower and electrical conductivity measurements provides a unique electronic spectroscopy tool with which to reveal the carrier distribution and dynamics in semiconductor nanocrystal solids.

Contents

1. Semiconductor nanocrystal solids.....	1
1.1 Introduction.....	1
1.2 Semiconductor nanocrystals as artificial atoms.....	4
1.3 Artificial solids constructed from semiconductor nanocrystals.....	8
1.4 Nanostructured thermoelectrics.....	19
1.5 Thesis overview.....	29
2. Electronic conduction and thermopower in semiconductor nanocrystal solids.....	35
2.1 Introduction.....	35
2.2 Physics of amorphous materials.....	36
2.3 Measurement of electrical and thermoelectric properties.....	41
2.4 Conclusion.....	46
3. Synthesis and characterization of metal-chalcogenide nanocrystals.....	49
3.1 Introduction.....	49
3.2 Synthesis and characterization of lead chalcogenide nanocrystals.....	50
3.3 Synthesis and characterization of silver telluride nanocrystals.....	55
3.4 X-ray structural characterization techniques.....	63
3.5 Conclusion.....	78
4. Temperature-dependent thermopower in PbTe nanocrystal solids.....	83
4.1 Introduction.....	83
4.2 Experimental details.....	84
4.3 Fermi energy level in PbTe nanocrystal solids.....	87
4.4 Density of states distribution in PbTe nanocrystal solids.....	99
4.5 Conclusion.....	104
5. PbTe nanocrystal solids doped with Ag₂Te artificial atoms.....	108
5.1 Introduction.....	108
5.2 Experimental details.....	110
5.3 Electronic spectroscopy of PbTe nanocrystal solids.....	112
5.4 Electronic spectroscopy of Ag ₂ Te nanocrystal solids.....	116
5.5 PbTe nanocrystal solids with Ag ₂ Te nanocrystal dopants.....	118

5.6 Conclusion.....	124
6. Solution-processable nanocomposites with enhanced thermopower.....	127
6.1 Introduction.....	127
6.2 Experimental details.....	128
6.3 Pt-Sb ₂ Te ₃ nanocomposite with enhanced thermoelectric power factor and carrier energy filtering.....	132
6.4 Conclusion.....	140
7. Conclusion and future work.....	144
7.1 Conclusion.....	144
7.2 Future work: Electronic contributions to the thermal conductivity.....	146

List of Tables

1.1	Typical thermopower values of various metals and semiconductors	24
4.1	Summary of samples prepared for temperature-dependent thermopower measurements.....	94
5.1	Thermopower, electrical conductivity and their activation energies PbTe nanocrystal solid doped with Ag ₂ Te nanocrystals.....	124
6.1	van der Pauw resistivity, Hall effect, and thermopower measurements on Sb ₂ Te ₃ matrix and Pt-Sb ₂ Te ₃ nanocomposite	138
6.2	Determination of van der Pauw resistivity and Hall effect measurement accuracy	140

List of Figures

1.1	Electronic structures of polycrystalline and amorphous semiconductors.....	3
1.2	Particle in a three dimensional box.....	6
1.3	Carrier delocalization in quantum dots and nanocrystals.....	10
1.4	Miniband formation in a quantum dot superlattice.....	13
1.5	Carrier mobility, charging energy and energy site variation in nanocrystal assemblies.....	16
1.6	Peltier and Seebeck effects.....	21
1.7	Thermoelectric modules and optimization of ZT.....	25
2.1	Resistivity and thermopower measurement techniques.....	44
3.1	Synthesis of metal chalcogenide nanocrystal via hot injection.....	52
3.2	Structural, chemical, and optical characterization of PbTe nanocrystals.....	55
3.3	TEM images and absorption spectra of Ag ₂ Te nanocrystals as a function of growth duration.....	57
3.4	TEM images, XRD patterns, and absorption spectra of three different sizes Ag ₂ Te nanocrystals.....	59
3.5	Extinction coefficient and temperature-dependent optical gap of Ag ₂ Te nanocrystals.....	61
3.6	Absorption spectra of Ag ₂ Te nanocrystals as a function of dielectric constant of the medium.....	62
3.7	Measurement configuration of X-ray diffractometer.....	63
3.8	Schematics of X-ray generator.....	65
3.9	X-ray focusing methods.....	67
3.10	Selection slits for para-focusing and parallel beam focusing.....	68
3.11	Diffraction peak shift from sample height variations.....	69
3.12	Soller slits and monochromators.....	70
3.13	Sample illumination area.....	71
3.14	Powder diffraction data of PbTe nanocrystals and nanocubes.....	73
3.15	Spatially resolved in-plane XRD.....	74
3.16	Transmission SAXS of PbS nanocrystals.....	75
3.17	Reflection-mode SAXS and in-plane SAXS of nanoplates.....	77

4.1	Energy-dependent DOS, mobility and conductivity of semiconductor nanocrystal solids.....	89
4.2	Open-circuit voltage and temperature-dependent thermopower of PbTe nanocrystal solids.....	90
4.3	Thermopower measurement consistency.....	91
4.4	TEM images and SAXS profiles of PbTe nanocrystals as a function of size.....	93
4.5	Slope of temperature-dependent thermopower as a function of PbTe nanocrystal size.....	94
4.6	TEM images of PbTe nanocrystals before and after hydrazine treatment.....	96
4.7	FET characteristics of n-type and p-type PbTe nanocrystal solids.....	97
4.8	TEM images, absorption spectra, and SAXS profiles of monodisperse and polydisperse PbTe nanocrystals.....	102
4.9	y-intercept of temperature-dependent thermopower.....	103
5.1	Temperature-dependent thermopower and conductivity measurements of nanocrystal solids.....	114
5.2	DOS versus energy diagram of PbTe nanocrystal solids.....	116
5.3	DOS versus energy diagram of Ag ₂ Te nanocrystal solids.....	118
5.4	TEM images of PbTe/Ag ₂ Te mixtures of three different ratios	119
5.5	Reflection-mode SAXS profiles of PbTe nanocrystal solids doped with Ag ₂ Te nanocrystals.....	121
5.6	TEM images and packing models of nanocrystal solids.....	121
5.7	Temperature-dependent thermopower and conductivity measurements of PbTe nanocrystal solids doped with Ag ₂ Te nanocrystals	124
6.1	TEM images and SAED patterns of Sb ₂ Te ₃ films	129
6.2	TEM images of solution-processable nanocomposite solution	130
6.3	Band alignment in Pt-Sb ₂ Te ₃ nanocomposites	134
6.4	XRD patterns and EDS spectrum of Pt-Sb ₂ Te ₃ nanocomposites.....	135
6.5	TEM images and SAED patterns of Pt-Sb ₂ Te ₃ nanocomposites after heat and TOP treatments	136
6.6	SEM images and thermopower measurements on Pt-Sb ₂ Te ₃ nanocomposite and Sb ₂ Te ₃ matrix	138
7.1	Nernst and Ettingshausen effects.....	148

1. Semiconductor nanocrystal solids

1.1 Introduction

Semiconductors are a group of materials with electronic properties intermediate between insulators and metals. The electrical conductivity can be controlled over orders of magnitude by introducing an electric field, light, impurity content, or by changing the temperature. The wide flexibility of semiconducting materials' electronic, optical, and optoelectronic properties has been the core of current semiconductor technologies creating a multibillion dollar industry. To achieve uniformity over a large area with a consistent electronic properties as well as economic viability, semiconductors have been developed from defect-free single crystals, polycrystals with grain boundaries (Figure 1.1(a)) and amorphous with the absence of long range order (Figure 1.1(c)). Each form of semiconductors shows characteristic electronic properties. For instance, carrier mobility in polycrystalline semiconductors is thermally activated and shows an unusual dependence on the doping concentration (Figure 1.1(b)) due to the band bending arising from interfacial trap states at the grain boundaries^[1] Amorphous semiconductors exhibit three distinct conduction regimes (Figure 1.1(d)) each with characteristic temperature dependences:

extended state conduction over the mobility edge, thermally activated hopping between localized band tail states, and variable range hopping near the Fermi energy level.^[2,3] Standard measurement techniques, such as Hall effect measurements, were crucial in examining the properties of polycrystalline semiconductors^[1,4] before material engineers could actually understand their applications. Although for amorphous semiconductors, Hall effect measurements showed anomalous results,^[5,6] field-effect transistor measurement turned out to be a valuable characterization tool to probe the density of state distribution and to verify the conduction in extended states above a sharp mobility edge.^[7,8] This has led to the successful commercialization of hydrogenated amorphous silicon in solar cell applications.^[9]

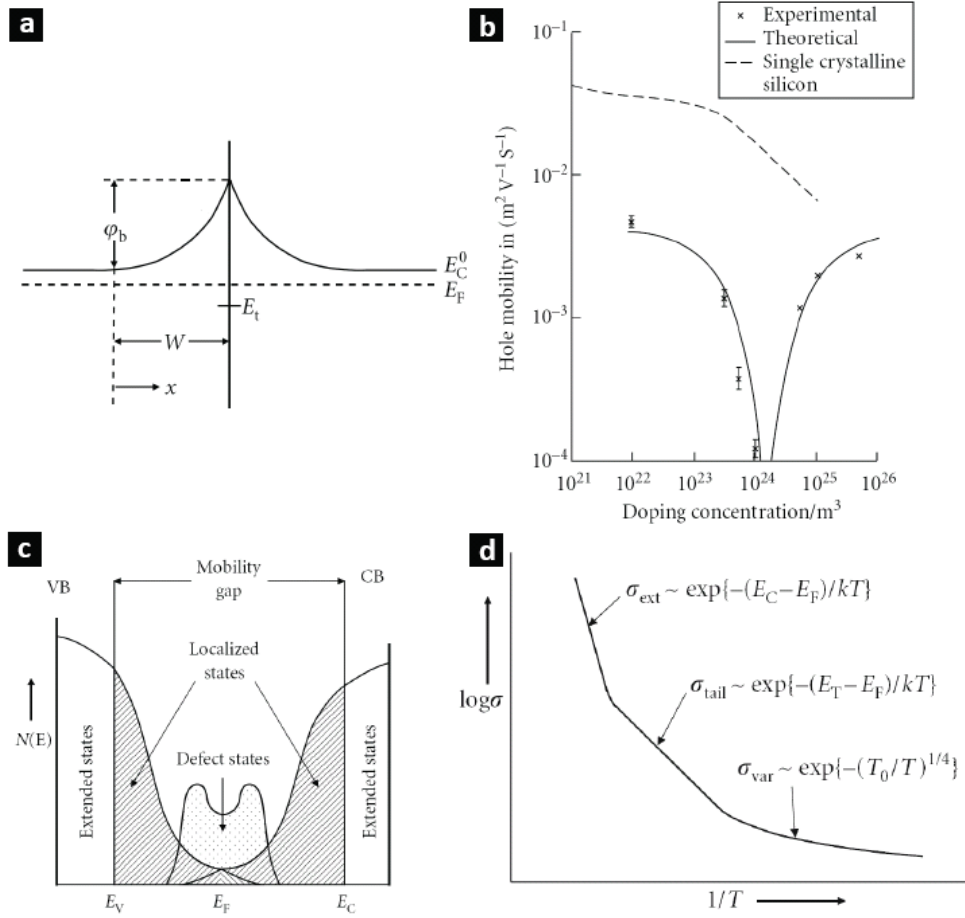


Figure 1.1 Schematics of electronic structure and properties of polycrystalline and amorphous semiconductors (adapted from reference [1]). (a) Band bending introduced at the grain boundary of polycrystalline semiconductor showing the potential barrier of ϕ_b . The depletion width (W) is smaller than the grain size and the Fermi energy level (E_F) is higher than the defect states (E_t). E_{C0} denotes the effective conduction band. (b) Experimental Hall mobility obtained from polycrystalline semiconductor showing a strong dependence on doping concentration. (c) Density of state diagram and (d) three characteristic conduction regimes observed in amorphous semiconductors.

On the other hand, semiconductors have also evolved into smaller dimensions such as thin films,^[10] nanowires,^[11] and nanocrystals,^[12] in which the crystal dimension dramatically modifies the electronic properties. Semiconductor nanocrystals are often referred to as “quantum dots” as the wave functions of their

electrons are confined in all three dimensions. Solids constructed from these semiconductor nanocrystals provide unprecedented functionality with novel physics. It is one of the most dynamic fields in nanoscience and technology. However, measurements and their interpretation is a challenging task in nanostructures and this has prevented clear understanding of electronic transport.. The motivation of this research is to explore the electronic density of states, doping, and carrier mobility in semiconductor nanocrystal solids, which has traditionally been a major focus of study in bulk semiconductors. Temperature-dependent electrical conductivity, thermopower and field-effect measurements are employed in combination with the model developed for amorphous material systems. This thesis aims to develop a new approach to monitor doping in semiconductor nanocrystal solids otherwise inaccessible using conventional measurement technique and to design a material system with enhanced thermoelectric power conversion efficiency.

1.2 Semiconductor nanocrystal as artificial atoms

In an isolated semiconductor nanocrystal, the electron wave is spatially confined in a small crystallite that contains only hundreds or thousands of atoms. The energy levels that electrons can occupy depend strongly on the size, shape, and the

crystal structure of the nanocrystal as well as the energy barrier of the surrounding medium. A simplistic model that provides a basic understanding of quantum mechanical confinement is an electron in a square box surrounded by infinite potential barriers (Figure 2.1(a)). The solution to the time-independent Schrödinger equation with appropriate boundary conditions gives,^[13]

$$\psi(x, y, z) = \left(\frac{2}{a}\right)^{3/2} \sin \frac{n_x \pi}{a} \sin \frac{n_y \pi}{a} \sin \frac{n_z \pi}{a} \dots\dots\dots(1)$$

$$E = \frac{\hbar^2 \pi^2}{2m_e a^2} (n_x^2 + n_y^2 + n_z^2)$$

where $n_{x,y,z}$ are the quantum numbers (Figure 2.1(b)) that reflect quantized energy states as well as atomic-like orbitals (if the wave function is translated into spherical coordinates) of electrons in a three dimensional box and a is the size of a nanocrystallite indicating a strong influence of size on energy.

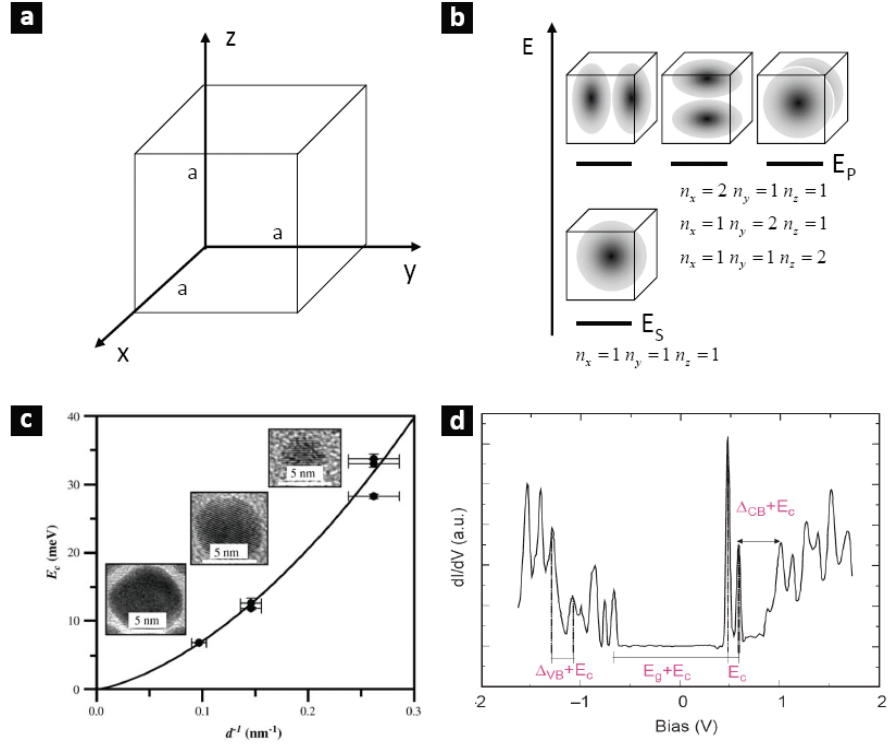


Figure 1.2 (a) Particle in a three dimensional box. (b) Graphical representation of orbitals and energy levels derived from the solution of the time-independent Schrödinger equation. (c) Charging energy as a function of CoPt₃ nanocrystal size (adapted from reference [16]). (d) STM spectroscopy on InAs nanocrystal showing two and up to six electrons are injected to E_S and E_P energy levels, respectively. (adapted from reference [17]).

Experimental confirmation on the electronic structure of semiconductor nanocrystals was performed by sequentially injecting electrons into an isolated nanocrystal using scanning tunneling microscopy (STM).^[14] The classical electrostatic energy required to add an electron to a neutral nanocrystal is called the charging energy E_C ,^[15] which is also known as the Coulombic blocking potential. In a simple form, considering a nanocrystal as a conducting sphere with the radius of R embedded in a dielectric of relative permittivity ϵ_m , the charging energy can be expressed as:

$$E_C = \frac{e^2}{2C_S} = \frac{e^2}{4\pi\epsilon_0\epsilon_m R} \dots\dots\dots(2)$$

where e is the elemental charge, C_S is the self capacitance of a sphere, and ϵ_0 is the vacuum permittivity. The charging energy is a function of nanocrystal size which has been experimentally demonstrated in CoPt₃ nanocrystals (Figure 2.1(c)).^[16] Adding the first electron to a ground state semiconductor nanocrystal requires an energy of $E_S + E_C$, where E_S denotes the energy of the first quantum confined energy level associated with the s orbital. For the second electron to be injected into the nanocrystal, electron-electron Coulomb repulsion E_{e-e} should be taken into account, requiring a total energy of $E_S + E_C + E_{e-e}$. A total of two electrons can be added to the lowest E_S energy level and six more electrons can be injected, in sequence, to the next P energy level (E_P) as demonstrated in chemically synthesized indium arsenide (InAs) nanocrystals (Figure 2.1(d)).^[17] Furthermore, probability of electron injection into the nanocrystal strongly depends on the symmetry of the wave function.^[18] For example, depending on how the STM tip and the p orbital wave function overlaps, tunneling probability of P_Z or P_X levels were determined and experimentally resolved in cadmium selenide (CdSe) nanocrystals.

The electronic structure of quantum confined semiconductor nanocrystals bear a strong resemblance to an atom. Hence, semiconductor nanocrystals are also

called the artificial atoms,^[19-21] which can be used as building blocks to construct artificial solids. This opens an exciting opportunity in material science to design and engineer artificial condensed matter that does not exist in nature with a prescribed set of physical properties.

1.3 Artificial solids constructed from semiconductor nanocrystals

When two isolated semiconductor nanocrystals are brought together to form a solid, repulsive and attractive forces find a balance to determine the equilibrium interparticle distance. During this process, dramatic changes in the electronic structure occurs giving rise to interesting electronic properties, analogous to solids built up from atoms. First, consider two nanocrystals, identical in size and shape, brought closely together. Two energy levels are separated by a barrier where charge transport between them is classically forbidden. Quantum mechanically, two wave functions decay inside the finite potential barrier and the overlap between them results in a finite probability of tunneling. The resonant tunneling rate between two energy levels is given by,^[22]

$$\Gamma = \Gamma_0 \exp \left[- \left(\frac{2m^* (E_{vac} - E)}{\hbar^2} \right)^{1/2} (d + 2r) \right] \dots\dots\dots(3)$$

where m^* is the effective mass of the electron, d is the interparticle spacing or the width of the potential barrier, $E_{vac} - E$ is the barrier height, r is the radius of the particle, and Γ_0 denotes the tunneling rate at vanishing barrier height or width. The exponent is often described as $-(d+2r) \cdot k$, where $1/k$ is spatial decay of the wave function outside the nanocrystal defining the localization length. The strength of the quantum mechanical coupling in terms of energy is given as $\hbar\Gamma$, which is usually referred to as the exchange coupling energy. When the coherent wave delocalizes between two nanocrystals, energy levels split into a bonding and anti-bonding states analogous to the linear combination of atomic orbital (LCAO). From an electronic standpoint, quantum mechanically coupled nanocrystals can be viewed as a nanocrystal molecule. This was experimentally demonstrated in gallium arsenide (GaAs) quantum dots using micro-photoluminescence measurements.^[23] As the interparticle distance decreases, splitting of the energy level is more pronounced (Figure 1.3(a)), and the the gap between the highest occupied molecular orbital (HOMO) - lowest unoccupied molecular orbital (LUMO) decreases.

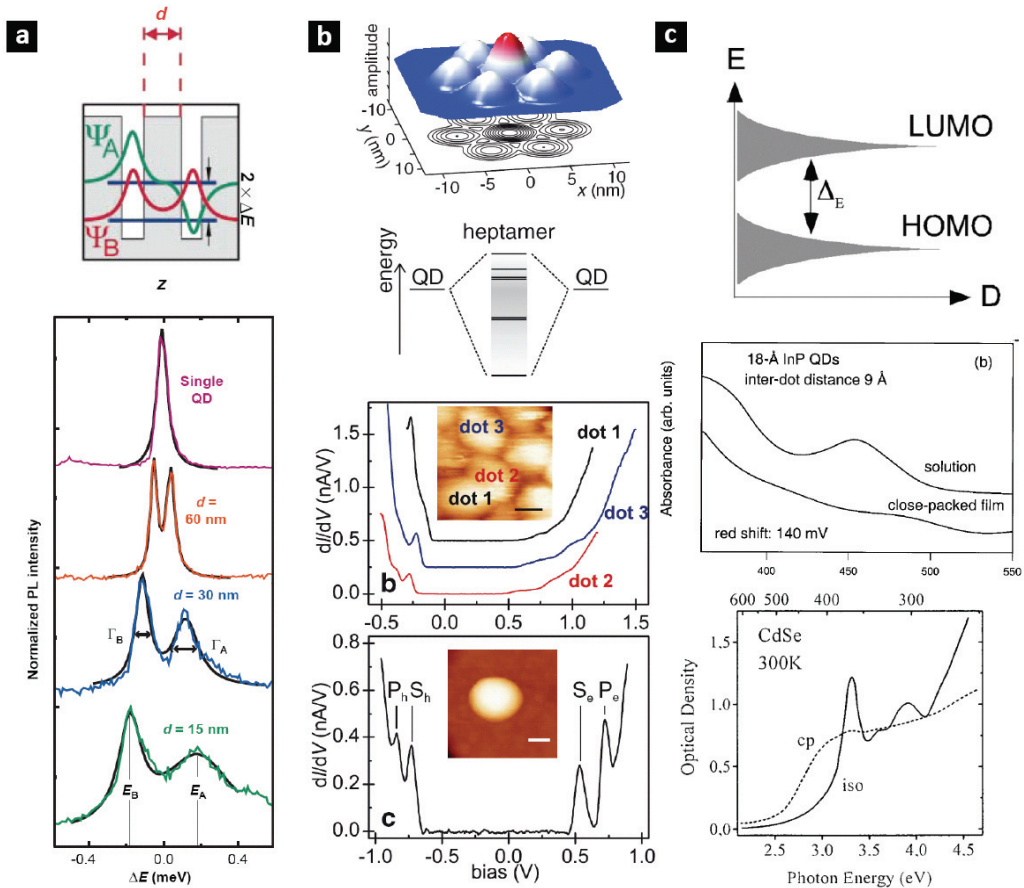


Figure 1.3 (a) Micro-photoluminescence spectra obtained from GaAs quantum dot synthesized using molecular beam epitaxy. As the interparticle spacing reduces two electron wave functions overlap splitting the energy levels into bonding and anti-bonding states. (adapted from reference [23]) (b) Schematic illustration of PbSe nanocrystal heptamer with wave function delocalized over nearby nanocrystals. The energy level becomes continuous and broadens reducing the HOMO-LUMO gap as confirmed by the STM measurements (adapted from reference [24]). (c) Absorption spectra obtained from extremely small InP (15 - 23 Å) and CdSe (~16 Å) nanocrystals showing smooth feature with reduced optical bandgap similar to that of the bulk semiconductor (adapted from reference [26,27]).

As more nanocrystals are added to form a nanocrystal heptamer (Figure 1.3(b)) and the electron wave function becomes delocalized over nearby nanocrystals, the effect of quantum confinement is reduced. This further closes the HOMO-LUMO

gap. Moreover, as more energy levels are introduced between discrete energy levels, the electronic structure becomes more continuous as is confirmed by STM measurement on lead selenide (PbSe) nanocrystal assemblies.^[24] As more nanocrystals are assembled to a hexagonally packed superlattice, a continuous miniband starts to form with a smaller bandgap.^[25] For extremely small indium phosphide (InP, 15 - 23 Å) and CdSe (~16 Å) nanocrystals with reduced interparticle spacing, a smaller nanocrystal radius further increases the coupling (equation (3)) yielding smooth, band-like absorption features (Figure 1.3(c)).^[26,27]

A theoretical model^[28,29] was also proposed demonstrating the formation of minibands in a silicon (Si) quantum dot superlattice (2 nm cubic nanocrystals, 1 nm interparticle spacing) inside a silicon nitride dielectric matrix (Si₃N₄, 1.9 eV barrier height) by introducing three quantum numbers $n_{x,y,z}$ (Figure 1.4(a)) similar to the model previously discussed in Figure 1.2(a). A bulk-like dispersion relationship was derived (Figure 1.4(b)) and the bandwidth as a function of barrier height (Figure 1.4(c)) and interparticle distance (Figure 1.4(d)) were studied.^[28] The electronic conduction in a strongly coupled nanocrystal solid is expected to show Bloch transport approaching that of the bulk with the carrier mobility of 100 - 200 cm²/Vs (Figure 1.4(e)). However, experimental measurements of field-effect mobility in nanocrystal solids show significantly lower values. For example, 6.1 nm PbSe

nanocrystals treated with different molecular length of thiols showed electron mobility ranging from 10^{-2} to 10^{-4} cm^2/Vs , when the interparticle spacing was varied from 4 to 9 Å, respectively ($m^* = 0.28m_e$, barrier height 1.6 eV).^[30] Note that the theoretical model in Figure 1.4(e) uses $m^* = 0.4m_e$ and barrier heights of 3.17 eV (SiO_2), 1.9 eV (Si_3N_4), and 0.5 eV (SiC).

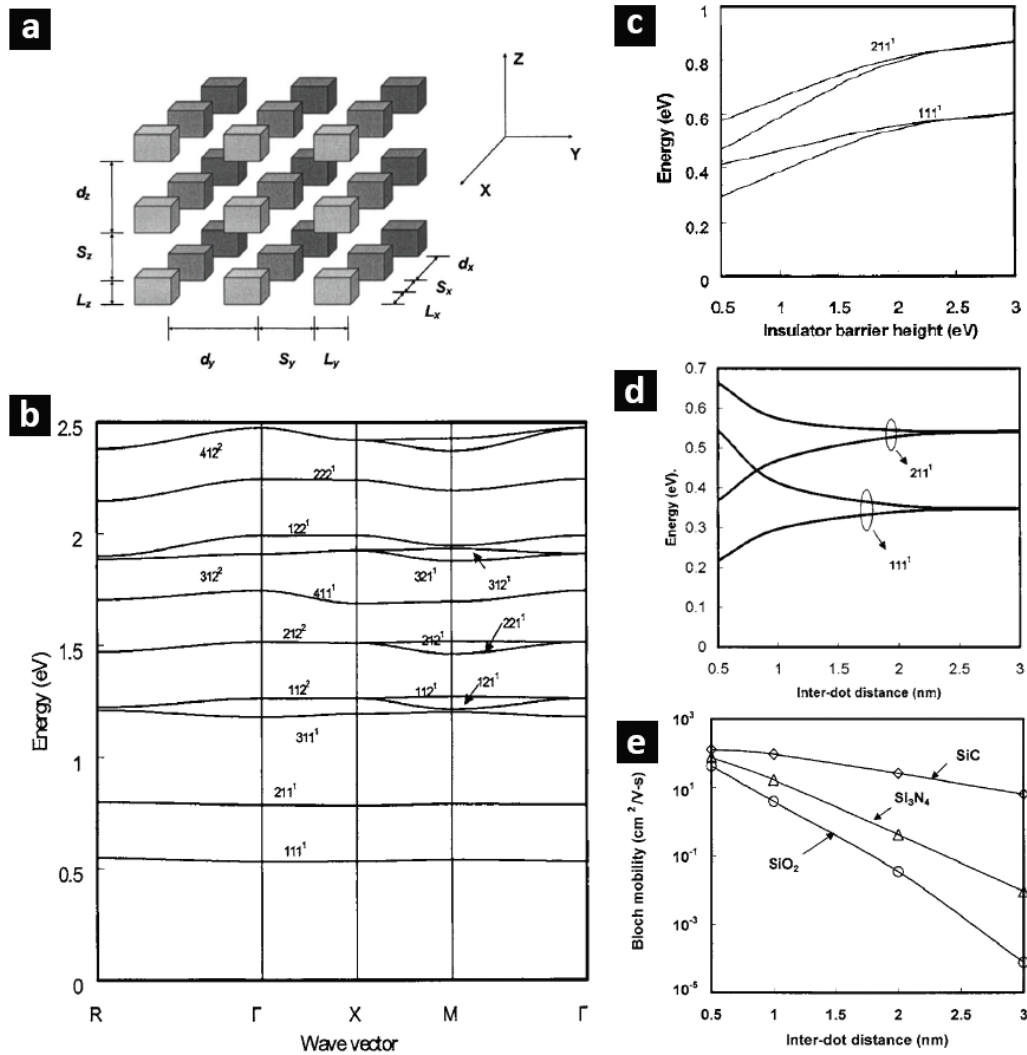


Figure 1.4 (a) Model structure of quantum dot superlattice to demonstrate the formation of miniband under strong coupling regime. (b) Conduction band dispersion relationship derived from 2 nm Si quantum dot superlattice with 1nm interparticle spacing embedded in Si_3N_4 dielectric matrix. Superscript denotes band degeneracy. (c,d) Bandwidth as a function of barrier height and interparticle spacing. (e) Bloch mobility as a function of interparticle spacing and barrier height (different materials of dielectric matrix). All Figures were adapted from reference [28].

Extensive studies were performed on amorphous semiconductors, relating the carrier mobility to the electronic structure and the carrier transport process. The electronic structure of amorphous semiconductors consists of extended and localized

electronic states sharply separated by the mobility edge (Figure 1.5(a)). Above the mobility edge, all the electronic states are delocalized (extended) and carriers show band-like transport behavior which typical mobilities of 100 cm²/Vs. On the other hand, below the mobility edge, all the electronic states are severely localized and the transport occurs via hopping between localized states. Hopping mobility is typically on the order of 10⁻² to 10⁻⁴ cm²/Vs. The mobility edge indicates the lowest limit of carrier mobility for extended transport which is also known as the minimum metallic conductivity of amorphous semiconductors. This can be roughly estimated when the mean free path of the electron is comparable to the inter-atomic spacing a_i as,

$$\mu_{\min} = \frac{ea_i}{v_{th}m^*} \dots\dots\dots(4)$$

where v_{th} is the thermal velocity of an electron ($\sim 10^5$ m/s).^[3] Taking a_i of ~ 3 Å gives 5 cm²/Vs. Similar approximation can be derived using the Einstein–Smoluchowski relation when the mean free path of the diffusive transport is near the inter-atomic distance:

$$\mu_{\min} = \frac{eD}{k_B T} \approx \frac{e\hbar}{6m^*k_B T} \dots\dots\dots(5)$$

where D is the diffusion coefficient, k_B is the Boltzmann constant, and T is the temperature. Diffusion coefficient is given by $D = (1/6) \cdot v_{el} a_i^2$ where v_{el} is the

electronic frequency ($\nu_{el} \approx h/2\pi m^* a_i^2 \approx 10^{15}$ /s). At room temperature, the minimum mobility is estimated as $7.5 \text{ cm}^2/\text{Vs}$.^[2] Nanocrystal solids with carrier mobilities below these minimum values indicate that electron wave functions are localized to individual nanocrystals and the transport occur via hopping. Thus, in reality, nanocrystals in a solid are not ideally coupled and suffer from inherent disorder due to variation in size, shape, surfaces, and from packing disorder. When this energetic disorder is larger than the electronic coupling energy, the physical properties of these systems can more closely resemble that of non-crystalline materials.

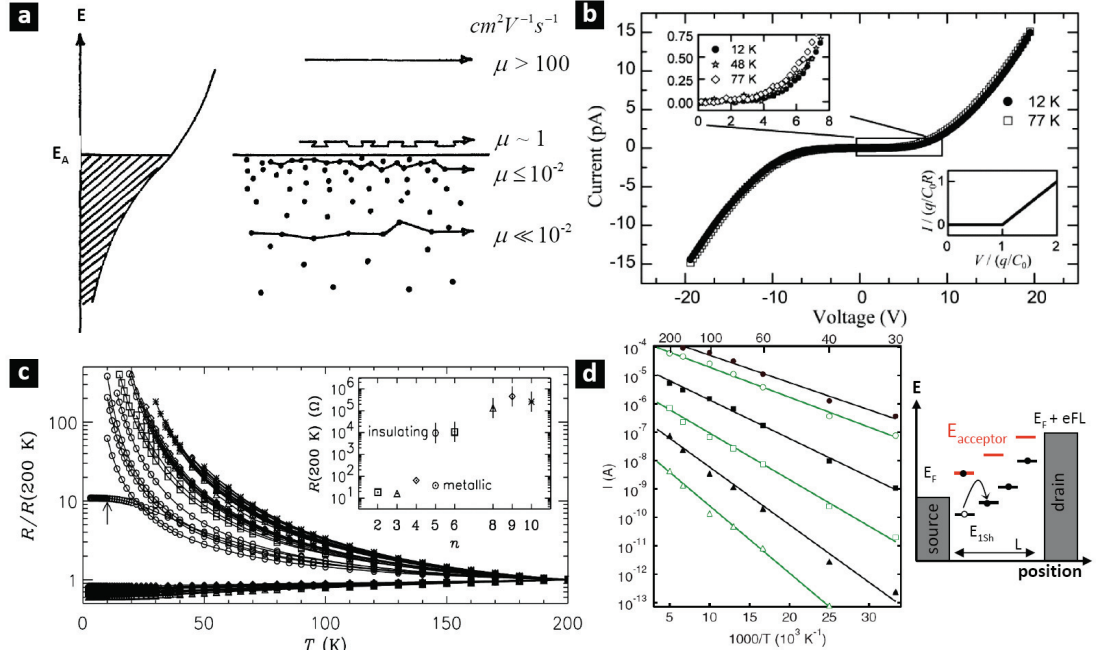


Figure 1.5 (a) Schematic representation of charge carrier mobility as a function of energy in amorphous semiconductors. Shaded area denoted localized states (adapted from reference [3]). (b) Current-voltage (IV) curve obtained from a monolayer assembly of 5.5 nm Au nanocrystals capped with 1.7 nm dodecanethiol showing an onset of current at a threshold voltage due to Coulombic blockade (adapted from reference [33]). (c) Temperature-dependent conductance curve from 5 nm Au with $HS(CH_2)_nSH$ cross-linking ligand. The slope changes from positive to negative at $n = 5$ indicating a MIT transition (adapted from reference [34]). (d) Temperature-dependent current measured as a function of source-drain field on thermally annealed PbSe nanocrystal solids. At high fields, holes only hop upward, eliminating the activation energy from energy disorder (ΔE_S) which is observed as a decreasing slope of current vs. $1000/T$ plot (adapted from reference [35]).

There are two terms that oppose exchange coupling ($\hbar\Gamma$) between nanocrystals. First is the charging energy E_C , which was discussed in the previous section. To add an electron to a nanocrystal solid, an additional term accounting for the mutual capacitance C_M between adjacent nanocrystals is needed:^[16,31]

$$\begin{aligned}
E_{C,solid} &= \frac{e^2}{2(C_S + \sum C_M)} \\
C_S &= \frac{e^2}{4\pi\epsilon_0\epsilon_{avg}R} \\
C_M &= 2\pi\epsilon_0\epsilon_{avg}R\left(1 + \frac{2R}{d}\right) \\
\epsilon_{avg} &= \epsilon_{lig} + \frac{4\sqrt{2}}{3}(\epsilon_{NC} - \epsilon_{lig})\left(\frac{R}{2R+d}\right)^3
\end{aligned}
\tag{6}$$

where d is the nanocrystal surface to surface separation, ϵ_{avg} is the volume-averaged dielectric constant^[32] calculated from the nanocrystal (ϵ_{NC}) and the ligand (ϵ_{lig}) dielectric constants. If the charging energy is smaller than the exchange coupling energy, electrons delocalize over the nanocrystal solids and band-like transport is observed. On the other hand, if the charging energy is larger, the electron wave functions localize in individual nanocrystals and transport occur via hopping which typically shows an onset of current at a threshold voltage due to the Coulombic blockade (Figure 1.5(b)).^[33] A sharp transition between band-like and hopping transport is known as Mott metal to insulator transition (MIT). An experimental confirmation was observed in gold (Au) nanocrystals capped with different length of cross-linking thiols $\text{HS}(\text{CH}_2)_n\text{SH}$.^[34] For $n < 5$ (below 1.1 nm), the slope of the temperature-dependent conductance changed from positive to negative (Figure 1.5(c)). Positive slope indicates that the mobility is thermally activated which a typical behavior found in hopping conduction. On the contrary, a negative slope is found in

band-like transport due to enhanced electron-phonon scattering at high temperatures.

The energy disorder ΔE_S is another key parameter that opposes exchange coupling. Unlike atoms, nanocrystals always have finite dispersion of size and shape from synthesis. This results in different confinement energies and introduces energy level offsets. If the exchange coupling energy is smaller than the energy disorder, the electron wave function localizes in each nanocrystal which is known as the Anderson localization. In order for the electrons to hop to other nanocrystals with different energies, thermal energy should be gained (upward hop) or released (downward hop) from (to) the nanocrystal lattice. For $h\Gamma > \Delta E_S$, band-like electronic structure as well as transport is observed. The effect of energy disorder was experimentally observed in weakly coupled PbSe nanocrystal films thermally annealed at ~ 400 K.^[35] Current-voltage (I-V) characteristics at low source-drain field show two activation energies corresponding to the activation energy for carrier generation (energetic difference between the Fermi level and the first energy level E_S) and activation energy due to energy disorder (ΔE_S) were observed. At high fields, energy levels align between the source and the drain contacts so that holes only have to hop upward (Figure 1.5(d)). This eliminates the activation energy due to the energy disorder and reduces the slope of current vs. $1000/T$.

Although many studies presented here were dedicated to understanding the

transport physics of carriers in nanocrystal solids, less is known about the surface of these nanocrystal constituents. Ligands that coordinate the surface of the nanocrystal are known to electronically dope the system.^[36] Unsaturated bonds on the crystal surface are also known to create electronic states at the mid-gap in nanocrystals.^[37] However, standard semiconductor theories does not fully explain the experimental observations of electronic transport in nanocrystal solids. Development of new measurement tools and theoretical methods are required to understand the electronic behavior of these material systems in more detail.

1.4 Nanostructured thermoelectrics

Motion of free carriers in metals or semiconductors are not only associated with charges but also with heat.^[38-40] First observed by Peltier, when two dissimilar materials are joined together and the electrical current (I) was passed through, heat (Q) was either absorbed or ejected depending on the direction of current flow. This Peltier effect is proportional to the current ($Q = \Pi \cdot I$, where Π is the Peltier coefficient) and it is an intrinsic property of the material. In a simple picture, the Peltier effect is due to the energetic difference of carriers in different materials (difference in material's Fermi energy level). As shown in Figure 1.6(a), when electrons flow from

material 1 to 2, the energy of the electron is reduced and this energy is released to the lattice, thereby heating the junction. When the electrons are flowing from material 2 to 1, electrons absorb energy from the lattice which cools the junction.

In the opposite case, when two different materials are joined together and the junctions were kept at different temperatures, a voltage difference is introduced, proportional to the temperature difference. The thermopower, also called the Seebeck coefficient, is the ratio between the voltage (ΔV) and temperature difference ($S = -\Delta V/\Delta T$). The physical origin of Seebeck effect is the thermodiffusion of carriers. As shown in Figure 1.6(b), on the hot end, Fermi distribution softens introducing a large number of high energy electrons. Due to this concentration gradient, carriers diffuse to the cold end until Coulombic repulsion further opposes the flow. The build-up of electrons on one side generates this voltage difference.

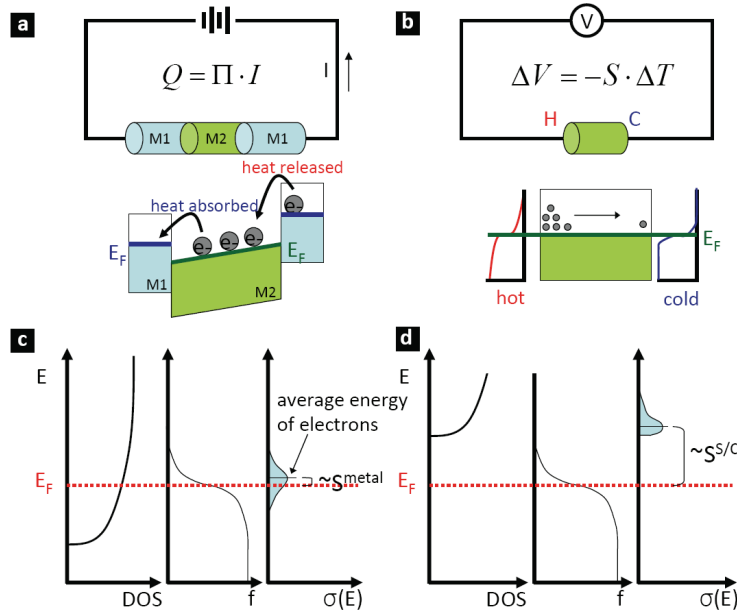


Figure 1.6 Schematic representation of thermoelectric effects. (a) Peltier effect (b) Seebeck effect (c), (d) Estimation of thermopower for metals and n-type semiconductors, respectively.

Formulation of thermopower from the Peltier coefficient gives a better intuitive picture of thermoelectric phenomena.^[41] The Peltier coefficient determines the energy (heat) transported by carriers per unit charge. This energy is measured relative to the Fermi level (E_F) and the contribution to each carrier on Π is proportional to their relative contribution to the total conductivity ($\sigma(E)/\sigma$) as

$$\Pi = -\frac{1}{e} \int (E_T - E_F) \frac{\sigma(E)}{\sigma} dE \dots\dots\dots(7)$$

where, E_T is the transport energy level (energy level where transport occurs) and $\sigma(E)$ is the energy-dependent conductivity (also known as differential conductivity).

Thermopower is related to the Peltier coefficient as $S = \Pi/T$ (Onsager or Kelvin

relation)^[42] and thus,

$$S = -\frac{k_B}{e} \int \frac{(E_T - E_F) \sigma(E)}{k_B T} dE \dots\dots\dots(8)$$

In terms of thermodynamics, thermopower indicates the entropy carried by carriers (change of heat divided by the temperature). For non-degenerate n-type semiconductor where conduction occurs in the conduction band, equation (8) simplifies to

$$S = -\frac{k_B}{e} \left[\frac{(E_C - E_F)}{k_B T} + A \right] \dots\dots\dots(9)$$

where E_C is the conduction band and A is the constant reflecting average kinetic energy carried by the carrier above the conduction band edge. The constant A , which is also known as the heat of transport constant is given as

$$A = \frac{\int_0^\infty \frac{\varepsilon}{k_B T} \sigma(\varepsilon) d\varepsilon}{\int_0^\infty \sigma(\varepsilon) d\varepsilon} \dots\dots\dots(10)$$

where $\varepsilon = E - E_C$. Thus, in a simple picture, thermopower consists of the potential energy contribution (first term in the bracket in equation (9)) and the kinetic energy contribution (second term in the bracket in equation (9)). In the case of metals, the Fermi level lies inside the conduction band and the contribution from the potential

energy is neglected which simplifies to the following equation known as the Mott relation:

$$S = \frac{\pi^2 k_B^2 T}{3e} \left[\frac{d(\ln \sigma(E))}{dE} \right]_{E=E_F} \dots\dots\dots(11)$$

Therefore, metals usually have low thermopower compared to semiconductors (Figure 1.6(c,d)). Note that the thermopower in semiconductors varies dramatically depending on the position of the Fermi level (i.e. doping concentration). Note also that the major feature discerning the thermopower behavior of a metal and a semiconductor is their temperature dependence (metal $S \sim T$, semiconductor $S \sim 1/T$). Typical values for metals and semiconductors are given in Table 1.1.^[43] Positive or negative signs of thermopower are an indication that majority carriers are holes or electrons, respectively. The existence of both n- and p-type thermoelements enables us to construct a complete thermoelectric module which will be discussed in the following paragraph.

Materials	Au	Cu	Ag	Si	Ge	Bi ₂ Te ₃
Thermopower [uV/K]	1.94	1.83	1.51	450	-548	-210

Table 1.1 Typical thermopower values of various metals and semiconductors (adapted from reference [43]). Note that thermopower of semiconductors can be dramatically varied by doping.

In a typical device, thermoelectric modules consist of n- and p-type legs connected in series electronically and in parallel thermally, as shown in Figure 1.7(a). Usually, thousands of these thermocouples are connected (Figure 1.7(b)) and the open circuit voltage generated is the sum of the thermopower produced at each couple. The efficiency of power generation is given by the ratio of net heat flow to electrical power output:

$$\eta = \frac{W}{Q_H} = \frac{I[(S_p - S_n)\Delta T - IR]}{KT + (S_p - S_n)IT_H - \frac{1}{2}I^2R} \dots\dots\dots(12)$$

where the numerator contains the Seebeck effect and the first, second, and third terms in the denominator represent thermal conductivity, the Peltier effect, and Joule heating, respectively.

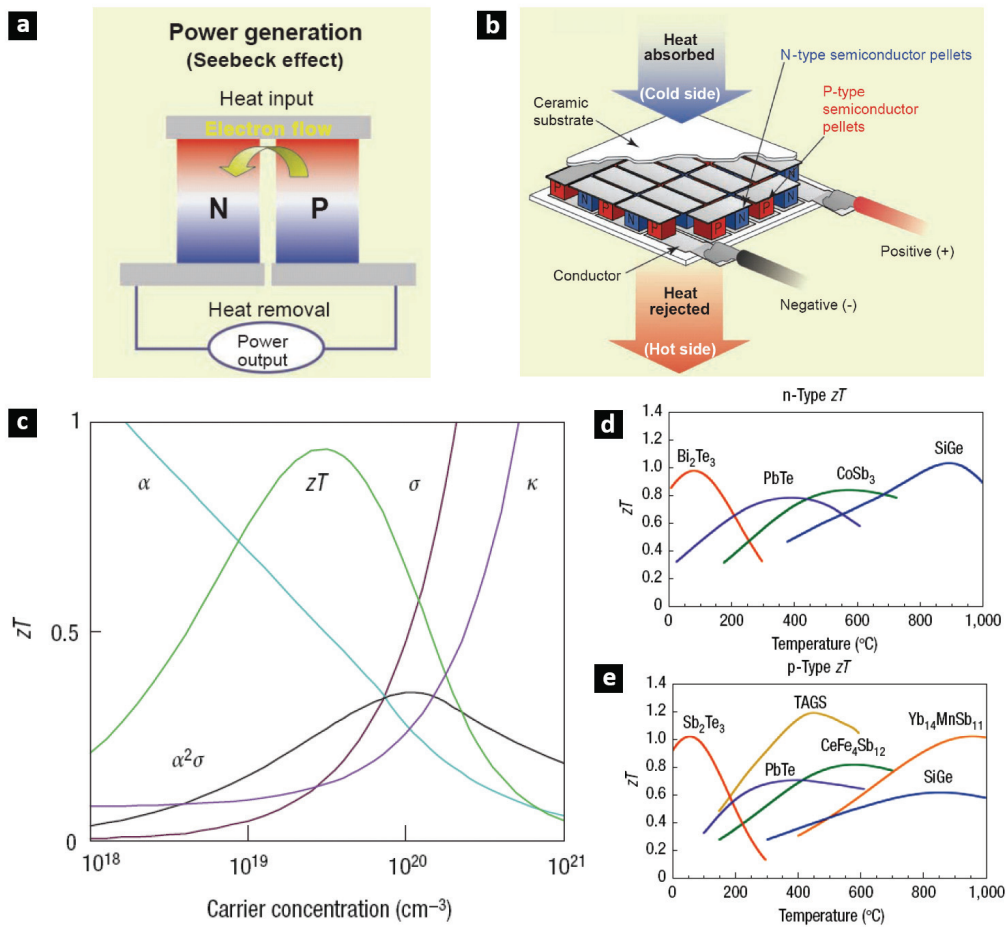


Figure 1.7 Basic construction of thermoelectric module and optimization of ZT. (a), (b) Thermocouple constructed from n- and p-type leg and thermoelectric generator. (adapted from reference [44]) (c) Optimization of materials property for maximum ZT. (d), (e) State-of-the-art n- and p-type commercial thermoelectric material. (adapted from reference [45])

Mathematical rearrangement of maximum efficiency gives the following

equation:

$$\eta_{\max} = \frac{\Delta T}{T_H} \cdot \frac{\sqrt{1+ZT} - 1}{\sqrt{1+ZT} + \frac{T_C}{T_H}} \dots\dots\dots(13)$$

The first term ($\Delta T/T_H$) is the Carnot efficiency which reflects the ultimate limits of thermoelectric performance, and the second term gives an important concept of

dimensionless figure of merit, ZT :

$$ZT = \frac{S^2 \sigma}{k} T \dots\dots\dots(14)$$

where σ is the electrical conductivity and k is the thermal conductivity. Thermal conductivity is the sum of electronic and lattice phonon contributions. In order to maximize ZT , it is imperative to maximize the power factor, $S^2 \sigma$, and minimize the thermal conductivity.

The key to achieving maximum ZT is optimization of interrelated material properties. First of all, in order to have large Seebeck coefficient, there should be a single type of carrier. In ambipolar semiconductors, for example, both electrons and holes diffuse to the cold end, canceling out the thermopower. Furthermore, carrier concentration in semiconductors should be low so that the Fermi energy is far from the band edge, as shown in Figure 1.6(d). However, low carrier concentration significantly reduces electrical conductivity. Carrier concentration is also coupled with the electronic contribution of thermal conductivity by the Wiedemann-Franz law:

$$k_e = L\sigma T = ne\mu LT \dots\dots\dots(15)$$

where k_e is the electronic contribution to the thermal conductivity and L is the Lorenz factor. Thus, the maximum ZT lies in the range where all of these three conflicting

parameters are optimized. This range of carrier concentration is in between 10^{19} and $10^{21} /\text{cm}^3$, as shown in Figure 1.7(c), usually found in degenerate semiconductors. There is a long history of efforts to reduce the lattice thermal conductivity by introducing atomic disorder, interfaces, and constructing complex unit cells. All these increases phonon scattering but they also affect material's electrical conductivity by scattering electrons and decreasing carrier mobility. Thus, best thermoelectrics rather require unusual materials: phonon-glass (low thermal conductivity), electron-crystal (while maintaining electronic conduction). The most widely used thermoelectric materials are bismuth telluride (Bi_2Te_3), lead telluride (PbTe), and their alloys which are semiconductors with heavy atomic weights. Current state-of-the-art thermoelectric materials are shown in Figure 1.7(d) and (e). Typical maximum ZT values for these materials are still limited to the range of 0.8 - 1.

Thermoelectric power generation has become an attractive means of future energy conversion. It is the easiest method to harvest electrical energy from waste heat or use electricity to function as an active heating/cooling element. Compared to conventional refrigerators, charge carriers are used as working fluids. Thus, with no moving parts, they are reliable, silent, maintenance free and cause no environmental impact. However, thermoelectrics have been too inefficient to be cost-effective in most applications. A broad search has been under way to identify new materials and

only recently, the major hurdle of $ZT \sim 1$ limit was overcome by using $\text{Bi}_2\text{Te}_3/\text{Sb}_2\text{Te}_3$ thin-film superlattices^[46] and $\text{PbTe}/\text{PbSeTe}$ quantum dot superlattices^[47], opening promising opportunities in nanostructured thermoelectrics. Sharp peaks in DOS have been theoretically^[48-50] predicted and experimentally^[51,52] observed to increase thermopower. Along with reduction in lattice thermal conductivity by an increase in the density of interfaces, the total ZT may be increased dramatically. However, it is interesting to note that two above representative examples (thin-film and quantum dot superlattice) only have benefited from a reduction in thermal conductivity while maintaining a thermoelectric power factor comparable to the bulk.^[53,54] The major advantage of implementing nanostructures to decouple interdependent material property and to optimize individual factors has not been realized to date.

The motivation for this research is to explore the extreme example of 0D nanostructures which is expected to have a strong impact on thermopower as well as carrier transport. Using nanocrystals as the fundamental building block to design new solid state material systems provides an effective approach to maximize the thermoelectric power factor with optimized carrier concentration. Nanocrystal solids also have uniquely sharp peaks in the electronic density of states that are theoretically predicted to increase thermopower. This material would not only benefit from interfacial scattering of phonons, but substantially increase the thermoelectric power

factor, and in turn, the figure of merit which could exceed the current state-of-the-art bulk counterpart ($ZT=1$). On the other hand, the concept of building artificial solids opens a new opportunity to explore novel physical properties distinct from their individual components. The ability to choose nanocrystals and assemble them into coordinated structure can be an effective bottom up design tool to overcome some of the current technological limits we face today.

1.5 Thesis overview

Solids constructed from monodisperse semiconductor nanocrystals inherently possess sharp distribution of density of states which is expected to impact thermopower as well as electrical conductivity. Most of the studies to date were limited to reporting enhanced thermopower values compared to the bulk counterpart. This thesis focuses on the measurement and the interpretation of temperature-dependent thermopower of PbTe nanocrystal solids to understand each physical term contributing to the thermopower. This physical understanding is, in turn, utilized to develop a powerful electronic spectroscopy tool to study carrier distribution and dynamics in semiconductor nanocrystal solids. This thesis also explores two major strategies to improve thermopower; (1) modification of the electronic density of states,

which is inherent in semiconductor nanocrystal solids, and (2) to modify carrier relaxation time to promote carrier energy filtering in solution-processable nanocomposites.

Chapter 2 introduces the physics of amorphous semiconductors which will be used to model the energy (charge and heat) transport and conversion in semiconductor nanocrystal solids.

In Chapter 3, the synthesis, structural characterization, and the chemical analysis of semiconductor chalcogenide nanocrystals is briefly introduced.

Chapter 4 focuses on the temperature-dependent thermopower measurements of PbTe nanocrystal solids. The Fermi energy level and the sharp distribution of the electronic density of states in nanocrystal solids are discussed.

In chapter 5, temperature-dependent electrical conductivity measurements are combined with the thermopower measurement. This study enables a detailed understanding of carrier transport in nanocrystal solids. Furthermore, a unique material system where a PbTe nanocrystal solid is doped with an artificial Ag₂Te nanocrystal dopant is investigated.

In chapter 6, solution-processable thermoelectric materials with enhanced thermopower via carrier energy filtering are explored. This work highlights the possibility of combining a diverse set of n- and p-type semiconductor matrices with

nanocrystals to engineer and optimize energy-dependent carrier scattering with the ease of solution-based materials processing.

Chapter 7 concludes this thesis work. The measurement of electronic and lattice contribution to the thermal conductivity is introduced as future work.

References

1. Orton, J. The Story of Semiconductors, *Oxford University Press*, New York, **2006**.
2. Elliot, S. R. Physics of Amorphous Materials, *Longman Scientific & Technical*, New York, **1990**.
3. Marshall, J. M. Carrier Diffusion in Amorphous Semiconductors. *Rep. Prog. Phys.*, **1983**, *46*, 1235-1282.
4. Orton, J. W.; Powell, M. J. The Hall Effect in Polycrystalline and Powdered Semiconductors. *Rep. Prog. Phys.*, **1980**, *43*, 81-1307.
5. Le Comber, P. G.; Jones, D. I.; Spear, W. E. Hall Effect and Impurity Conduction in Substitutionally Doped Amorphous Silicon. *Phil. Mag. B*, **1977**, *35*, 1173
6. Crupi, I. *et al.* Anomalous and Normal Hall Effect in Hydrogenated Amorphous Si Prepared by Plasma Enhanced Chemical Vapor Deposition. *J. App. Phys.*, **2010**, *107*, 043503.
7. Spear, W. E.; Le Comber, P. G. Investigation of the Localized State Distribution in Amorphous Si Films. *J. Non-Cryst.*, **1972**, 727-738.
8. Le Comber P. G.; Spear, W. E. Electronic Transport in Amorphous Silicon Films. *Phys. Rev. Lett.*, **1970**, *24*, 509-511.
9. Street, R. A. Hydrogenated Amorphous Silicon, *Cambridge University Press*, New York, **1991**.
10. Streetman B. G.; Banerjee, S. Solid State Electronic Devices, *Prentice Hall*, New Jersey, **2000**.
11. Li, Y.; Qian, F.; Xiang, J.; Lieber, C. M. Nanowire Electron and Optoelectronic Devices. *Mater. Today*, **2006**, *9*, 18-27.
12. Murray, C. B. *et al.* Colloidal Synthesis of Nanocrystals and Nanocrystal Superlattices. *IBM J. Res. & Dev.*, **2001**, *45*, 47-56.
13. Phillips, A. C. Introduction to Quantum Mechanics, *John Wiley & Sons*, New York, **2003**.

14. Vanmaekelbergh, D.; Liljeroth, P. Electron-Conducting Quantum Dots Solids: Novel Materials Based on Colloidal Semiconductor Nanocrystals. *Chem. Soc. Rev.*, **2005**, *34*, 299-312.
15. Collier, C. P.; Vossmeier, T.; Heath, J. R. Nanocrystal Superlattice. *Annu. Rev. Phys. Chem.* **1998**, *49*, 371-404.
16. Quinn, A. J.; Redmond G. Artificial Atom Solids Based on Metal Nanocrystals: Formation and Electronic Properties. *Prog. Solid State Chem.* **2005**, *33*, 263-277.
17. Banin, U.; Cao, Y.; Katz, D.; Millo, O. Identification of Atomic-Like Electronic States in Indium Arsenide Nanocrystal Quantum Dots. *Nature*, **1999**, *400*, 542-544.
18. Jdira, L. *et al.* Scanning Tunneling Spectroscopy on Arrays of CdSe Quantum Dots: Response of Wave Functions to Local Electric Fields. *Nano Lett.*, **2008**, *8*, 4014-4019.
19. Alivisatos, A. P. Semiconductor Clusters, Nanocrystals, and Quantum Dots. *Science*, **1996**, *271*, 933-937.
20. Kastner, M. A. Artificial Atoms. *Phys. Today*, **1993**, *46*, 24-31.
21. Ashoori, R. C. Electrons in Artificial Atoms. *Nature*, **1996**, *379*, 413-419.
22. Talapin, D. V.; Lee, J. -S.; Kovalenko, M. V.; Shevchenko, E. V. Prospects of Colloidal Nanocrystals for Electronic and Optoelectronic Applications. *Chem. Rev.*, **2010**, *110*, 389-458.
23. Schedelbeck, G.; Wegscheider, W.; Bichler, M.; Abstreiter, G. Coupled Quantum Dots Fabricated by Cleaved Edge Overgrowth: From Artificial Atoms to Molecules. *Science*, **1997**, *278*, 1792-1795.
24. Liljeroth, P. *et al.* Variable Orbital Coupling in a Two-Dimensional Quantum-Dot Solid Probed on a Local Scale. *Phys. Rev. Lett.*, **2006**, *97*, 096803.
25. Williams, K. J. *et al.* Strong Electronic Coupling in Two-Dimensional Assemblies of Colloidal PbSe Quantum Dots. *ACS Nano*, **2009**, *3*, 1532-1538.
26. Micic, O. I.; Ahrenkiel, S. P.; Nozik, A. J. Synthesis of extremely small InP Quantum Dots and Electronic Coupling in Their Disordered Solid Films. *Appl. Phys. Lett.*, **2001**, *78*, 4022-4024.
27. Artemyev, M. V. *et al.*, Optical Properties of Dense and Diluted Ensembles of Semiconductor Quantum Dots. *Phys. Stat. Sol.*, **2001**, *224*, 393-396.
28. Jiang, C. -W.; Green, M. A. Silicon Quantum Dot Superlattices: Modeling of Energy Bands, Densities of States, and Mobilities for Silicon Tandem Solar Cell Applications. *J. Appl. Phys.*, **2006**, *99*, 114902.
29. Lazarenkova, O. L.; Balabin, A. A. Miniband Formation in a Quantum Dot Crystal, *J. Appl. Phys.*, **2001**, *89*, 5509-5515.
30. Liu, Y. *et al.* Dependence of Carrier Mobility on Nanocrystal Size and Ligand Length in PbSe Nanocrystal Solids. *Nano Lett.*, **2009**, *10*, 1960-1969.
31. Lailhtman, B.; Wolf, E. L. Tunneling Time and Effective Capacitance for Single Electron

- Tunneling. *Phys. Lett. A*, **1989**, *139*, 257-260.
32. Drndic, M.; Jarosz, M. V.; Morgan, N. Y.; Kastner, M. A.; Bawendi, M. G. Transport Properties of Annealed CdSe Colloidal Nanocrystal Solids. *J. Appl. Phys.*, **2002**, *92*, 7498-7503.
 33. Parthasarathy, R.; Lin, X. M.; Jaeger, H. M. Electronic Transport in Metal Nanocrystal Arrays: The Effect of Structural Disorder on Scaling Behavior. *Phys. Rev. Lett.*, **2001**, *87*, 186807.
 34. Zabet-Khosousi, A.; Trudeau, P. -E.; Suganuma, Y.; Dhirani, A. -A. Metal to Insulator Transition in Films of Molecularly Linked Gold Nanoparticles. *Phys. Rev. Lett.*, **2006**, *96*, 156403.
 35. Mentzel, T. S.; Porter, V. J.; Geyer, S.; MacLean, K.; Bawendi, M. G.; Kastner, M. A. Charge Transport in PbSe Nanocrystal Arrays. *Phys. Rev. B*, **2008**, *77*, 075316.
 36. Talapin, D.; Murray, C. B. PbSe Nanocrystal Solids for n- and p-Channel Thin Film Field-Effect Transistors. *Science*, **2005**, *310*, 86-89.
 37. Steiner, D. *et al.* Electronic Structure and Self-Assembly of Cross-Linked Semiconductor Nanocrystal Arrays. *Nanotechnology*, **2008**, *19*, 065201.
 38. MacDonald, D. K. C. Thermoelectricity: An Introduction to the Principles. *John Wiley & Sons*, New York, **1962**.
 39. Pollock, D. D. Thermoelectricity: Theory, Thermometry, Tool, *ASTM*, Philadelphia, **1985**.
 40. Nolas, G. S.; Sharp, J.; Goldsmid, H. J. Thermoelectrics: Basic Principles and New Materials Developments, *Springer*, Germany, **2001**.
 41. Fritzsche, H. A General Expression for the Thermoelectric Power. *Sol. Stat. Comm.*, **1971**, *9*, 1813-1815.
 42. Kittel, C. Introduction to Solid State Physics, *John Wiley & Sons*, New York, **1996**.
 43. Rowe, D. M. CRC Handbook of Thermoelectrics, *CRC Press*, New York, **1995**.
 44. Bell, L. E. Cooling, Heating, Generating Power, and Recovering Waste Heat with Thermoelectric Systems. *Science*, **2008**, *321*, 1457-1461.
 45. Snyder, G. J.; Toberer, E. S. Complex Thermoelectric Materials. *Nature Mat.*, **2008**, *7*, 105-114.
 46. Venkatasubramanian, R.; Siivola, E.; Colpitts, T.; O'Quinn, B. Thin-Film Thermoelectric Devices with High Room-Temperature Figures of Merit. *Nature*, **2001**, *412*, 597-602.
 47. Harman, T.C. *et al.* Quantum Dot Superlattice Thermoelectric Materials and Devices. *Science*, **2002**, *297*, 2229-2232.
 48. Hicks, L. D.; Dresselhaus, M. S. Thermoelectric Figure of Merit of a One-Dimensional Conductor. *Phys. Rev. B*, **1993**, *47*, 16631.
 49. Mahan, G. D.; Sofo, J. O. The Best Thermoelectric. *Proc. Natl. Acad. Sci.*, **1996**, *93*, 7436-7439.
 50. Shakouri, A. Thermoelectric, Thermionic, Thermophotovoltaic Energy Conversion. *Int.*

Conf. Thermoelect., **2005**, 492–497.

51. Heremans, J. P. *et al.* Enhancement of Thermoelectric Efficiency in PbTe by Distortion of the Electronic Density of States. *Science.*, **2008**, *321*, 554–557.

52. Heremans, J.; Thrush, C. M. Thermoelectric Power of Bismuth Nanowires. *Phys. Rev. B.*, **1999**, *59*, 12579–12583.

53. Kanatzidis, M. G. Nanostructured Thermoelectrics: The New Paradigm? *Chem. Mater.*, **2010**, *22*, 648-659.

54. Minnich, A. J.; Dresselhaus, M. S.; Ren, Z. F.; Chen, G. Bulk Nanostructured Thermoelectric Materials: Current Research and Future Prospects. *Energy Environ. Sci.*, **2009**, *2*, 466-479.

2. Electronic conduction and thermopower in semiconductor nanocrystal solids

2.1 Introduction

At first glance, one could easily conclude that amorphous material systems may never behave as a semiconductor due to lack of a periodic lattice. However, the key concept in understanding the electronic properties of non-crystalline material is that no real solid is truly amorphous. In many amorphous semiconductors, amorphous silicon for example, fairly well defined short range order exists. Interestingly, amorphous silicon has an optical bandgap similar to crystalline silicon in spite of variations in bond lengths, angles, and the presence of dangling bonds distorts long range order. Random variation of the environment affects the energy of defects and creates a broad distribution of localized states at the band tail as shown in Figure 1.1(c). This is also reflected as a broad onset of optical absorption which is known as the Urbach region.^[1] Due to the lack of periodicity, however, electrons in amorphous systems cannot be described using Bloch wave functions to derive conventional band diagrams. The solution to this problem is to describe the electronic structure of amorphous systems using a density of states verses energy diagram, as shown in

Figure 1.1(c). The density of states versus energy diagram for a nanocrystal solid is expected to have a similar electronic structure. The highest and lowest energy state that holes and electrons can occupy will be broadened due to variations in size (variation in confinement energy) and most of energy states involved in transport are localized due to a high degree of disorder present in the system. The following chapters discuss carrier transport models in amorphous materials which can also be applied to semiconductor nanocrystal solids.

2.2 Physics of amorphous materials

There are two representative models^[1] that describe electron and hole transport in a disordered systems with mobility values far below the theoretical limit ($< 5 \text{ cm}^2/\text{Vs}$) dictated by scattering at each atomic point. The first is referred to as the multiple trapping model^[2,3] where band-like electronic transport occurs near the mobility edge. However, just below the mobility edge, localized band-tail states act as shallow traps. Charge carriers are trapped and thermally excited (released) back to the mobility edge multiple times while traveling through the lattice, which accounts for the low mobility value observed. An alternative view is given by the thermally-assisted hopping model where electrons or holes transport via hopping near the

localized band-tail states without being thermally excited to the mobility edge.^[4-5]

Whether the transport occurs via hopping or through multiple trapping near mobility edge depends critically on the electronic density of states, Fermi energy, and temperature. In the case where the Fermi level is far below the mobility edge and the density of localized band-tail states is high, there is greater wave function overlap (stronger exchange coupling) and hopping conduction dominates electronic transport. At the other extreme, if the density of localized state is low and the Fermi level is close enough to mobility edge, thermal excitation to the extended states and the multiple trap and release processes outweigh the hopping. Extensive electrical conductivity and thermopower studies of doped hydrogenated amorphous silicon reveal that below 600 K, carrier transport is dominated by hopping below the mobility edge.^[5]

Conduction involving localized states takes place by transition of an electron from a filled state to the empty state, usually with assistance from phonons (if the electrons are hopping to energy states with different energy). This mechanism of hopping conduction originates from heavily doped (the wave functions of the impurity states significantly overlap) and compensated (empty states are available) semiconductors. This model was extended to describe the transport in amorphous semiconductors in which conduction occurs at the localized band-tail states. A simple

model was given by Mott^[6] where the rate of hopping is given in equation (3) with an additional Arrhenius term accounting for the energy difference in electronic states (ΔE) for the upward hop:

$$\begin{aligned} \Gamma &= \Gamma_0 \exp[-k(d+2R)] \exp\left[\frac{\Delta E}{kT}\right] && : \text{upward hop} \quad \dots\dots\dots(16) \\ \Gamma &= \Gamma_0 \exp[-k(d+2R)] && : \text{downward hop} \end{aligned}$$

The diffusion coefficient from the random diffusive motion of a carrier is given by $D = \Gamma(d+2R)^2/6$. Using the Einstein–Smoluchowski relation in equation (5) gives the mobility of the hopping conduction as

$$\mu = \frac{e(d+2R)^2}{6k_B T} \Gamma_0 \exp[-k(d+2R)] \exp\left[-\frac{\Delta E}{kT}\right] \dots\dots\dots(17)$$

The first exponential term indicates the spatial disorder arising from variation in exchange coupling. For nanocrystal solids this is an inherent property already determined from assembly process (as well as chemical or heat treatments). The second exponential term specifies the energetic disorder of electronic states due to nanocrystal size variation. Equation (17) indicates that as the temperature increases, mobility increases. In contrast, bulk-like transport shows a reduction in mobility as the temperature increases due to enhanced electron-phonon scattering.^[7] Competition between the two exponential terms results in two different hopping conductivity

mechanisms.^[8] For $k(d+2R) > \Delta E/k_B T$, hopping occurs via nearest neighbor energy levels. The electrical conductivity for thermally-activated nearest-neighbor hopping is given as,

$$\sigma = eN(E) \exp\left(\frac{E_T - E_F}{k_B T}\right) \frac{e(d+2R)^2}{6k_B T} \Gamma_0 \exp[-k(d+2R)] \exp\left[-\frac{\Delta E}{kT}\right] \dots (18)$$

where $N(E)$ is the effective density of states of the electronic states involved in transport, E_F is the Fermi level, and the first exponential term indicates the activation energy for charge carrier generation. On the other hand, if $k(d+2R) < \Delta E/k_B T$, which typically occurs well below the room temperature, the number and the energy of phonons are both small. Thus, hopping to the nearest-neighbor that involves large energy variations (ΔE) becomes unfavorable. Rather, there is a higher probability of finding a distant energy level with a lower energy variation. Thus, electron hops to a larger distance, which is known as variable-range hopping. Optimizing the spatial term $\exp[-k/(d+2R)]$ and the energetic term $\exp[-\Delta/k_B T]$ gives the optimal distance with the characteristic temperature-dependence of electrical conductivity of $\ln\sigma \sim T^{1/4}$. For a system with additional electron-electron interactions, the Efros–Shklovskii variable-range hopping model predicts $\ln\sigma \sim T^{1/2}$.

The thermopower is defined as the entropy transport with a charge carrier per unit charge (see section 1.4). This entropy is divided into two components.^[9] The first

is the configuration entropy (S_{config}) which is estimated by adding n number of charge carriers across the density of states gap to the N number of available states. This procedure is identical to the calculation of entropy of mixing using the Boltzmann formula and Stirling's approximation^[10] as

$$S_{config} = k_B \ln \left(\frac{1-c}{c} \right) \dots \dots \dots (19)$$

where $c = n/N$ is the carrier concentration. Relating the Fermi function to the carrier concentration term ($c = 1/[\exp(E - E_F)/kT+1]$), the thermopower is simply given as

$$S_{config} = k_B \left[\frac{E - E_F}{k_B T} \right] \dots \dots \dots (20)$$

This equation is known as the Heikes formula derived for non-interacting charge carriers and it is valid irrespective of the transport mechanism. The second entropy term ($S_{transport}$) takes into account the net energy transferred as the carrier hops between inequivalent energy levels, which depends on the transport mechanism.

Emin^[11] derived the phonon-assisted hopping motion as

$$S_{transport} = \frac{1}{eT} \left[(E_f - E_i) \frac{(\lambda_i - \lambda_f)}{(\lambda_i + \lambda_f)} \right] \dots \dots \dots (21)$$

where E_f and E_i are the final and initial energy levels, and λ_f and λ_i are the electron-

phonon coupling strength of final and initial energy levels, respectively. Considering a nearly equal number of upward and downward hops, this term is generally neglected.^[12] Thus, the final form for thermopower in which charge carriers first have to be thermally excited to the transport level and then hops to the nearest-neighbor is identical to the previous equation (9).

2.3 Measurement of electrical and thermoelectric properties

The performance of a thermoelectric generator or refrigerator is determined by the figure of merit Z which consists of three materials inherent parameters: electrical conductivity (σ), thermopower (S), and thermal conductivity (k). Although direct measurement of all three parameter is preferred, sometimes it is necessary to perform independent measurements on each materials parameter. For instance, in rapid screening of new material combinations as well as optimization of carrier concentration, separate measurements are required and are routine in the actual production of thermoelectric materials.

Measurement of electrical conductivity has been practiced for a long time and there are two major sources of error identified that obstructs accurate measurements.^[13,14] First is the contact resistance arising from improper connection

between the electrode and the sample. This is especially important for samples with low resistivity (and most of the optimized thermoelectric materials are degenerate semiconductors and therefore have low resistivity). In order to avoid contact resistance (R_C), a four-contact technique is generally used (Figure 2.1(a)). Since the resistance from the contact (as well as measurement wires) and the sample is connected in series, current is same at all points. Measuring the voltage drop directly across the sample with two separate probes provides the resistance of the sample alone. Another error arises in the measurement of samples' conductivity due to the Peltier effect imposing a temperature gradient across the sample. This temperature gradient, in turn, generated thermo-voltage (Seebeck voltage) across the sample. In order to avoid this error, a current reversal method is used especially in the van der Pauw resistivity measurement. The van der Pauw resistivity measurement is widely used in the semiconductor industry to measure thin films of an arbitrary shaped sample (Figure 2.1(b)). A contact is placed at each corner and the current is applied across contact 1 and 2 (I_{12} , current is applied in a regime where current-voltage response is linear and the Joule heating is less than 5 mW) while simultaneously measuring the voltage across 3 and 4 (V_{43}). The direction of the current is then reversed (I_{21}) and the voltage V_{34} is measured. Averaging these two measurements eliminates the thermo-voltage. Defining $R_A = (V_{43}/I_{12} - V_{43}/I_{21})/2$ and $R_B = (V_{14}/I_{23} -$

$V_{14}/I_{32})/2$, sheet resistance R_S is obtained through solving $\exp(-\pi R_A/R_S) + \exp(-\pi R_B/R_S) = 1$. The bulk resistivity is then $\rho = R_S t$, where t is the thickness of the film. The van der Pauw resistivity measurement is usually accompanied with Hall effect measurements to extract carrier type, concentration and mobility. The Hall effect is measured using the same van der Pauw geometry with current I_{13} and by measuring the voltage V_{24} under an applied magnetic field. The measured Hall voltage is affected by the offset voltage arising from the voltage contact 2 and 4 being misaligned from the equipotential line.^[15] To eliminate the offset voltage, a magnetic field reversal method as well as geometric averaging is usually employed. This also eliminates other spurious magnetothermal effects such as Ettingshausen and Righi-Leduc effects.^[16] A total of eight voltage measurements are performed as

$$\begin{aligned}
 V_A &= V_{24P} - V_{24N} & V_B &= V_{42P} - V_{42N} \\
 V_E &= V_{13P} - V_{13N} & V_F &= V_{31P} - V_{31N} \quad \dots\dots\dots(22)
 \end{aligned}$$

where the P and N subscripts denote positive and negative polarity of the magnetic field, respectively. The carrier concentration (n) is inversely proportional to the field and geometric averaged Hall voltage by

$$n = \frac{IB}{q \frac{(V_A + V_B + V_C + V_D)}{8} t} \dots\dots\dots(23)$$

where B is the magnetic field. With the known resistivity of the sample, carrier mobility (μ) can be calculated as $\mu = 1/enp$.

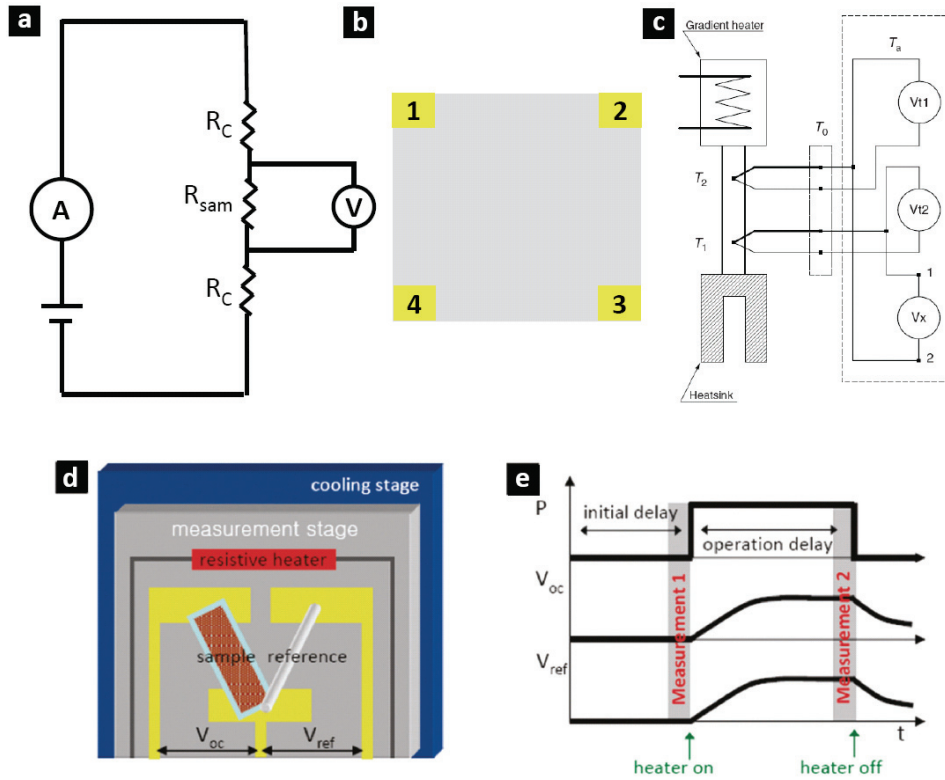


Figure 2.1 Schematic diagram of (a) four-contact technique, (b) van der Pauw geometry for resistivity and Hall effect measurement, and (c) thermopower measurement using differential method (adapted from reference [13]). (d) and (e) is the schematic illustration of temperature-dependent thermopower measurement described in the text.

There are two conventional methods for thermopower measurement.^[13] First is the integral method, which is the simplest way to measure thermopower. However, this method is not widely used due to the major limitation that the sample should be prepared as a long wire (for more detail see reference [13]). On the other hand, the

differential method can be applied to wide range of sample geometries (Figure 2.1(c)).

This method applies a temperature difference between two points of the sample and measures the thermopower after steady-state is achieved. The measured voltage difference across temperature point T_1 and T_2 is the sum of the entire material junction as

$$\Delta V = -\left(\int_{T_a}^{T_0} S_{Cu} dT + \int_{T_0}^{T_1} S_{ref} dT + \int_{T_1}^{T_2} S_x dT + \int_{T_2}^{T_0} S_{ref} dT + \int_{T_0}^{T_a} S_{Cu} dT\right) \dots\dots(24)$$

where S_{Cu} , S_{ref} , and S_x is the thermopower (Seebeck coefficient) of copper, the reference and the sample, respectively. This simplifies to the following equation

$$\Delta V = -\int_{T_1}^{T_2} (S_x - S_{ref}) dT \dots\dots\dots(25)$$

$$S_x(T_{avg}) = -\frac{\Delta V}{\Delta T} + S_{ref}(T_{avg})$$

where $T_{avg} = (T_1 + T_2)/2$.

For accurate temperature-dependent thermopower measurements, the applied temperature difference ΔT generated from the heater should be small (~1.5 K). This is to ensure that the applied ΔT does not perturb the sample temperature (Figure 2.1(d)). Accurate measurement of a small thermo-voltage (due to small ΔT) may be hindered by other thermo-voltages generated from wires, connectors, and instrument electronics. These typically contribute as the major sources of error. These errors can be eliminated by taking two measurements at different heater power outputs,^[16] as

shown in Figure 2.1(e) . The measured open-circuit voltage V_{oc} of the sample and the reference voltage V_{ref} (constantan) at two different heater outputs (P_1 and P_2):

$$\begin{aligned}
 V_{oc}(P_1) &= S_{sam} \Delta T(P_1) + \Delta V_{error}^{sam} \\
 V_{ref}(P_1) &= S_{ref} \Delta T(P_1) + \Delta V_{error}^{ref} \\
 & \dots\dots\dots(26) \\
 V_{oc}(P_2) &= S_{sam} \Delta T(P_2) + \Delta V_{error}^{sam} \\
 V_{ref}(P_2) &= S_{ref} \Delta T(P_2) + \Delta V_{error}^{ref}
 \end{aligned}$$

The error voltages arising from sample measurement ΔV_{error}^{sam} and the reference measurement ΔV_{error}^{ref} are constant for two power outputs since the heat is applied only in proximity to the sample and the reference junction. Eliminating ΔV_{error}^{sam} and ΔV_{error}^{ref} by taking the difference of the two voltage measurements results in an accurate value of the sample's thermopower:

$$S_{sam} = S_{ref} \frac{[V_{oc}(P_1) - V_{oc}(P_2)]}{[V_{ref}(P_1) - V_{ref}(P_2)]} \dots\dots\dots(27)$$

2.4 Conclusion

Nanocrystal solids as active electronic and thermoelectric devices are still in the development stage. The present challenge in nanocrystal solids is improvement of the low carrier mobility which limits their performance as charge transport systems. However, the ultimate goal may not be a system that resembles 3D bulk-like extended

systems, because delocalization will decrease the unique property of quantum confined features in nanocrystal solids from which many devices, including thermoelectrics and photovoltaics, benefit. Thus, efforts toward a new materials design in coordinated arrays of nanocrystals as well as device architectures which embrace both features are needed.

On the other hand, a view from the other side provides an unprecedented opportunity for novel device design. Even in an ideally exchange coupled nanocrystal solid, the presence of an external electric field causes each energy level to shift (field-induced band-bending corresponding to bulk), increasing the energy level offset. At a certain threshold electric field ($h\Gamma < \Delta E_S$), this may disrupt the formation of minibands and cause localization of electrons at each nanocrystal.^[17,18] Transition from delocalized to localized electronic structure can be reversibly switched by applying external electric field. This offers additional materials functionality to manipulate the electronic structure itself, a control not present in bulk semiconductor systems.

References

1. Pankove, J. I. Semiconductors and Semimetals: Hydrogenated Amorphous Silicon, Vol 21, Part B, *Academic Press*, London, **1984**.

2. Tiedje, T.; Rose, A. A Physical Interpretation of Dispersive Transport in Disordered Semiconductors, *Sol. Stst. Comm.*, **1980**, *37*, 49-52.
3. Orenstein, J.; Kastner, M. Photocurrent Transient Spectroscopy: Measurement of Density of Localized States in a-As₂Se₃. *Phys. Rev. Lett.*, **1981**, *46*, 1421-1424.
4. Mott, N. F. Conduction in Glasses Containing Transition Metal Ions, *J. Non-crystl. Solids.*, **1968**, *1*, 1-17.
5. Dohler, G. H. Conductivity, Thermopower, and Statistical Shift in Amorphous Semiconductors. *Phys. Rev. B*, **1979**, *19*, 2083-2091.
6. Elliot, S. R. Physics of Amorphous Materials, *Longman Scientific & Technical*, New York, **1990**.
7. Kittel, C. Introduction to Solid State Physic, *John Wiley & Sons*, New York, **1996**.
8. Parfenov, O. E.; Shklyaruk, F. A. On the Temperature Dependence of the Hopping Thermopower in Disordered Semiconductors. *Semiconductors*, **2006**, *41*, 1021-1026.
9. Rowe, D. M. Thermoelectrics Handbook: Macro to Nano. *Taylor & Francis Group*, New York, **2006**.
10. Tilley, R. J. D. Principle and Application of Chemical Defects, *Stanley Thornes Ltd.*, United Kingdom, **1998**.
11. Emin, D. Thermoelectric Power Due to Electronic Hopping Motion. *Phys. Rev. Lett.*, **1975**, *35*, 882-885.
12. von Mühlhelen, A.; Errien, N.; Schaer, M.; Bussac, M. N.; Zuppiroli, L. Thermopower measurements on Pentacene Transistors. *Phys. Rev. B*, **2008**, *75*, 115338.
13. Rowe, D. M. CRC Handbook of Thermoelectrics, *CRC Press*, New York, **1995**.
14. Nolas, G. S.; Sharp, J.; Goldsmid, H. J. Thermoelectrics: Basic Principles and New Materials Developments, *Springer*, Germany, **2001**.
15. Marion, D.; Cristoloveanu, S.; Chovet, A. High Magnetic-Field Van Der Pauw Method: Magnetoresistance Measurement and Applications. *IEE Proc.*, **1982**, *129*, 125-16. Look, D. C. Electrical Characterization of GaAs Materials and Devices, *John Wiely & Sons*, Chichester, **1989**.
16. Resel, R; Gratz, E.; Burkov, A. T.; Nakama, T.; Higa, M.; Yagasaki, K. Thermopower Measurements in Magnetic Fields up to 17 T Using the Toggled Heating Method. *Rev. Sci. Instrum.*, **1996**, *67*, 1970–1975.
17. Artemyev, M. V. *et al.*, Optical Properties of Dense and Diluted Ensembles of Semiconductor Quantum Dots. *Phys. Stat. Sol.*, **2001**, *224*, 393-396.
18. Artemyev, M. V.; Woggon, U.; Jaschinski, H.; Gurionvich, L. I.; Gaponenko, S. V. Spectroscopic Study of Electronic States in an Ensemble of Close-Packed CdSe Nanocrystals. *J. Phys. Chem. B.*, **2000**, *104*, 11617-11621.

3. Synthesis and characterization of metal-chalcogenide nanocrystals

3.1 Introduction

Lead chalcogenide NC solids have been extensively studied for potentially cheap, high-performance electronic and optoelectronic devices including field-effect transistors,^[1,2] photodetectors,^[3] and solar cells.^[4] In this work, we chose lead telluride (PbTe), the most strongly quantum-confined binary semiconductor known with a large excitonic Bohr radius ($a_0 \sim 46$ nm).^[5] Well-developed synthetic procedures enable precise control over crystal size and shape providing a low dispersion of on-site energies. Along with large 4-fold band degeneracy and low charging energy E_C (using the static dielectric constant of bulk PbTe $\epsilon_{PbTe} \sim 1000$ for 7 nm spherical nanocrystal capped with oleic acid, $E_C \sim 0.5$ meV),^[6] PbTe is an ideal choice for transport studies. PbTe also shows the highest thermoelectric figure of merit for a single phase bulk material at ~ 300 - 400 °C^[7] and has been recently investigated as an interesting material system for nanostructures^[8,9] and nanocomposites^[10,11] with improved energy conversion efficiency. The other material chosen for doping studies is silver telluride (Ag₂Te), which is a well-known p-type dopant in PbTe bulk

compounds.^[7,12]

Bulk silver tellurides (Ag_2Te) with stoichiometric excess of silver show polymorphic transformations at around 145°C and 802°C with monoclinic (β), face-centered cubic (α), and body-centered cubic (γ) phases.^[13,14] The transition from semiconductor (β) to ionic conductor (α),^[15,16] large magnetoresistance in nonstoichiometric samples,^[17,18] and high electron mobility with low thermal conductivity (β)^[19] have drawn significant attention in materials research. There are more interesting physical properties to be explored, especially in the nanoscale regime where the crystal domain is smaller than the electronic (electrons, holes, and ions) and thermal transport scales. Ag_2Te with different geometries such as nanowires,^[20] nanotubes,^[21] nanorods,^[22] and nanoparticles^[23,24] has been previously reported. In this study, we investigate the structural, chemical and optical characterization of Ag_2Te NCs as a function of size.

3.2 Synthesis and characterization of lead-chalcogenide nanocrystals

Monodisperse PbTe nanocrystals are synthesized via hot-injection method developed by Murray.^[25] The synthesis is based on the reaction between two

precursors, lead oleate and trioctylphosphine-tellurium, in the presence of excess surfactants. The oleic acid and the trioctylphosphine (TOP) are bound to the metal and the chalcogenide, respectively, which controls the reaction rate. Surfactants also prevent uncontrolled growth of nanocrystals as well as aggregation between nanocrystals. Rapid injection of TOP-Te into a reaction vessel containing lead oleate, squalane (noncoordinating solvent), and excess oleic acid (surfactant) at high temperature, results in an abrupt supersaturation of PbTe monomer which is quickly relieved by a spontaneous nucleation event followed by the growth of nuclei (Figure 3.1). Separation of the nucleation and growth regime is critical in achieving a narrow distribution of nuclei as well as high monodispersity of the final product. The growth is divided into two regimes separated by the critical monomer concentration (C^*). Growth above this critical concentration is referred to a size focusing regime where nanocrystals grow at the expense of monomers in the reaction and the rate of nanocrystal growth is inversely proportional to the nanocrystal size.^[26] Larger nanocrystals grow slowly and the smaller nanocrystals grow rapidly decreasing the size distribution in the synthesis batch. Below the critical monomer concentration, the amount of leftover monomer in the reaction is not sufficient enough to maintain the growth. At this stage, known as the Ostwald ripening process,^[27] larger nanocrystals grow at the expense of smaller nanocrystals thus, increasing the polydispersity of the

nanocrystal size distribution. Additional injection of precursor (drop-wise injection to prevent additional nucleation) at this stage may raise the concentration of monomer above C^* , further focusing the nanocrystal distribution.^[28] This is indicated as the blue dotted line in Figure 3.1.

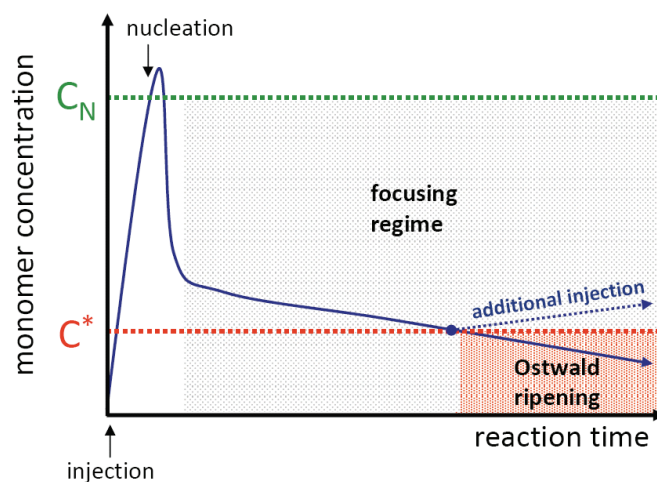


Figure 3.1 Schematic illustration of monomer concentration vs. reaction time for the synthesis of metal chalcogenide nanocrystal via hot injection. C_N denotes critical monomer concentration for the nucleation threshold and C^* indicates the concentration threshold for Ostwald ripening.

In a typical synthesis, 1.1379 g of lead acetate trihydrate and 2 mL of oleic acid (OA) are dissolved in 20 mL of squalane. This solution is heated to 100 °C under vacuum for the formation of lead oleate and removal of water and acetic acid. After heating the solution up to 180 °C, 4 mL of TOP-Te is swiftly injected and maintained at 173 °C for 1 minute. The reaction is then quenched using a water bath and the

nanocrystals are separated using hexane and acetone. A transmission electron microscopy (TEM) image of the resulting monodisperse nanocrystals with average size of $6.5 \text{ nm} \pm 0.4 \text{ nm}$ are shown in Fig. 3.2(a) and (b). There are two strategies to control the size of the nanocrystals. The first approach varies the growth time while keeping the growth kinetic constant^[29]. As discussed previously, additional injection of precursors while varying the growth time enables us to achieve different sizes of nanocrystals with the advantage of further focusing the size distribution as the nanocrystals grow. Fig. 3.2(c) is the optical absorption spectrum of PbTe nanocrystals obtained by the additional injection method, with size varying from 6.5nm to 8nm, showing the narrowing of full-width half-maximum (FWHM) of the first excitonic transition peak. The second approach modifies the growth kinetics, governed by the surfactant system, Pb to OA ratio, Pb to Te ratio, injection and growth temperature, while fixing the growth time^[30,31]. Changing the Pb or Te monomer activity also enables us to tune the growth kinetics. For example, by using HEPT-Te (hexaethylphosphorous triamide, HEPT) instead of TOP-Te, nanocrystals grow more rapidly. It is interesting to note that as the nanocrystals grow to a certain size ($\sim 12 \text{ nm}$ for this specific reaction), spherical nanocrystals starts to evolve to an equilibrium cubic shape^[30-32], typically, with an increase in polydispersity. This is shown in Fig. 3.2(d) and (e). Figure 3.2(f) shows the powder diffraction pattern obtained from 6.5

nm spherical PbTe nanocrystal assemblies identified as rock salt (Altaite) crystal structure (JCPDS 38-1435) with ~ 3.5 fold increase in I_{200}/I_{220} intensity ratio indicating preferred orientation of the $\{200\}$ plane perpendicular to the surface. The size estimated from Scherrer broadening is ~ 5 nm ($\{200\}$, FWHM = 1.6°). Chemical composition analysis using energy-disperse X-ray spectroscopy (EDS) shows an excess of Pb (Pb : Te = 1.14 : 1).

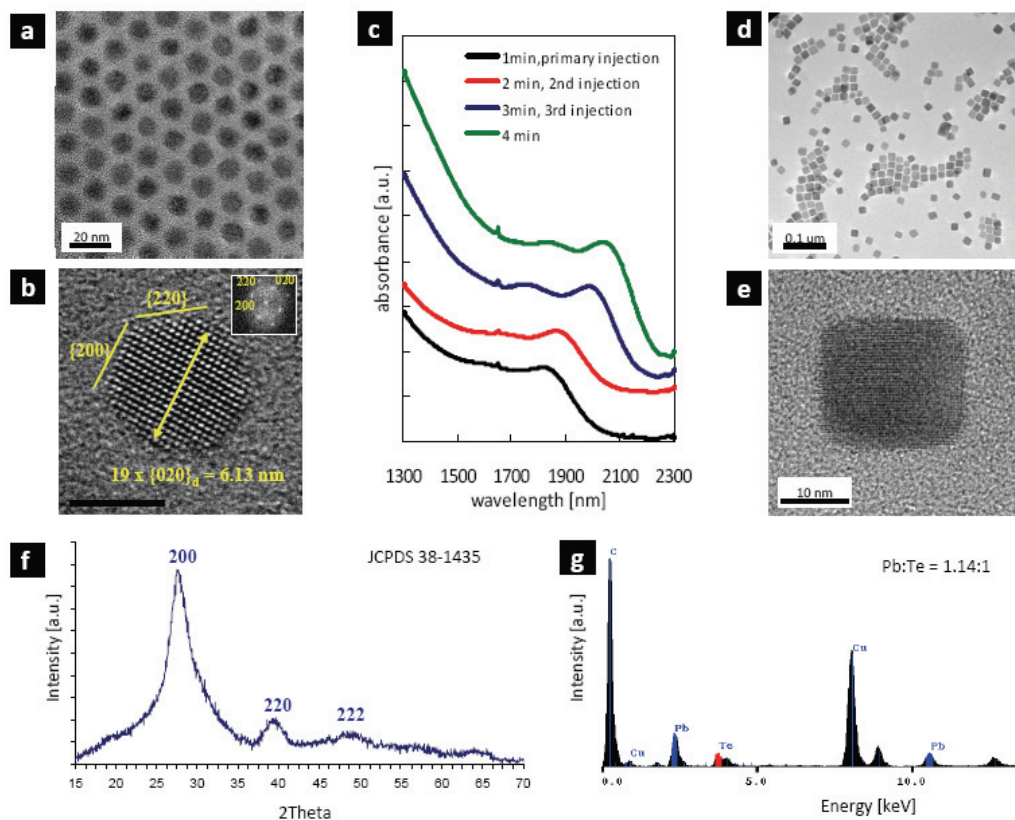


Figure 3.2 Structural, chemical, and optical analyses of PbTe nanocrystals. (a) TEM of as-synthesized monodispersed PbTe nanocrystals in ordered assembly. (b) HRTEM of PbTe nanocrystals, 6.12nm in diameter, showing truncated octahedron shape with distinct crystal facets. Inset shows 2D Fourier transform of the HR image. (c) Optical absorption spectrum of different sizes of PbTe nanocrystals dispersed in tetrachloroethylene (TCE). (d), (e) TEM of cubic PbTe nanocrystal synthesized using HEPT-Te. (f) XRD of PbTe nanocrystals (JCPDS 38-1435). (g) EDS spectrum of PbTe nanocrystal showing Pb : Te stoichiometry of 1.14 : 1.

3.3 Synthesis and characterization of silver telluride nanocrystals

The Ag_2Te nanocrystals were synthesized via rapid injection of trioctylphosphine-tellurium (TOP-Te) into a mixture of silver-dodecanethiol and 4-

tert-butyltoluene. Figure 3.3(a-f) and (g) shows the TEM images and the absorption spectra of Ag_2Te NCs as a function of growth duration. The aliquot retrieved at 10 min after injection of TOP-Te shows NCs with wide distribution of size and shape (Figure 3.3(a)) and a broad absorption feature (A in Figure 3.3(g)). After 1 hr of reaction, the sample shows bimodal distribution of large (6 - 10 nm) and small 3.1 nm NCs (Figure 3.3(b)) and a distinct absorption peak arising from small NCs starts to evolve (B in Figure 3.3(g)). Large NCs transform to a barrel shape (Figure 3.3(c)) with no distinctive absorption peaks (C in Figure 3.3(g)) while the small NCs do not show a change in their size. After 12 hr of reaction, large NCs grow and precipitate out from the solution leaving behind small NCs with consistent size and distribution (Figure 3.3(d) and D in (g)). Finally after 24 hr of reaction, the majority of large NCs form precipitates and separate to the bottom of the reaction vessel. These precipitates show mixtures of tabular and prismatic shapes which is commonly found in monoclinic minerals^[33, 34] (Figure 3.3(f)). In the reaction supernatant, monodisperse Ag_2Te nanocrystals with 3.1 nm in average size are obtained which form an ordered superlattice upon film deposition (Figure 3.3(e)). The nucleation and growth of Ag_2Te nanocrystals are significantly different from that of the well-established II-VI or IV-VI semiconductor synthesized via hot-injection where nanocrystals continuously grow from the nuclei through focusing and defocusing regimes. They are also different

from other anomalous growth processes previously reported, such as digestive ripening^[35] and magic size^[36] nanocrystals. It is worthy noting that the absorption spectrum obtained from 3.1 nm monodisperse NCs show distinct absorption peaks (E in Figure 3.3(g)) similarly observed in semiconductor nanocrystals with discrete quantized energy spectrum.

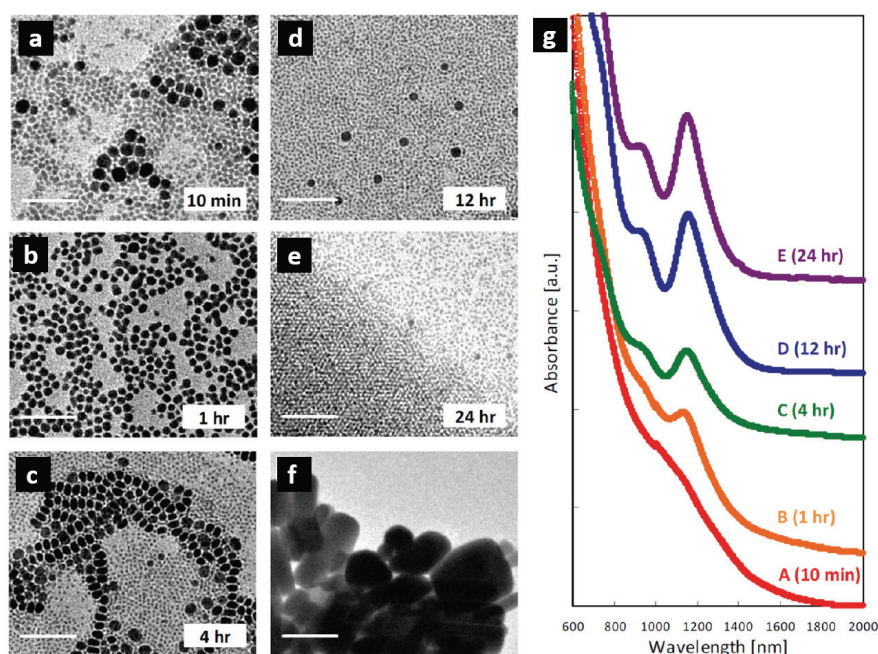


Figure 3.3 TEM images of Ag₂Te NCs obtained at different growth durations. (a) 10 min, (b) 1 hr, (c) 4 hr, (d) 12 hr, (e) 24 hr. (f) shows the precipitates obtained from 24 hr reaction. All scale bars are 50 nm. (g) Absorption spectra of corresponding Ag₂Te NCs at different growth durations.

For further chemical, structural and optical characterization, three different sizes of Ag₂Te NCs are extracted from the reaction. Monodisperse nanocrystals 3.1 nm in size and the precipitate were obtained from a 24 hr reaction. Large nanocrystals

6 -10 nm in size were withdrawn from a 1 hr reaction followed by size-selective precipitation. Figure 3.4(a-c) shows the TEM images of small NCs, large NCs, and precipitate, respectively. The chemical composition analysis using atomic emission spectroscopy indicates that the small monodisperse NCs have a large stoichiometric excess of silver (Ag:Te = 2.39:1). As the size increases, the amount of excess silver decreases but still remains as a silver-rich compound. It is expected that the nanocrystal surface is terminated with silver ions coordinated with the surfactant, resulting in a stoichiometric excess of silver.^[37,38] As the size increases, the surface to volume ratio decreases, reducing the Ag to Te ratio.

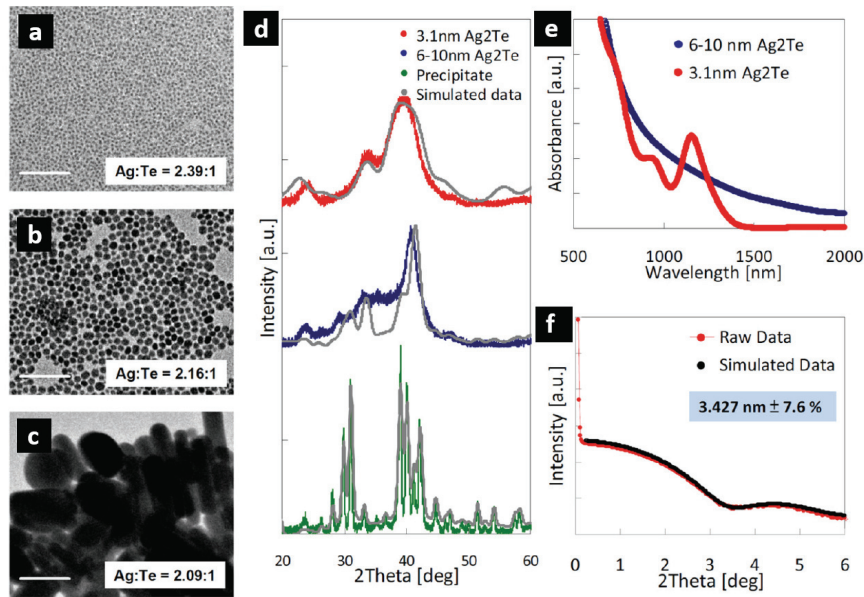


Figure 3.4 TEM image obtained from (a) monodisperse 3.1 nm NCs, (b) 6 ~ 10 nm NCs, and (c) precipitates of Ag_2Te . The stoichiometry is denoted in the inset. All scale bars are 50 nm. (d) Powder X-ray diffraction patterns and the corresponding simulation curves. (e) Absorption spectra obtained from the 3.1 nm and 6 ~ 10 nm Ag_2Te NCs. (f) The transmission small-angle X-ray scattering (SAXS) data obtained from Ag_2Te NCs shown in (a) and the simulation curve indicating the average size of 3.43 nm with the distribution of 7.6 %.

Structural characterization using power diffraction is shown in Figure 3.4(d).

The diffraction pattern obtained from the precipitate (extracted after the 24 hr reaction) is identical to the low temperature β - Ag_2Te (monoclinic, JCPDS: 081-1820) commonly found in bulk. Interestingly, for small NCs (obtained after 24 hr reaction), XRD pattern deviates from the β -phase and rather closely matches with the simulated structure of a 67% γ (BCC, JCPDS 081-1824) and 33% α (FCC, JCPDS 081-1821) phase mixture as shown in Figure 3.4(d). Both are high temperature phases that are not stable at room temperature according to the bulk phase diagram.^[14] However, the

phase equilibria in nanosystems may be dramatically different from the bulk counterpart which has been confirmed theoretically^[39] and experimentally.^[40, 41] This indicates that the γ and α nanocrystalline phases can be acquired at the reaction temperature (which is stable or metastable down to room temperature) with the Ag and Te composition mentioned above in the chemical analysis. For large NCs (obtained after 1 hr reaction), the XRD pattern was closely fitted to a simulated pattern composed of 67% γ and 33% β phase. Bulk α and γ Ag_2Te are ionic conductors that exhibits high silver ion mobility at a high temperature (above 802°C for the γ phase). However, Ag_2Te at room temperature obtained from colloidal synthesis may possess a different electronic structure and thus, further optical characterization is performed.

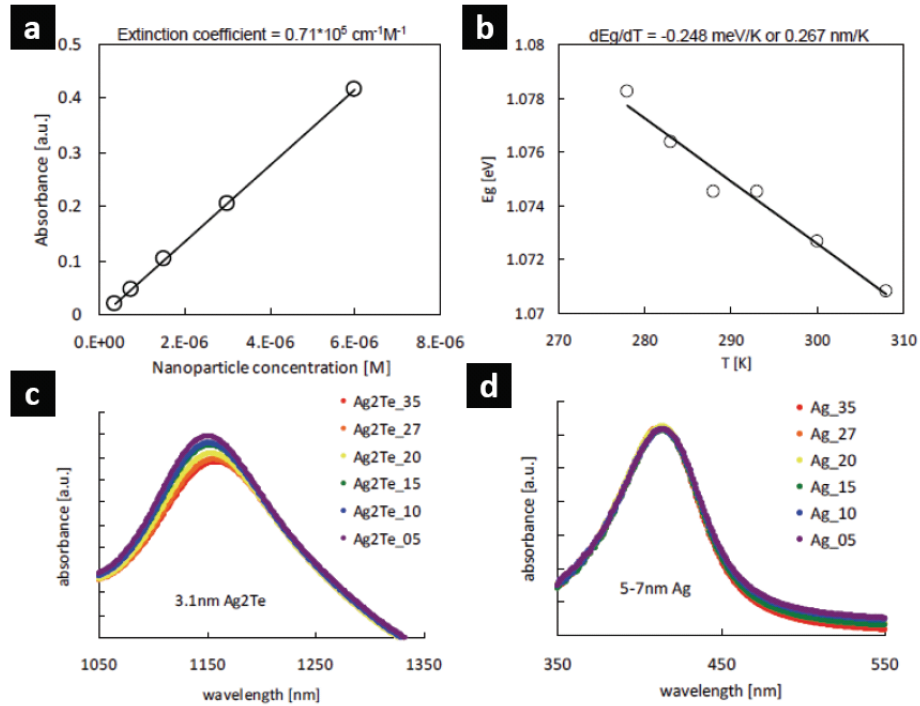


Figure 3.5 (a) Plot of absorbance vs. nanocrystal concentration to extract the extinction coefficient ($0.71 \times 10^5 \text{ cm}^{-1} \text{ M}^{-1}$) for monodisperse 3.1 nm Ag₂Te NCs. (b) The temperature-dependent shift of the optical bandgap in Ag₂Te NCs ($dE_g/dT = -0.248 \text{ meV/K}$ or 0.267 nm/K) and (c) the corresponding absorption as a function of temperature. (d) Absorption spectra of Ag NCs demonstrating that plasmonic absorption show negligible shift as a function of temperature.

The optical absorption spectra obtained from small and large Ag₂Te NCs are shown in Figure 3.4(e). Large nanocrystals show featureless absorption, possibly due to the polydispersity of the sample or the excitons not being quantum mechanically confined. A recent study on silver chalcogenide nanocrystals with high monodispersity are also reported to show similar broad absorption.^[23] On the other hand, small nanocrystals with 7.6% of size distribution (Figure 3.4(f)) show multiple distinct absorption peaks with the molar extinction coefficient of $7.1 \times 10^4 \text{ cm}^{-1} \text{ M}^{-1}$

(Figure 3.5(a), assuming bulk density of 8.318 g/cm^3 , calculated from the 1154 nm peak) as similarly observed for quantum confined semiconductor nanocrystals with discrete energy levels. In order to confirm that the optical absorption involves interband transitions, temperature-dependent optical gap measurements were performed. Ag_2Te NCs show significant blue shift as the temperature is lowered (Figure 3.5(b,d)), indicating the semiconducting nature of the material. Silver NCs, on the other hand, show negligible shift as a function of temperature (Figure 3(c)). Ag_2Te NCs also do not show apparent shift in absorption peak shift by varying the solvents with different dielectric constants (Figure 3.6).^[42]

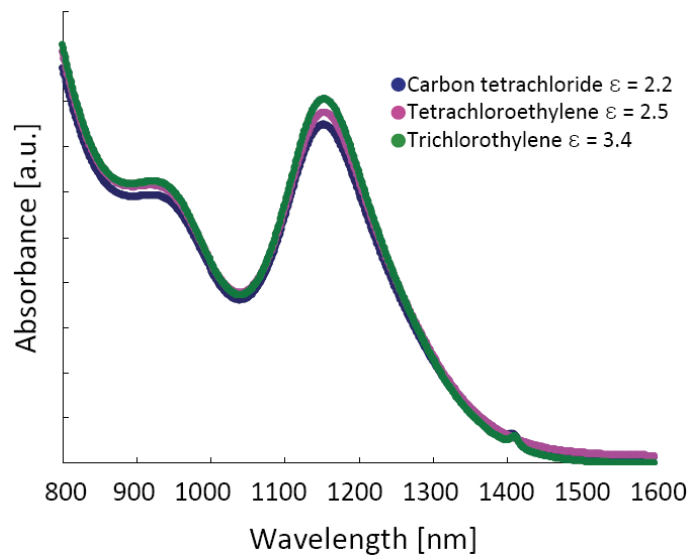


Figure 3.6 Absorption spectra obtained from monodisperse 3.1 nm Ag_2Te NCs dissolved in carbon tetrachloride (dielectric constant = 2.2), tetrachloroethylene (dielectric constant = 2.5) and trichloroethylene (dielectric constant = 3.4), showing that optical bandgap does not change with the dielectric constant of the surrounding medium.

3.4 X-ray structural characterization techniques

Structural characterizations of nanocrystals as well as their assemblies were performed using Rigaku Smartlab™ high-resolution diffractometer. Typical measurement configuration is shown in Figure 3.7. The left hand side of the sample holder is referred as “theta source arm” (denoted as Theta_s arm) which is composed of X-ray generator, incident beam focusing optics, and optical slits. The right hand side of the sample holder is referred as “theta detector arm” (denoted as Theta_d arm) which consists of receiving beam optics, slits, automatic attenuator and a X-ray detector.

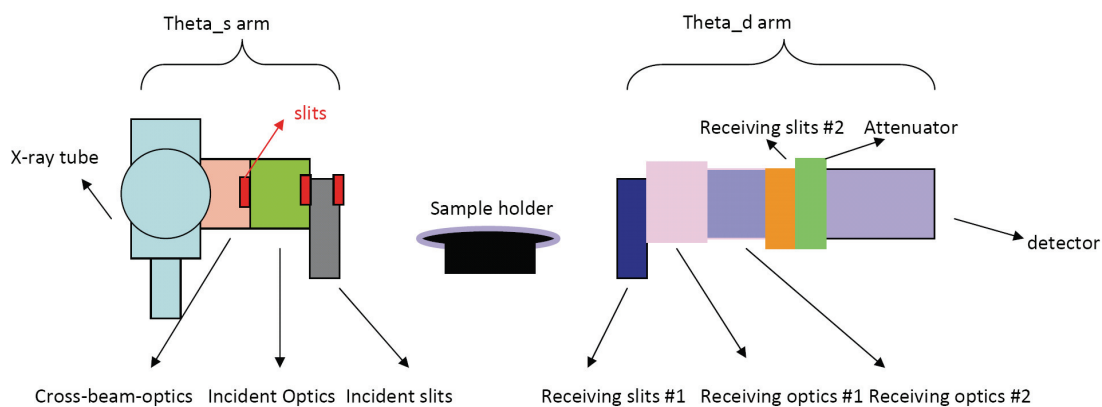


Figure 3.7 Measurement configuration of Rigaku Smartlab™ horizontal mount X-ray diffractometer.

A 2.2KW fixed tube X-ray source is typically mounted to operate under 40 kV / 44 mA condition. The anode target is subjected to a stream of focused electron

beam emanating from the cathode and accelerated due to the high potential bias (high tension, HT) applied across two electrodes. Since 99% of the incident electrons are converted to heat, heat dissipation at the focal spot on the target limits the maximum X-ray generation. A rotating anode can also be installed to improve the X-ray intensity by sweeping the anode and spreading the heat load over larger area (Figure 3.8 (a) and (b)).

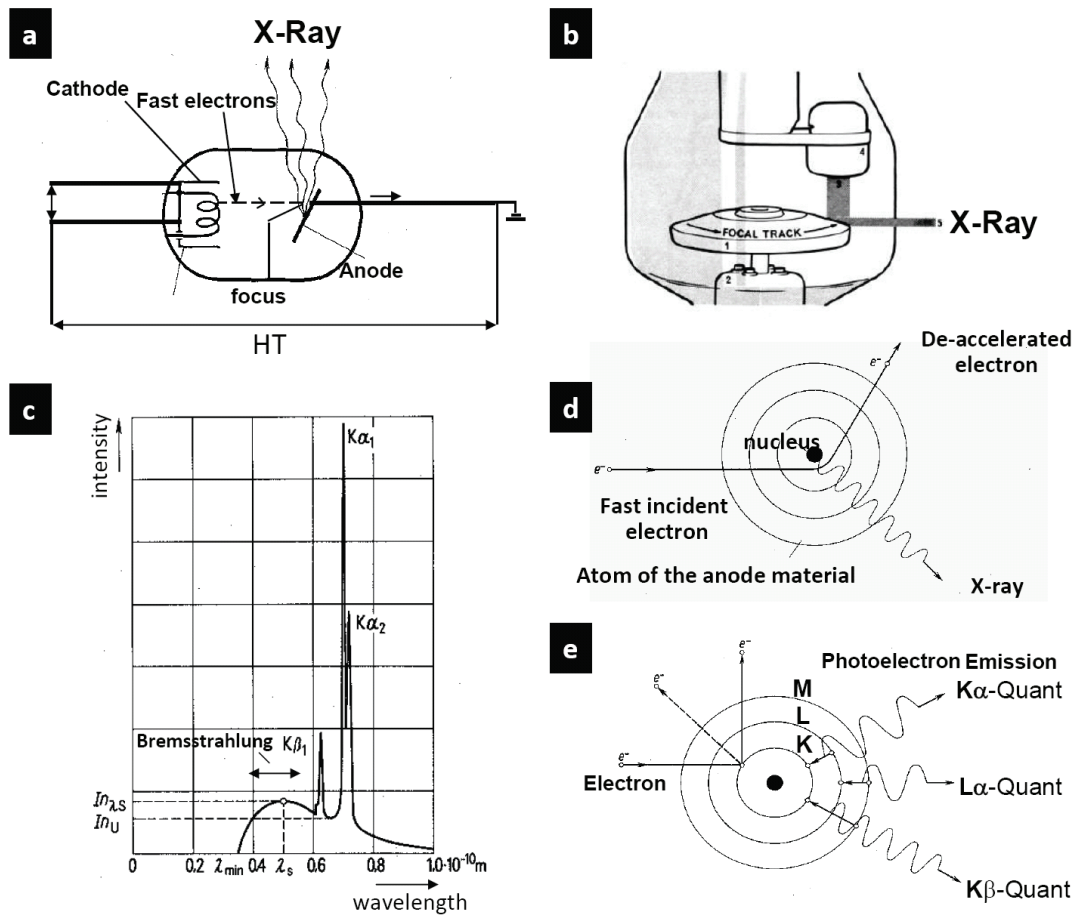


Figure 3.8 Schematic of X-ray generation using a Cu target. (a) Fixed tube X-ray generator. (b) Rotating anode X-ray generator. (c) X-ray spectrum generated using Cu target. (d) Generation of the white X-ray or Bremsstrahlung continuum. (e) Characteristic X-ray emission from Cu target. (Adapted from reference [43])

When a stream of electrons bombard the target anode, for Cu in this specific example, a broad spectrum followed by several sharp peaks of X-ray is generated (Figure 3.8 (c)). The first broad X-ray, also known as the white X-ray or Bremsstrahlung continuum (Figure 3.8 (d)), is generated due to the de-acceleration of electrons around the anode materials' nucleus. This usually produces a broad

background superimposed on the diffraction data. Three sharp radiations, denoted as $K_{\beta 1}$, $K_{\alpha 1}$, and $K_{\alpha 2}$, are the characteristic X-ray emitted from Cu atomic transitions (Figure 3.8 (e)). Among three peaks, $K_{\alpha 1}$, which shows the highest intensity (intensity ratios, $K_{\alpha 1}:K_{\alpha 2}:K_{\beta 1} = 10:5:2$), is used for diffraction measurements.

Two focusing methods are employed to refine the X-ray beam from a divergent source. First is the Bragg-Brentano focusing (parafocusing) with 2θ - θ or θ - θ geometry.^[44] Smartlab uses θ - θ geometry (Figure 3.9(a)) where the sample is stationary in the horizontal position and the X-ray source (incident beam) as well as the detector (receiving beam) moves in a circle that is centered at the sample. Soller slits are used to limit the angular divergence of the source and the angular acceptance of the detector. In this setup, Ni foil is inserted at the receiving arm to remove the $K_{\beta 1}$ peak. The $K_{\alpha 2}$ peak has to be removed manually after the data collection. Second is the parallel beam focusing which uses a curved and graded multilayer mirror (Göbel mirror, Figure 3.9 (b)) to generate parallel X-ray beam.^[45] The multilayer mirror also serves as a monochromator due to the layer thickness gradient which removes both $K_{\beta 1}$ and $K_{\alpha 2}$ peaks simultaneously.

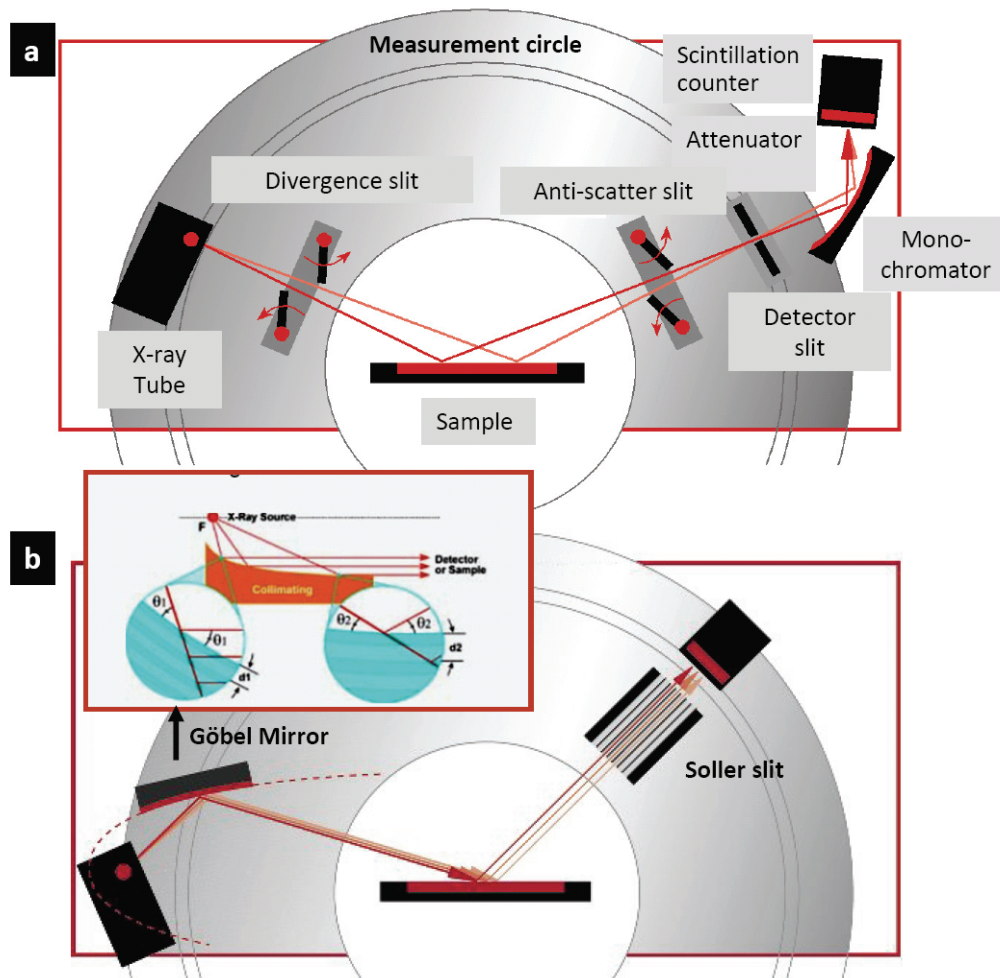
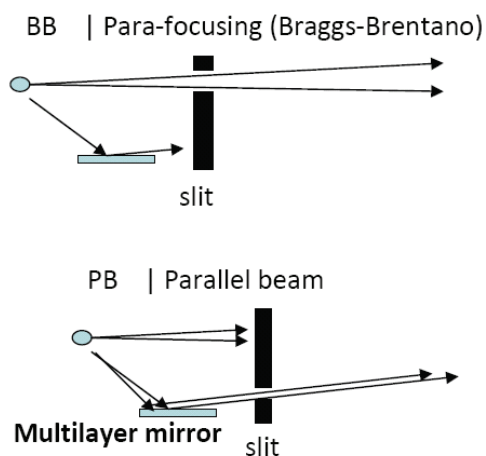


Figure 3.9 (a) Bragg-Brentano (para-focusing) geometry. (b) Parallel-beam focusing using multilayered (Göbel) mirror. (Adapted from reference [43])

In Smartlab, a selection slit is inserted into the cross-beam optic slot (Figure 3.7). The BB selection slit has an opening above the center point (Figure 3.10) where the diverging X-ray beam is refined using Soller slits. The PB selection slit has an opening below the center point and the X-ray beams reflected from the multilayer mirror is collected (Figure 3.10). Slits with narrower width and length can be used for small angle and micro-area experiments.



Selection Slits	
BB	Para-focusing (Braggs-Brentano)
PB	Parallel beam
SA	Small angle scattering
MA	Micro-area
SA01	Small angle high intensity

Figure 3.10 Selection slits for BB and PB focusing. A list of selection slit is also shown for small angle and micro-area experiments.

For BB focusing, the sample surface should be smooth, flat and should also be at the correct height. If the sample height is outside the rotation axis, shifts in diffraction peaks occur (Figure 3.11(a)). On the contrary, PB focused beam is insensitive to the sample height and surface (Figure 3.11(b)).

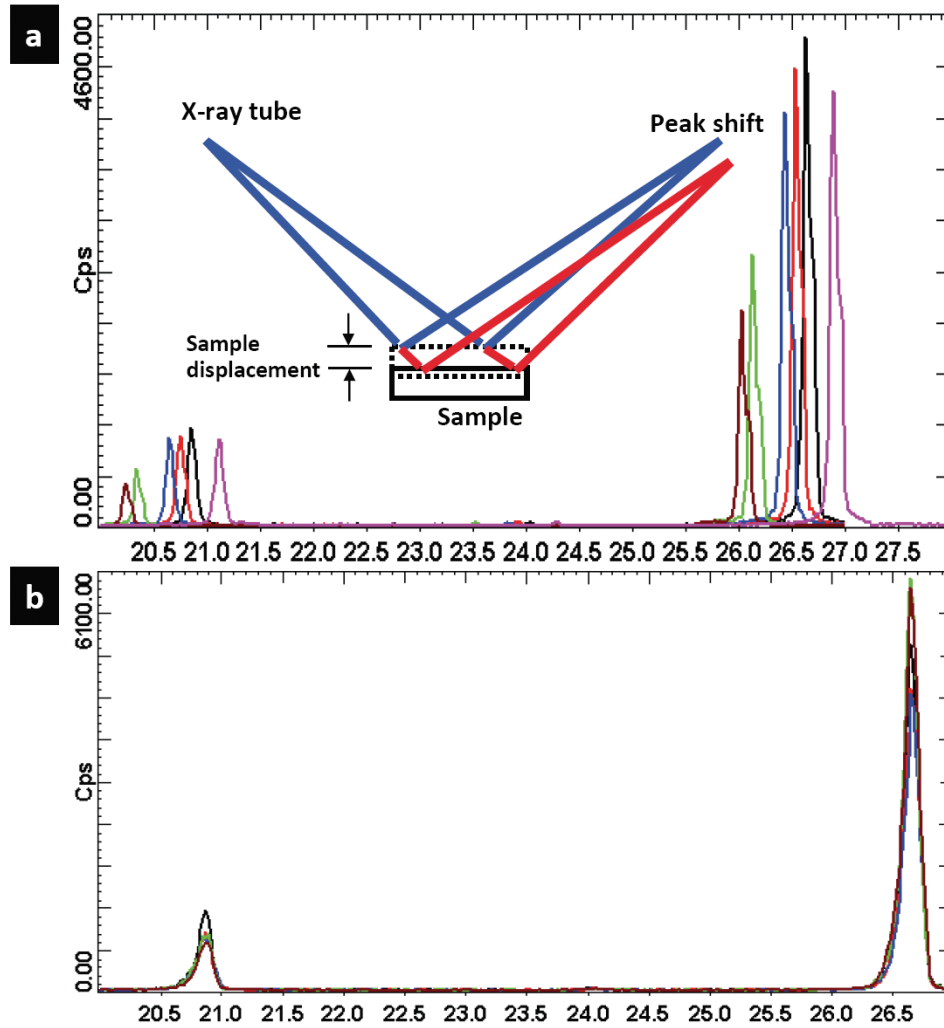


Figure 3.11 Shifts in diffraction peaks as a function of sample height for (a) BB focusing and (b) PB focusing. (Adapted from reference [43])

Three different X-ray optics can be mounted on incident optic slot at source arm depending on the measurement configuration Soller slit which uses closely spaced parallel plates to reduce the beam divergence angle (Figure 3.7(a)). Monochromators selectively collect diffracted beam from a single crystal with one wavelength. Single crystal germanium with (220) or (400) orientation can be used in two-bounce (Figure 3.12(b) or four-bounce (Figure 3.12(c)) configurations. Narrower

Soller slits as well as higher bounce monochromators increase the peak resolution but reduces the intensity (Figure 3.12(d)).

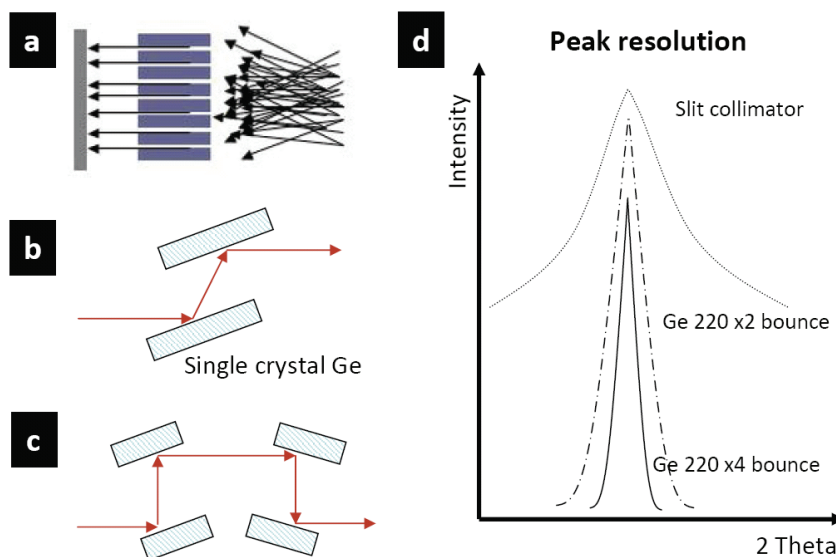


Figure 3.12 X-ray incident optics. (a) Soller slit collimator. (b) 2-bounce single crystal Ge monochromator. (c) 4-bounce monochromator. (d) Schematic for peak resolution vs. intensity for different optics.

The first incident slit (length-limiting slit) at the end of the source arm (Figure 3.7) controls the divergent angle of the beam (BB) or the length of the beam (PB) illuminating on the sample (Figure 3.13). The height of the beam illuminating on the sample is varied by the incident angle (w). If the incident angle is small, large area is illuminated (with smaller penetration depth) whereas for a large incident angle, the illumination area becomes small (with larger penetration depth). The sample is mounted on a goniometer with x-, y-shift, cradle (rocking), and rotation (in-plane)

capability.

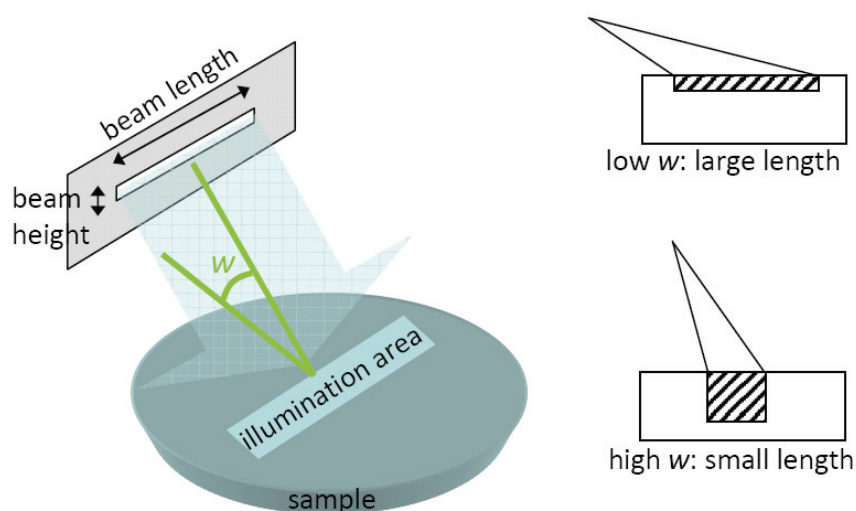


Figure 3.13 Length limiting slit and the sample illumination area.

The receiving slit and the optics on the detector arm (Figure 3.7) are installed to reduce the fluorescent photons, generated from the sample, reaching the detector. Monochromator can also be mounted for high resolution scans. For small-angle X-ray scattering measurements, a vacuum tube optic is installed to minimize the scattering due to air and maximize the X-ray signal collection.

An attenuator is installed right before the detector to automatically adjust the X-ray beam intensity. A solid-state silicon detector is mounted at the end of the detector arm when incident X-ray creates electron-hole pairs. These charges are collected, amplified, and recorded with excellent energy resolution. The X-ray photon

arriving at the detector is counted with a limited period of time. By increasing the data collection time (n times), the signal to noise ratio can be improved by $n^{1/2}$.^[43] In order to increase the data collection rate, position sensitive strip detector can also be mounted.

Five measurement techniques are performed to characterize nanocrystals and their assemblies: powder X-ray diffraction (pXRD), in-plane XRD, transmission small angle X-ray scattering (TSAXS), reflection-mode SAXS, and in-plane SAXS. The pXRD is the most widely used technique for crystal phase determination. Figure 3.14 shows the pXRD pattern obtained from PbTe nanocrystals and nanocubes which is identical to the bulk crystal phase (Altaite, JCPDS 021-0885). Size broadening is estimated using the Scherrer's equation: $B = s\lambda/t\cos\theta$ where B is the full width-half maximum of the diffraction peak, s is the shape factor, λ is the X-ray wavelength (1.54 Å), t is the thickness of the nanocrystallite, and θ is the Bragg's angle. Using (200) Bragg's reflection, the nanocrystallite size was calculated to be 5.5 nm for the spherical nanocrystal ($s = 0.89$) and 18.5 for the cubic particle ($s = 0.94$) which is consistent with the TEM observation.

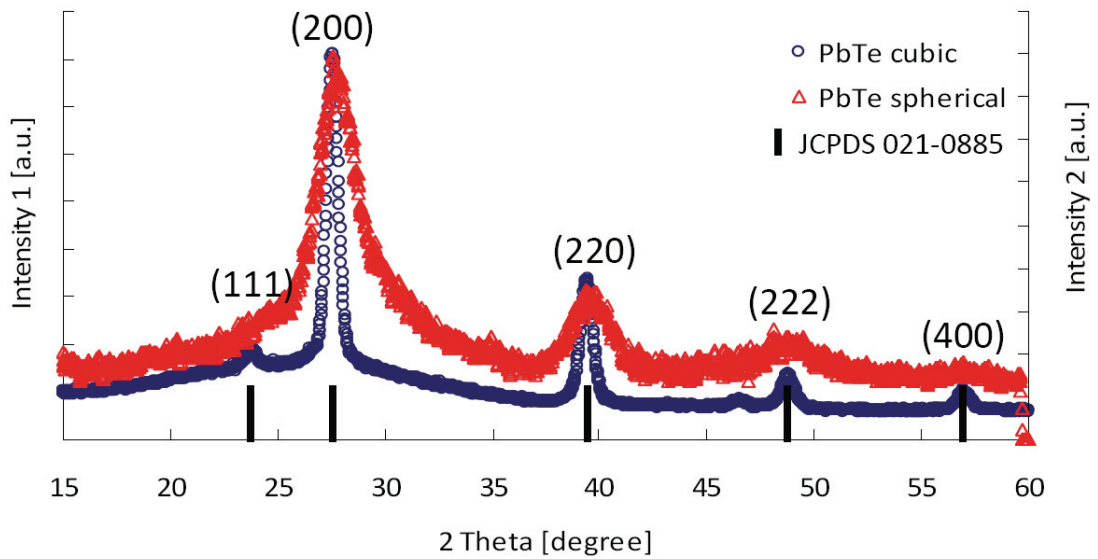


Figure 3.14 Powder diffraction data obtained from 5.5 nm spherical nanocrystals and 18.5 nm nanocubes.

The standard pXRD offers crystal structure information obtained by diffraction from surface-normal lattice plane. The penetration depth (x) of X-ray into the sample depends on the incident angle w and the X-ray absorption coefficient μ as $x = [-\ln(1-G)]/\sin w/2 \mu$ where G is the ratio between incident and diffracted beam intensity.^[44] When the sample thickness is too thin or to structurally probe only the sample surface, in-plane diffraction is employed. Since the beam is incident at a grazing angle, only the surface (~ 100 nm) structure is probed. The source and the detector perform a 2theta-theta scan in a circle that is almost parallel to the surface which provides surface-parallel structural information. Figure 3.15 shows an example of spatially-resolved in-plane XRD of CdS thinfilm deposited on a tin oxide substrate. Conventional pXRD could not resolve diffraction peak arising from CdS (Greenockite

70-02553 and Hawleyite 75-0581).

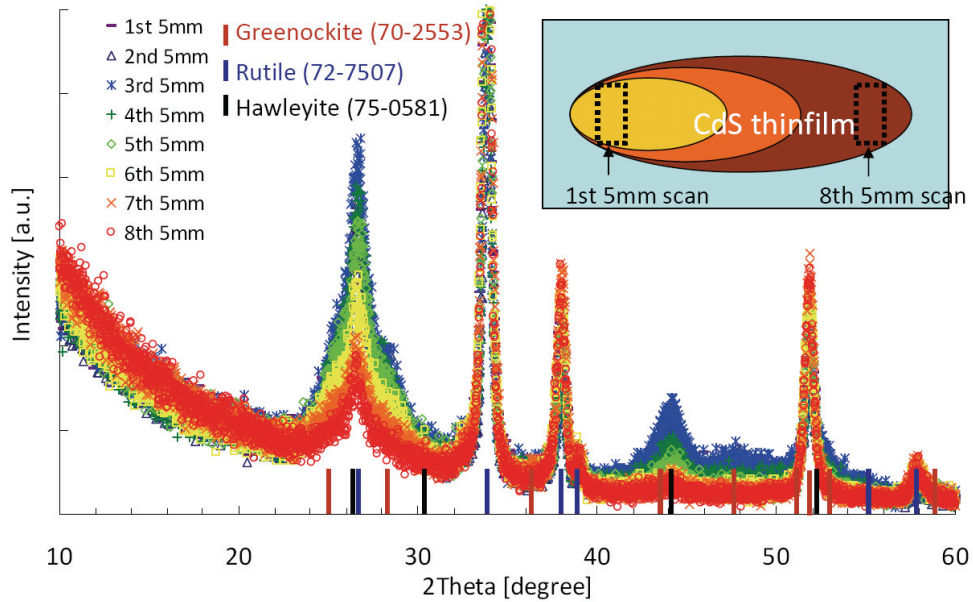


Figure 3.15 Spatially resolved in-plane XRD of CdS thinfilm deposited on a tin oxide substrate.

Strong Bragg diffractions provide a precise determination of the atomic structure of the crystal. On the other hand, diffuse scattering also reveal valuable structural information on a scale larger than the atomic spacing. In SAXS, scattering arises from the electron density difference between the nanoscale object and the surrounding medium. The intensity of the scattering radiation is expressed as, $I(q) = |f(q)|^2 \cdot S(q)$ where $f(q)$ is the form factor which depends on the size and shape of the particle and $S(q)$ is the structure factor which gives the correlation between particles. Formulation of $f(q)$ using standard spherical model with Schultz distribution function accounting for the size dispersion^[46-48] and equating $S(q) = 1$ for dilute assumption,

scattering profile can be fitted to obtain average size and distribution of nanocrystals.

Figure 3.16 shows TSAXS profiles and simulation fittings (black curve) obtained from as-synthesized PbS nanocrystals dispersed in hexane. Three rounds of ultra-centrifugation were performed (Thermo Scientific Sorvall WX Ultra Centrifuge) to further reduce the size dispersion.

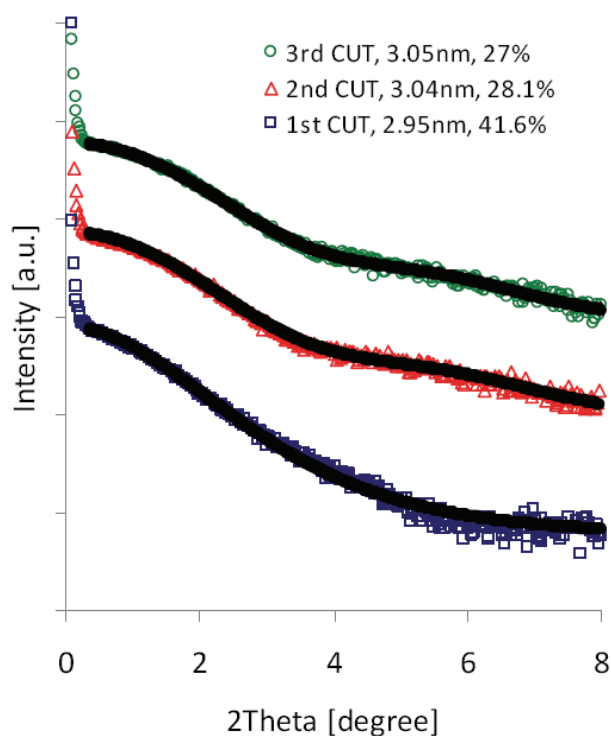


Figure 3.16 Transmission SAXS curve obtained from PbS nanocrystal with three different average size and distribution. Black curves represent simulating fittings.

Nanocrystals assembled into a superlattice is investigated using reflection small-angle X-ray scattering (RSAXS) and in-plane small-angle X-ray scattering (in-plane SAXS) measurements. GdF₃ nanoplates are chosen as the nanocrystal building

blocks due to high monodispersity and tunability in shape and size. Upon assembly liquid-crystalline-like superlattices are formed. In the RSAXS measurement, X-ray beam scatters off the nanocrystal film on substrate as illustrated in Figure 3.17 (a) and scattered beam is collected in 2θ - θ geometry. An off-set scan ($\theta + \delta\theta/2\theta$) is performed to avoid strong specular reflection. Bragg diffraction patterns obtained from RSAXS measurements indicate out-of-plane ordering. On the other hand, in-plane SAXS measurements utilize a grazing incident geometry (α_i) and scattered beam is collected by scanning detector in a plane parallel to the film surface (Figure 3.17 (b)). In-plane SAXS provides scattering information about in-plane ordering. Therefore, the two scattering measurements are complimentary and provide precise structural information to confirm the orientation of the liquid crystalline assemblies. In both RSAXS and in-plane measurements, up to 9th order of Bragg diffractions are observed with equal spacing that is the result of scattering from the face-to-face ordering of the nanoplates (Figure 3.17 (c) and (d)). High order diffractions indicate that long-range translational order exists within the nanoplate stacks. Peak broadening in SAXS patterns is an indication of the average domain size of assembled structure.

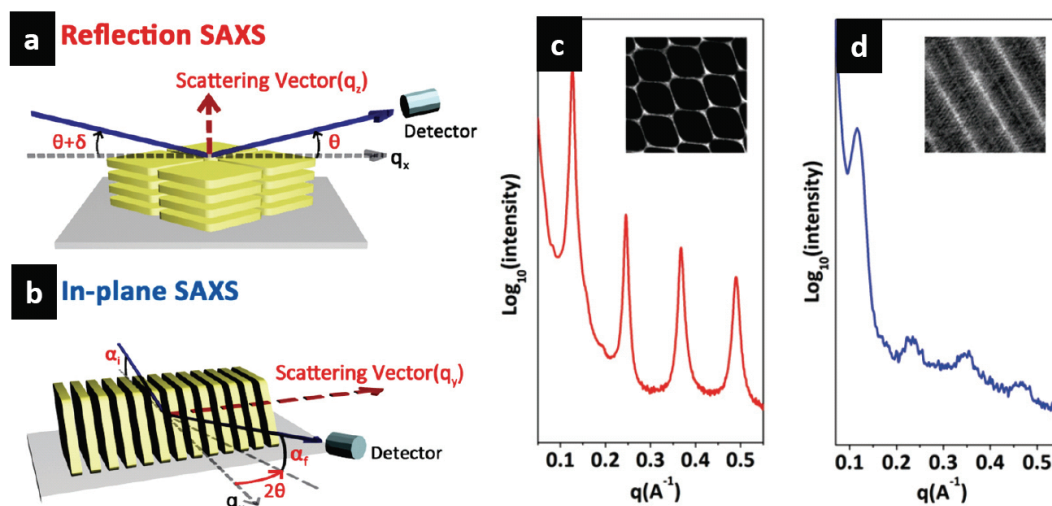


Figure 3.17 Schematics of a small-angle X-ray scattering experiment. (a) RSAXS), (b) In-plane SAXS, and (c) RSAXS patterns showing fringe patterns corresponding to columnar assembly, (d) In-plane SAXS result indicating to lamellar assembly.

The scattering angles of the peaks in the SAXS pattern are used to determine the average inter-particle spacing, where the center-to-center distance between nearest neighbors in the nanoplate stacks is given by $d=2\pi/q$. In RSAXS, the position of first diffraction peak is $0.127(\text{Å}^{-1})$ which corresponds to a 4.9 nm of center-to-center distance. Average inter-particle spacing is obtained by subtracting the nanoplate thickness from center-to-center distance. The thickness of rhombic nanoplate observed by TEM is 2.4 nm. Thus, the average inter-particle spacing in columnar assembled nanoplates is estimated as 2.5 nm which is consistent with the average length of two oleic acid molecules. On the other hand, the position of first diffraction peak from in-plane SAXS is $0.115(\text{Å}^{-1})$ and the lattice spacing in lamellar ordering

gives 5.5 nm.

3.5 Conclusion

Monodisperse PbTe NCs with size varying from 4 to 11.5 nm were synthesized via hot-injection method. The size tunability, monodispersity, high dielectric constant, as well as low effective mass and large Bohr radius offered by PbTe provide an ideal building block to design and engineer artificial solids for carrier transport and energy conversion studies.

Monodisperse Ag₂Te NCs synthesized with the average size of 3.1 nm show distinct absorption peaks similar to the interband absorption observed in quantum confined semiconductor nanocrystals. In order to identify the nature of this optical feature, temperature-dependent optical gap as well as absorption shift as a function of solvent dielectric constant was investigated which revealed the semiconducting property of the Ag₂Te NCs. The sharp absorption at 1154 nm uniquely located inside the window of the biological tissue accompanied by the linear and large temperature bandgap coefficient offers the potentials for temperature markers in living cells. The functionality offered from nanocrystals in addition to unusual physical properties of Ag₂Te provides a valuable materials system to further explore.

Lastly, directed self-assembly of colloidal nanocrystals into ordered superlattices enables the preparation of novel artificial solids with diverse functionalities. To understand the origin of the collective interactions between nanocrystals assembled into superlattices, the structure must be precisely characterized. Structural parameters, such as the symmetry, domain orientation, inter-particle spacing, and degree of order all influence the mutual interactions between nanocrystal building blocks. This understanding allows us to design the properties of new solids from a set of building blocks, which is distinct from those of individual nanoparticles.

Reference

1. Talapin, D. V.; Murray, C. B. PbSe Nanocrystal Solids for n- and p-Channel Thin Film Field-Effect Transistors. *Science*, **2005**, *310*, 86–89.
2. Kang, M. S.; Lee, J.; Norris, D. J.; Frisbie, C. D. Size-Dependent Electrical Transport in CdSe Nanocrystal Thin Films. *Nano Lett.*, **2009**, *9*, 3848–3852.
3. McDonald, S. A. *et al.* Solution-Processed PbS Quantum Dot Infrared Photodetectors and Photovoltaics. *Nature Mater.*, **2005**, *4*, 138–142.
4. Ellingson, R. J. *et al.* Highly Efficient Multiple Exciton Generation in Colloidal PbSe and PbS Quantum Dots. *Nano Lett.*, **2005**, *5*, 865–871.
5. Wise, F. W. Lead Sulfide Quantum Dots: the Limit of Strong Quantum Confinement. *Acc. Chem. Res.*, **2000**, *33*, 773–780.
6. Madelung, O.; Roessler, U.; Schulz, M. Landolt-Bornstein - Group III Condensed Matter; *Springer-Verlag*, Berlin, **1998**.
7. Dughaish, Z. H. Lead Telluride as a Thermoelectric Material for Thermoelectric Power

- Generation. *Physica B*, **2002**, 322, 205–223.
8. Ji, X.; Zhang, b.; Su, Z.; Holgate, T.; He, J.; Tritt, T. M. Nanoscale Granular Boundaries in Polycrystalline $\text{Pb}_{0.75}\text{Sn}_{0.25}\text{Te}$: An Innovative Approach to Enhance the Thermoelectric Figure of Merit. *Phys. Status Solidi A*, **2009**, 206, 221–228.
9. Caylor, J. C.; Coonley, K.; Stuart, J.; Colpitts, T.; Venkatasubramanian, R. Enhanced Thermoelectric Performance in PbTe-Based Superlattice Structures from Reduction of Lattice Thermal Conductivity. *Appl. Phys. Lett.*, **2005**, 87, No. 023105.
10. Harman, T. C.; Taylor, P. J.; Walsh, M. P.; LaForge, B. E. Quantum Dot Superlattice Thermoelectric Materials and Devices. *Science*, **2002**, 297, 2229–2232.
11. Vineis, C. J.; Harman, T. C.; Calawa, S. D.; Walsh, M. P.; Reeder, R. E.; Singh, R.; Shakouri, A. Carrier Concentration and Temperature Dependence of the Electronic Transport Properties of Epitaxial PbTe and PbTe/PbSe Nanodot Superlattices. *Phys. Rev. B*, **2008**, 77, 235202.
12. Rowe, D. M. *CRC Handbook of thermoelectrics*; CRC Press: New York, 1995.13.
- Schneider, J.; Schulz, H. Z. X-ray Powder Diffraction of Silver Telluride (Ag_2Te) at Temperatures Up to 1123 K. *Kristallogr.*, **1993**, 203, 1-15.
14. Karakaya, I.; Thompson, W. T. The Ag-Te (Silver-Tellurium) System. *J. Phase Equilib.*, **1991**, 12, 56-63.
15. Kobayashi, M.; Ishikawa, K.; Tachibana, F.; Okazaki, H. Diffusion Path and Haven's Ratio of Mobile Ions in $\alpha\text{-Ag}_2\text{Te}$. *Phys. Rev. B*, **1988**, 38, 3050-3055.
16. Fujikane, M.; Kurosaki, K.; Muta, H.; Yamanaka, S. Electrical Properties of α - and β - Ag_2Te . *J. Alloy. Compd.*, **2005**, 387, 297-299.
17. Xu, R. *et al.*, Large Magnetoresistance in Non-Magnetic Silver Chalcogenides. *Nature*, **1997**, 390, 57-60.
18. Lee, M.; Rosenbaum, T. F.; Saboungi, M.-L.; Schnyders, H. S. Band-Gap Tuning and Linear Magnetoresistance in the Silver Chalcogenides. *Phys. Rev. Lett.*, **2002**, 88, 066602.
19. Taylor, P. F.; Wood, C. J. Thermoelectric Properties of Ag_2Te . *Appl. Phys.*, **1961**, 32, 1-3.
20. Chen, R.; Xu, D.; Guo, G.; Gui, L. Silver Telluride Nanowires Prepared by DC Electrodeposition in Porous Anodic Alumina Templates. *J. Mater. Chem.*, **2002**, 12, 2435-2438.
21. Qin, A.; Fang, Y.; Tao, P.; Zhang, J.; Su, C. Silver Telluride Nanotubes Prepared by the Hydrothermal Method. *Inorg. Chem.*, **2007**, 46, 7403-7409.
22. Zuo, P.; Zhang, S.; Jin, B.; Tian, Y.; Yang, J. Rapid Synthesis and Electrochemical Property of Ag_2Te Nanorods. *J. Phys. Chem. C.*, **2008**, 112, 14825-14829.
23. Sahu, A.; Qi, L.; Kang, M. S.; Deng, D.; Norris, D. J. Facile Synthesis of Silver Chalcogenide (Ag_2E ; E = Se, S, Te) Semiconductor Nanocrystals. *J. Am. Chem. Soc.*, **2011**, 133, 6509-6512.
24. Harpeness, R.; Palchik, O.; Gedanken, A.; Palchik, V.; Amiel, S.; Slifkin, M. A.; Weiss,

- A. M. Preparation and Characterization of Ag₂E (E = Se, Te) Using the Sonochemically Assisted Polyol Method. *Chem. Mater.*, **2002**, *14*, 2094-2102.
25. Murray, C. B.; Norris, D. J.; Bawendi, M. G. Synthesis and Characterization of Nearly Monodisperse CdE (E = S, Se, Te) Semiconductor Nanocrystallites. *J. Am. Chem. Soc.*, **1993**, *115*, 8706-8715.
26. Peng, X.; Wickham, J.; Alivisatos, A. P. Kinetics of II-VI and II-V Colloidal Semiconductor Nanocrystal Growth: "Focusing" of Size Distributions. *J. Am. Chem. Soc.*, **1998**, *120*, 5343-5344.
27. Porter, D. A.; Easterling, K. E. Phase Transformations in Metals and Alloys. *Chapman & Hall*, New York, **1992**.
28. Peng, Z. A.; Peng, X. Nearly Monodisperse and Shape-Controlled CdSe Nanocrystals via Alternative Routes: Nucleation and Growth. *J. Am. Chem. Soc.*, **2001**, *124*, 3343-3353.
29. Urban, J. J., Talapin, D. V., Shevchenko, E. V. & Murray, C. B. Self assembly of PbTe quantum dots into nanocrystal superlattices and glassy films. *J. Am. Chem. Soc.*, **2006**, *128*, 3248-3255
30. Murphy, J. E. *et al.* PbTe colloidal nanocrystals: synthesis, Characterization, and multiple exciton generation. *J. Am. Chem. Soc.*, **2006**, *128*, 3241-3247
31. Mokari, T., Zhang, M. & Yang, P. Shape, size, and assembly control of PbTe nanocrystals. *J. Am. Chem. Soc.*, **2007**, *129*, 9864-9865
32. Lu, W., Fang, J., Stokes, K. L. & Lin, J. Shape evolution and self assembly of monodisperse PbTe nanocrystals. *J. Am. Chem. Soc.*, **2004**, *126*, 11798-11799
33. Bishop, A. C.; Woolley, A. R.; Hamilton, W. R. *Cambridge Guide to Minerals, Rocks and Fossils*, Cambridge University Press, Cambridge, **1999**.
34. Wenk, H.-R.; Bulakh, A. *Minerals: their constitution and origin*; Cambridge University Press, Cambridge, **2004**.
35. Stoeva, S.; Klabunde, K. J.; Sorensen, C. M.; Dragieva, I. Gram-Scale Synthesis of Monodisperse Gold Colloids by the Solvated Metal Atom Dispersion Method and Digestive Ripening and Their Organization into Two- and Three-Dimensional Structures. *J. Am. Chem. Soc.*, **2002**, *124*, 2305-2311.
36. Dai, Q. *et al.* Facile Synthesis of Magic-Sized CdSe and CdTe Nanocrystals with Tunable Existence Periods., *Nanotechnology*, **2007**, *18*, 405603.
37. Dai, Q. *et al.* Size-Dependent Composition and Molar Extinction Coefficient of PbSe Semiconductor Nanocrystals. *ACS Nano*, **2009**, *3*, 1518-1524.
38. Moreels, I. *et al.* Composition and Size-Dependent Extinction Coefficient of Colloidal PbSe Quantum Dots. *Chem. Mater.* **2007**, *19*, 6101-6106.
39. Jesser, W. A.; Shiflet, G. J.; Allen, G. L.; Crawford, J. L. Equilibrium Phase Diagrams of Isolated Nano-Phases. *Mat. Res. Innovat.*, **1999**, *2*, 211-216.

40. Sutter, E.; Sutter, P. Phase Diagram of Nanoscale Alloy Particles Used for Vapor-Liquid-Solid Growth of Semiconductor Nanowires. *Nano Lett.* **2008**, *8*, 411-414.
41. Jesser, W. A.; Shneck, R. Z.; Gile, W. W. Solid-Liquid Equilibria in Nanoparticles of Pb-Bi Alloys. *Phys. Rev. B*, **2004**, *69*, 144121.
42. Luther, J. M.; Jain, P. K.; Ewers, T.; Alivisatos, A. P. Localized Surface Plasmon Resonances Arising from Free Carriers in Doped Quantum Dots. *Nature Mater.* **2011**, *10*, 361-366.
43. Haberkorn R. Introduction to Powder X-Ray Diffraction: *Bruker AXS*, **1999**.
44. Cullity B. D.; Stock S. R. Elements of X-ray Diffraction, *Prentice Hall*, **2001**.
45. Schuster, M; Gobel, H. Parallel-Beam Coupling into Channel-Cut Monochromators Using Curved Graded Multilayers. *J. Phys. D: Appl. Phys.* **1995**, *28*, A270-A275.
46. Brochert, H. *et al.* Determination of Nanocrystal Sizes: A Comparison of TEM, SAXS, and XRD Studies of Highly Monodisperse CoPt₃ Particles. *Langmuir* **2005**, *21*, 1931–1936.
47. Reiker, T.; Hanprasopwattana, A.; Datye, A.; Hubbard, P. Particle Size Distribution Inferred from Small-Angle X-ray Scattering and Transmission Electron Microscopy. *Langmuir* **1999**, *15*, 638–641.
48. Kotlarchyk, M.; Chen, S.-H. Analysis of Small Angle Neutron Scattering Spectra from Polydisperse Interacting Colloids. *J. Chem. Phys.* **1983**, *79*, 2461–2469.

4. Temperature-dependent thermopower in PbTe nanocrystal solids

4.1 Introduction

The core of semiconductor technology is the ability to manipulate the electronic properties of materials by introducing an electric field, light, impurities, or by changing the temperature. Solids artificially constructed from semiconductor nanocrystals provide additional size-dependent functionalities and have generated enormous interest in device applications such as photodetectors,^[1] transistors,^[2] thermoelectrics,^[3] and solar cells.^[4,5] In this class of materials, as well as in bulk semiconductors, the position of the Fermi energy level (E_F) relative to the transport energy level (E_T) is a key parameter in determining the electronic properties of the system. Currently, research is progressing to incorporate nanocrystal solids into more complex architectures, including metal/semiconductor junctions,^[6,7] semiconductor heterojunctions,^[8] and organic/inorganic hybrid structures.^[9,10] However, there are a limited number of studies devoted to measuring and interpreting E_F in semiconductor nanocrystal solids,^[11] which is crucial in optimizing device performance. In this work, we directly extract $E_F - E_T$ by applying temperature-

dependent thermopower measurements to semiconductor nanocrystal solids. This measurement technique is particularly useful for nanocrystal solid systems in which electron or hole conduction occurs via hopping between localized energy states^[12,13] above or below E_F , respectively. Electrical conductivity measurements cannot distinguish $E_F - E_T$ and the activation energy for mobility separately in these systems. Furthermore, thermopower measurements are conducted under open-circuit conditions, and it is insensitive to the contact resistance, which gives us an additional advantage over electrical conductivity measurements. Using temperature- dependent thermopower measurements, we extract each term of the thermopower equation^[14] and examine their physical meaning as applied to semiconductor nanocrystal solids.

4.2 Experimental details

In a typical synthesis, 1.138 g of lead acetate trihydrate (Aldrich, 99%) and 2 mL of oleic acid (Aldrich, 90%) were added to 20 mL of squalane (Aldrich, 99%), which was heated at 100 °C for 2 h under vacuum. After the solution was heated to 185 °C under nitrogen flow, 4 mL of trioctylphosphine telluride (0.75M, TOP-Te) solution, which was prepared by dissolving 4.75 g of tellurium shot in 50 mL of trioctylphosphine (Aldrich, 90%), was injected and the growth temperature was

maintained at 175 °C. The growth time was varied from 20 s to 2 min 30 s which yielded nanocrystal sizes varying from 6.4 nm to 9.97 nm. For the largest 11.5 nm nanocrystals, 6 mL of TOP-Te was injected at 195 °C and the growth was maintained at 180 °C for 2 min and 30 s. Polydisperse nanocrystals were synthesized by injecting 4 mL of TOP-Te slowly in a drop-wise manner at 185 °C where the growth temperature dropped down to 173 °C gradually during 1 min and 15 s of reaction. All syntheses were performed using the standard air-free technique (Schlenk line), and separation and purification processes were done in a nitrogen glovebox using anhydrous hexane and acetone. Optical absorption measurements on PbTe nanocrystals dissolved in tetrachloroethylene (Aldrich, 99%) were performed using Analytical Spectral Devices QSP 350-2000 with airtight cuvettes. TEM images were obtained using JEOL 1400. For SAXS experiments, samples were prepared in sealed capillaries filled with PbTe nanocrystals dissolved in hexane, and the measurements were conducted using Rigaku Smartlab high-resolution diffractometer.

Samples for thermopower measurements were prepared inside the nitrogen glovebox without exposure to oxygen and moisture. PbTe nanocrystals, dissolved in an anhydrous hexane and octane mixture, were dropcast on to a thin microscope cover glass to form a glassy film. This cover glass was scribed beforehand with precision diamond scribe so that small rectangular shapes can be easily cleaved later on with a

small amount of pressure. The PbTe nanocrystal film was then submerged in 1 M of hydrazine (Aldrich, anhydrous, 98%) in acetonitrile (Aldrich, anhydrous, 99.8%) overnight. Several depositions and treatments were repeated to fill in the cracks formed in the film, and a small rectangle portion was removed from the cover glass. All samples were prepared with approximately 1.5 mm by 4 mm geometry and an average 85 ± 20 nm nanocrystal film thickness (SEM cross-section, FEI Strata DB235) and were mounted on the measurement stage using silver paste (Leitsilber 200, Ted Pella). Temperature-dependent thermopower measurements were conducted using MMR technologies K-20 and SB-100 with a high impedance amplifier (100 gain). Copper-constantan (alloy of 45% nickel and 55% copper) is used as a reference junction to monitor temperature difference ΔT . Throughout the measurement, heater power output was adjusted so that ΔT was fixed at 1.5 K, the initial delay was set to 5 min for the temperature of the sample to reach equilibrium with the cooling stage, and the operation delay was adjusted to 30 s in order to achieve steady state across the measurement stage. All samples were kept at 6 mTorr for 3 hr prior to the measurements.

4.3 Fermi energy level in PbTe nanocrystal solids

The thermopower (R , Seebeck coefficient) is the heat carried per charge carrier divided by the temperature ($\mu\text{V/K}$), or in thermodynamic terms, the entropy transported per carrier. A general expression for the thermopower of semiconductors (p-type) was derived by Fritzsche:^[14]

$$S = \frac{k}{e} \left[\frac{(E_F - E_T)}{k_B T} + A \right] \dots\dots\dots (28)$$

where, k is the Boltzmann constant, e is the elementary charge, and A is a temperature independent constant (heat of transport constant). Here we define the transport energy level E_T associated with the onset of mobility. Unlike bulk semiconductors, E_T in a nanocrystal solid is not necessarily the edge of the density of states (DOS). When a charge carrier is thermally excited to the very edge of the DOS, there is a low probability of finding a nearby energy state with the energy difference smaller than kT and thus the carriers remain immobile. As the carriers are excited to E_T , a continuous percolation path between two electrical contacts forms and the carrier starts to hop with a detectible mobility. Beyond E_T , the mobility increases abruptly with increasing available energy states for transport. As illustrated in Figure 4.1, the position of E_T may lie between the edge and the peak of the DOS depending on the monodispersity of nanocrystals, which determines the distribution of energy states. The first term in

the bracket is known as the configurational entropy contribution to the thermopower^[15-18] which is independent of the transport mechanism. The second term A , known as the heat of transport constant, accounts for the carriers beyond E_T . It represents the additional kinetic energy of the carriers, in units of kT , weighted by their relative contribution to the total conductivity:

$$A = \frac{\int_{-\infty}^0 \frac{\varepsilon}{kT} \sigma(\varepsilon) d\varepsilon}{\int_{-\infty}^0 \sigma(\varepsilon) d\varepsilon}, \quad \varepsilon = E_T - E \dots\dots\dots(29)$$

The heat of transport constant A depends on the energy-dependent conductivity $\sigma(E)$, which is a sensitive function of energy-dependent density of states $D(E)$ and mobility $\mu(E)$. In bulk semiconductors, the heat of transport constant is a small value between 1 and 2. In semiconductor nanocrystal solid systems, constant A can have a larger value ($A > 2$) if a wider distribution of energy states are utilized for transport. It is governed by the steepness of the rise of $D(E)$ from E_T to the peak of the DOS, given that the width of the DOS distribution exceeds kT .^[19,20] Both the position of $E_F - E_T$ and the heat of transport constant A are extracted from the temperature-dependent thermopower measurements. The slope of thermopower versus $1/T$ gives $E_F - E_T$ and the constant A is derived from the y-intercept. The temperature-dependent thermopower measurement were performed using experimental configuration

previously discussed in Chapter 2.4 and Figure 2.1(d) and (e).^[21]

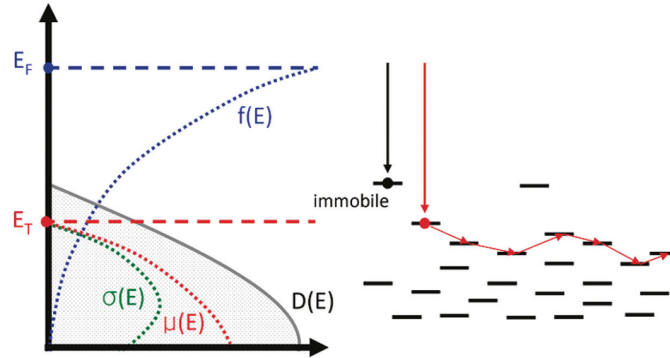


Figure 4.1 Schematic illustration of energy-dependent mobility ($\mu(E)$), density of state ($D(E)$), and Fermi-Dirac distribution function ($f(E)$) showing energy-dependent conductivity ($\sigma(E)$) in p-type semiconductor nanocrystal solids. Transport energy level E_T is defined as an energy level where the hopping mobility increases from zero. In a physical picture, it is the lowest energy level where the percolation path of energy state emerges between two contacts.

A typical plot of V_{oc} versus ΔT (while the stage temperature is fixed) for a PbTe nanocrystal (8.71 nm) solid is shown in Figure 4.2(a). The open circuit voltage V_{oc} is zero at the origin and the constant slope indicates that the thermopower of 856.37 $\mu\text{V/K}$ is an inherent property of the solid. A typical temperature-dependent thermopower measurement, R_{sam} versus stage temperature T (while ΔT is fixed), is shown in Figure 4.2(b). Reliable thermopower measurements were obtained from 300 to 190 K. Below 190 K the thermopower reading starts to fluctuate, in some cases to negative values. Interestingly, such behavior was similarly observed in liquid mercury near the critical point,^[22,23] although the reason is not clearly known. At lower

temperatures, the voltage measurement reaches maximum overload due to the high resistance of the sample.

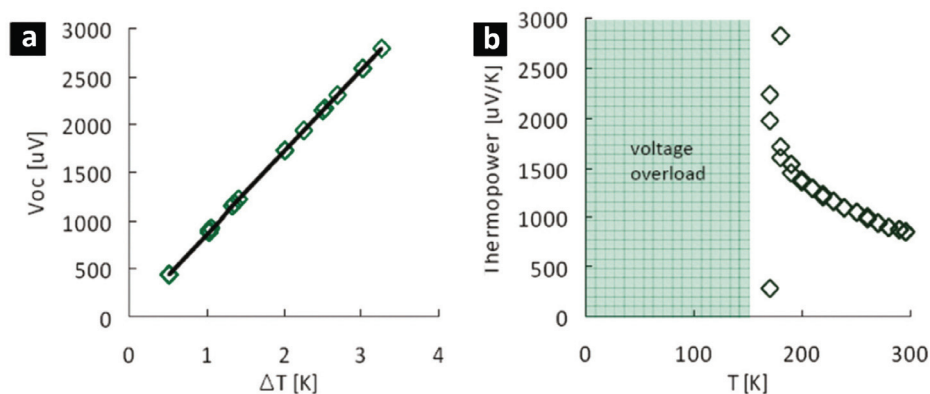


Figure 4.2 (a) Measurements of open-circuit voltages on a PbTe nanocrystal (8.71 nm) solid as a function of applied temperature difference ΔT while the temperature of the cooling stage was fixed at room temperature. The slope gives the thermopower of 856.37 $\mu\text{V}/\text{K}$. (b) Plot of temperature-dependent thermopower measurement on the same sample while ΔT was fixed at 1.5 K. Around ~ 180 K the thermopower starts to fluctuate and below 170 K the measurement readings were unreliable due to voltage overload.

The consistency of thermopower measurements were confirmed by using three PbTe nanocrystal samples (color coded) with similar average size and dispersion but from different synthesis batches. Thermopower measurements on these samples yield a similar slope and y-intercept on the thermopower versus $1000/T$ plot, as shown in Figure 4.3.

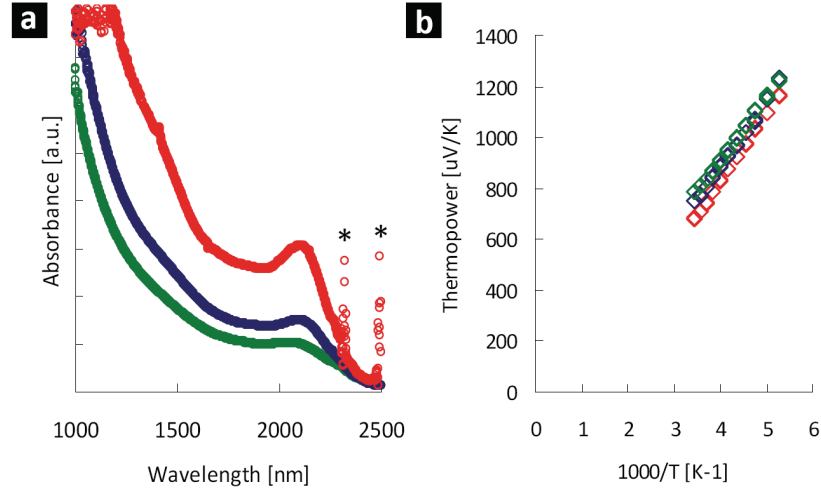


Figure 4.3 (a) Optical absorption of three PbTe nanocrystal samples from separate synthesis batches (different concentration) showing similar average size and dispersion. Two asterisks indicate superposition of solvent (squalane) and surfactant (oleic acid) vibrational overtones. (b) Raw data of temperature-dependent thermopower measured on three samples showing the consistency of measurements. Three data points were measured at each designated temperature domain and each data point represents 6 averaged readings.

Our first interest in this work is to examine $E_F - E_T$ as a function of PbTe nanocrystal size. A series of nanocrystals with different sizes varying from 6.4 to 11.5 nm were synthesized by modifying the reaction temperature, time, and Pb/Te ratio, as shown in Figure 4.4. Average nanocrystal size and distribution were characterized using small angle X-ray scattering (SAXS) and were compared with the transmission electron microscopy (TEM) data. SAXS data curves were fit using a standard spherical model with a Schultz distribution function accounting for the nanocrystal size distributions.^[24-26] Average size determined from TEM image analysis compared with SAXS data fitting show an increasing deviation as the nanocrystal size increases.

This increase in error is due to the evolution of shape from spherical to cubic as the PbTe nanocrystals grow.^[27-30] This is shown in Figure 4.4(a) for the largest PbTe nanocrystal which explains the discrepancy of average size determination using spherical SAXS fitting model. The average size and distribution expressed in standard deviation, determined by SAXS experiments were 11.5 nm \pm 8.1% (largest nanocrystals, denoted as A), 9.97 nm \pm 10.8% (B), 8.71 nm \pm 9.3% (C), 7.55 nm \pm 9.5% (D), and 6.4 nm \pm 11.4% (smallest nanocrystals, E).

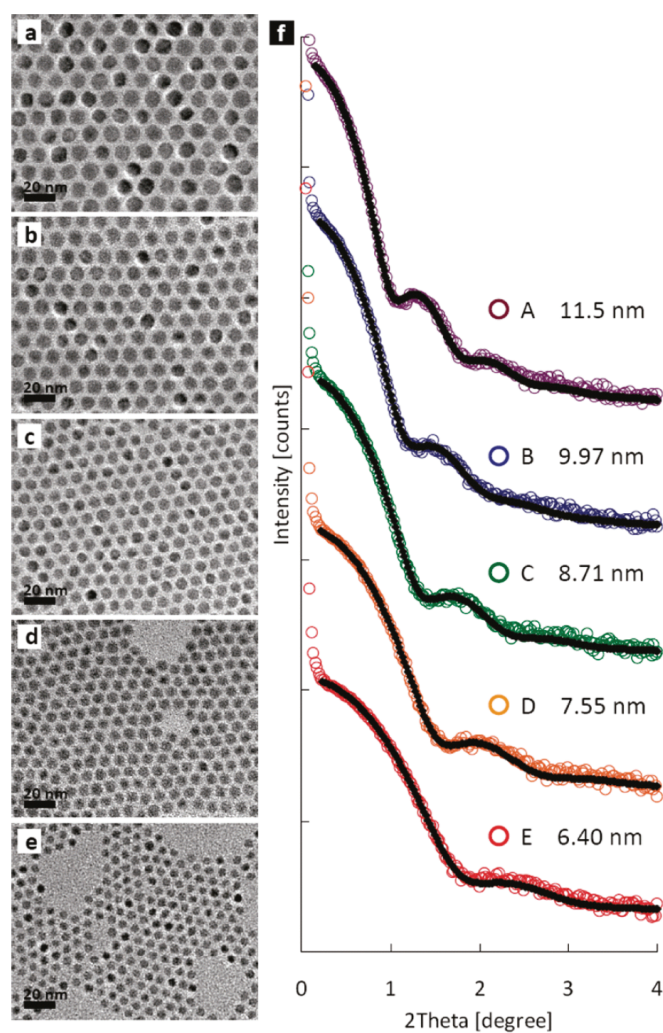


Figure 4.4 TEM image of PbTe nanocrystals synthesized with five different sizes (a-e) and corresponding SAXS curves (f). The scattering curves were fit (shown in solid line) using a spherical model with particle size distribution corresponding to the Schultz distribution function. Largest nanocrystals (a and purple scattering curve A in panel f) yields an average size of 11.5 nm with 8.1% standard deviation. Smallest nanocrystals had average size of 6.4 nm with a standard deviation of 11.4% (e and red curve E in panel f). Medium size range particles (b-d) denoted as curves B, C, and D in panel f show average sizes and distributions of 9.97 nm \pm 10.8%, 8.71 nm \pm 9.3%, and 7.55 nm \pm 9.5%, respectively.

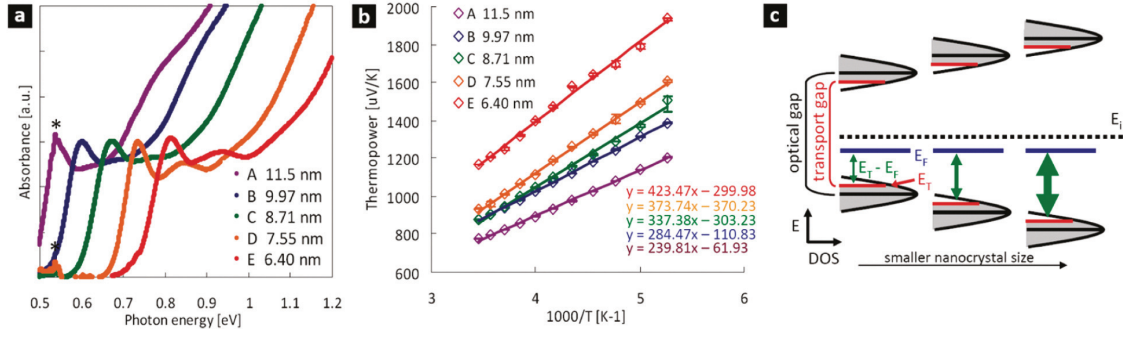


Figure 4.5 (a) Optical absorption spectra of PbTe nanocrystals of five different sizes. Two asterisks indicate superposition of solvent (squalane) and surfactant (oleic acid) vibrational overtone. (b) Temperature-dependent thermopower measurements on nanocrystal solids constructed from various sizes of PbTe nanocrystals. Each solid line is a linear fit to extract slopes which reveal $E_F - E_T$. The y-intercept comes from three different contributions which include the heat of transport constant. (c) Schematic illustration of $E_F - E_T$ as a function of nanocrystal size as measured in temperature-dependent thermopower measurements.

sample name	A	B	C	D	E
average size[nm]	11.5	9.97	8.71	7.55	6.4
std dev [%]	8.1	10.8	9.3	9.5	11.4
junction Resistance [M Ω]	2.65	4.89	14.4	39.96	> 40 (OL)
thermopower, RT [uV/K]	774.08	875.43	874.25	932.09	1167.82
slope [ueV]	239.81	284.47	337.38	373.74	423.47
std error, slope	1.36	0.95	5.75	3.25	6.16
y-intercept [ueV/K]	-61.93	-110.83	-303.23	-370.23	-299.98
std error, y-intercept	5.81	4.07	24.62	13.90	26.37

Table 4.1 Table summarizing the basic physical properties of the samples prepared for temperature-dependent thermopower experiments and the measurement analyses. Average size and dispersion in standard deviation is measured from SAXS experiments. Junction resistance was measured after the sample was mounted on the measurement stage using Fluke 117 multimeter. The smallest nanocrystal (E) sample shows resistance higher than 40 M Ω which is out of the multimeter's measurement range (overload). The slopes and the y-intercepts were extracted from thermopower versus 1000/T plot.

The optical absorption spectra of PbTe nanocrystals are shown in Figure 4.5(a). From the largest (A) to the smallest (E) nanocrystals, optical gaps defined from

the first excitonic peaks were 0.54, 0.60, 0.67, 0.74, and 0.82 eV. Corresponding temperature-dependent thermopower measurements are shown in Figure 4.5(b). Table 4.1 summarizes the physical properties of samples prepared for the thermopower and the measurement results. For all, the samples were dropcast and treated with 1 M of hydrazine in anhydrous acetonitrile overnight followed by subsequent cycles of nanocrystal depositions and hydrazine treatments to make a continuous thick film. The samples were mounted on the cooling stage in a closed chamber which was kept under vacuum (6 mTorr) for 3 hr prior to the measurements. Hydrazine treatment^[27,31,32] is known to reduce the interparticle spacing (Figure 4.6) facilitating interparticle carrier transport and to dope PbTe nanocrystal solids n-type (Figure 4.7(a) and (b)). Under vacuum conditions, hydrazine desorbs from the surface of the nanocrystals converting the solid to p-type.^[31] All samples, sizes ranging from A to E, show positive thermopower indicating that the majority carriers responsible for electronic conduction are holes. This is consistent with the result that only holes can be accumulated in the field-effect transistor measurements (Figure 4.7(c) and (d)), suggesting that PbTe nanocrystal solids can be described as unipolar p-type semiconductors. The slopes of each sample from the linear fit give 239.81 ± 1.36 meV (A), 284.47 ± 0.95 meV (B), 337.38 ± 5.75 meV (C), 373.74 ± 3.25 meV (D), and 423.7 ± 6.16 meV (E) from the largest to the smallest samples, respectively.

Comparison of the optical gap and the temperature dependent thermopower measured on nanocrystal sample A indicates that $E_F - E_T$ is smaller than half of the measured optical gap. This indicates that E_F lies below the midgap (p-type). As the size of the constituent nanocrystals is reduced, the separation between the lowest occupied and the highest unoccupied energy states increases due to quantum confinement. This results in the DOS gap widening in the solid as illustrated in Figure 4.5(c) and reflected in the increasing slope ($E_F - E_T$) in Figure 4.5(b).

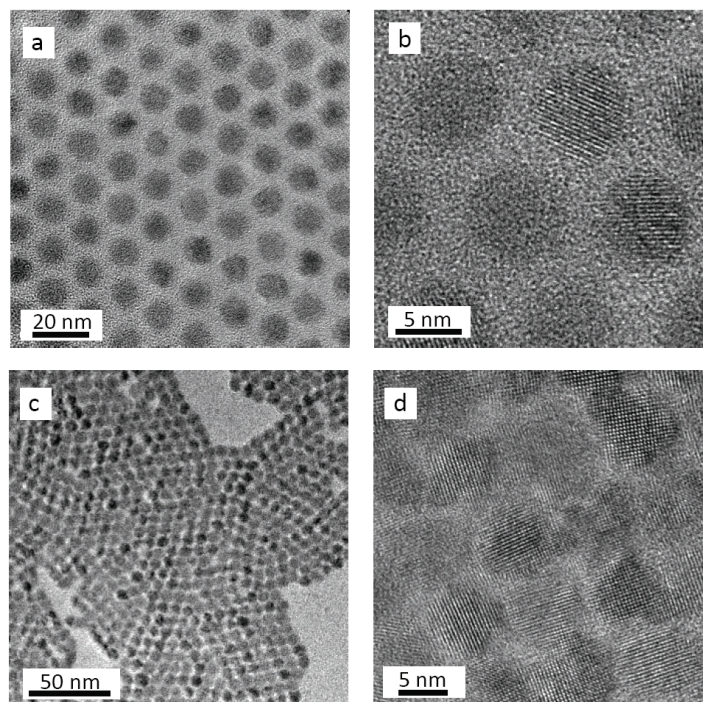


Figure 4.6 TEM images of 7.5 nm PbTe nanocrystal assemblies before and after hydrazine treatment. (a,b) Low magnification and high-resolution TEM images of PbTe nanocrystal assemblies before the hydrazine treatment. Average interparticle spacing is 2.8 nm. (c,d) PbTe assemblies after the hydrazine treatment. Average interparticle spacing is reduced to 0.3 nm.

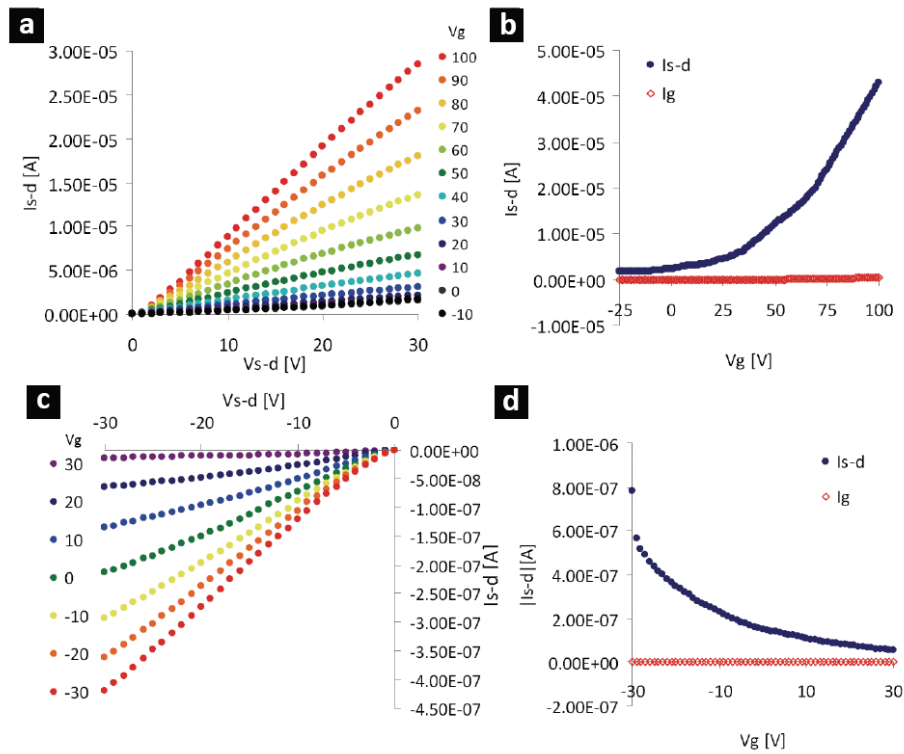


Figure 4.7 (a) Field-effect transistor (FET) measurements for a hydrazine treated PbTe nanocrystal solid. PbTe nanocrystals with first excitonic peak at 1880 nm were synthesized and dropcast on heavily p-doped Si/SiO_x (200 nm thermal oxide) substrate with predefined 40 nm Au/Ti electrodes (channel aspect ratio, 1:300). Nanocrystal films were treated with 4 M of hydrazine in acetonitrile overnight and multiple cycles of deposition and treatment were followed. The source-drain current (I_{s-d}) versus source-drain voltage (V_{s-d}) characteristic and the transfer characteristic (I_{s-d} vs. gate voltage V_g) show *n*-type accumulation behavior. The field-effect mobility at saturation regime was $1.6 \times 10^{-3} \text{ cm}^2/\text{Vs}$. Electronic measurements were conducted using MMR microprobe station coupled with HP 4145B semiconductor parameter analyzer. Gate currents (I_g) are plotted to demonstrate that there are negligible leakage current through the oxide. (b) FET measurements under vacuum condition on hydrazine treated PbTe nanocrystal solid. Same device mention in (a) and (b) was kept under vacuum (6 mTorr) for 3 hours. As the hydrazine desorbs away from the surface, the nanocrystal solid changes to a *p*-type semiconductor as observed by the FET measurements.

It is worth noting that the smallest nanocrystal samples exhibit the highest electrical resistivity (see details in the Table 4.1), which results in reduced accuracy of

the thermopower measurement. This is observed in sample E of Figure 4.5(b) as the measured data fluctuate around the linear regression. While these temperature-dependent thermopower measurements cannot directly reveal the exact position of E_F and E_T , their difference ($E_F - E_T$) can be a valuable piece of information when combined with other material characterization techniques. First, if the effective density of states $D(E)$ is known, the carrier concentration can be calculated from the well-known Maxwell-Boltzmann statistics ($p = D(E) \cdot \exp[(E_F - E_T)/kT]$). Second, the exact position of the Fermi energy level can be determined with either electron affinity or ionization potential information (with respect to the zero vacuum level), which can be measured by cyclic voltammetry^[33] or ultraviolet photoemission spectroscopy (UPS).^[34] The full DOS diagram for semiconductor nanocrystal solids can be constructed to estimate the electrostatic potential (corresponding to band-bending in bulk semiconductors) created at the semiconductor/semiconductor or metal/semiconductor junctions. Finally, in material systems where E_T is fixed, the temperature-dependent thermopower alone can be a powerful tool to monitor the shift in E_F as a function of doping.^[11] This is studied in Chapter 5. The position of E_T as well as E_F may also show temperature dependent shifts. However, the shifts in these energy levels do not affect the slope of temperature-dependent thermopower, which will be discussed below in the analysis of the y-intercept.

4.4 Density of states distribution in PbTe nanocrystal solids

The y-intercepts of the temperature-dependent thermopower also reveal important information regarding the electronic structure of solids constructed from PbTe nanocrystals. The y-intercepts from Figure 4.5(b) (as summarized in Table 4.1) are -61.93 ± 5.81 (A), -110.83 ± 4.07 (B), -303.23 ± 24.62 (C), -370.23 ± 13.90 (D), and -299.98 ± 26.37 mV/K (E), from largest to smallest nanocrystals. There are three contributing factors that affect y-intercept. The first is the heat of transport constant A , which is determined by energy-dependent conductivity $\sigma(E)$. For the case where $D(E)$ and $\mu(E)$ increase as $(E_T - E)^m$, the theoretical prediction^[14,20,35] estimates $A = I + m$. The heat of transport constant for PbTe nanocrystal solids within the monodispersity range mentioned above is estimated around 3 based on the curvature of the optical DOS in Figure 4.8(a) and (e). The second factor is attributed to the variation in DOS gap (and thus E_T) as a function of temperature.^[36-39] Assuming a linear relationship and replacing $E_F - E_T$ term by $E_F - (E_T + \gamma_g T)$ in equation (28) gives

$$\alpha = \frac{k}{e} \left[\frac{(E_F - E_T)}{kT} - \frac{\gamma_g}{k} + A \right] \dots \dots \dots (30)$$

where γ_g is the temperature-dependent DOS gap coefficient. The magnitude as well as the sign of this coefficient is known to have a size dependence,^[40,41] which can deviate

from the bulk value.^[42,43] Although the exact value is unknown, in the size range of 6.4 - 11.5 nm, our measurements suggest that PbTe nanocrystals may have large temperature coefficients ($\gamma_g > 370$ meV/K). This factor contributes to the negative y-intercept of the temperature-dependent thermopower plot, since it is physically impossible for the heat of transport constant to have a negative value. For smaller nanocrystals, the relaxation of quantum confinement due to the thermal expansion of crystallite size and the electron-phonon coupling term dominates the contribution from the thermal expansion of lattice,^[41] shifting the $-\gamma_g/k$ term more negative. Thus, for smaller nanocrystal sizes, the y-intercept shows more negative value. The third factor comes from the shift in E_F ,^[35,44-46] which gives a positive contribution to the y-intercept. In nanocrystal solids, various surface and nonstoichiometric defects may introduce additional energy states near the midgap^[47] which can be asymmetrically distributed throughout the DOS gap. At 0 K, the Fermi energy may lie below the midgap if more defect states are distributed below the mid-gap. Increasing the temperature shifts the Fermi level toward the midgap as the intrinsic carrier dominates the position of the E_F . This effect will dominate in narrow DOS gap nanocrystal solids, which is exhibited as an increasing value in the y-intercept as the size of the nanocrystal increases. Taking the E_F shift into account ($(E_F + \gamma_F T) - E_T$), the following equation summarizes the y-intercept of the temperature-dependent thermopower:

$$\alpha = \frac{k}{e} \left[\frac{(E_F - E_T)}{kT} - \frac{\gamma_g}{k} + \frac{\gamma_F}{k} + A \right] \dots \dots \dots (31)$$

To study the effect of the DOS on the heat of transport constant in detail, samples were prepared such that the edge of the DOS was kept constant and the distance between the DOS edge and the peak was varied by increasing the polydispersity of the nanocrystals. As shown in Figure 4.8(a-c) the TEM image of the nanocrystals and the SAXS profiles indicate two distinct monodisperse (denoted as mono) and polydisperse (poly) nanocrystal samples. Optical absorption measurements (Figure 4.8(d)) show a wider distribution in the first excitonic transition peak for the polydisperse samples but with a common optical DOS edge. Increasing the polydispersity by 50% (as confirmed from SAXS data in Figure 4.8(c) showed negligible change in $E_F - E_T$ as evidenced by the similar slope in Figure 4.9(a), and the average size of the nanocrystals only decreased by 0.32 nm. The larger y-intercept of the temperature-dependent thermopower plots observed in the monodisperse nanocrystal solid can be attributed to a higher heat of transport constant (since other parameters are fixed). The increase in the heat of transport constant can be understood by estimating the distribution of mobile carriers inside the DOS and predicting the average kinetic energy. This is conducted by multiplying the Fermi distribution function $f(E)$ with $D(E)$ and taking the average of the distribution. From Figure 4.9(b),

the distance between E_T and the average kinetic energy of carriers E_{avg} is larger in monodisperse nanocrystal solid. Although the contribution from $\mu(E)$ may also increase the y-intercept, it is expected that a sharper distribution of the DOS shifts the average kinetic energy further away from the E_T , thereby increasing the heat of transport constant in the current study.

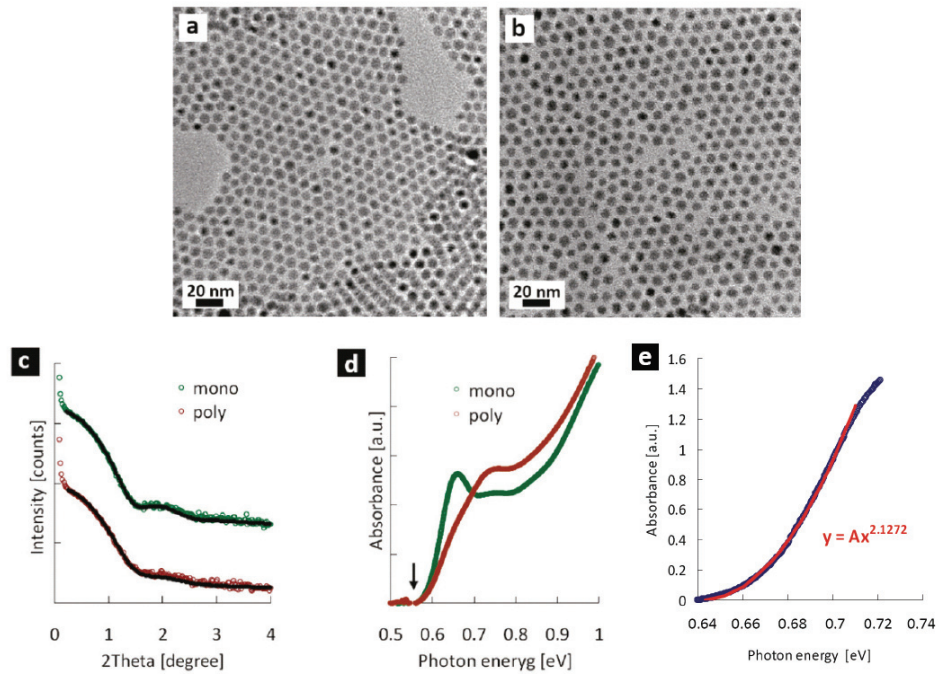


Figure 4.8 TEM image of (a) monodisperse and (b) polydisperse PbTe nanocrystals. (c) Fitting scattering profiles (shown in solid line) indicate that monodisperse nanocrystals have average size and distribution of $7.77 \text{ nm} \pm 9.6\%$ and $7.45 \text{ nm} \pm 14.3\%$ for polydisperse nanocrystals. (d) Corresponding absorption spectra for two samples. Arrow indicates the common edge of optical DOS. (e) Estimation of heat of transport constant from the curvature of the optical DOS.

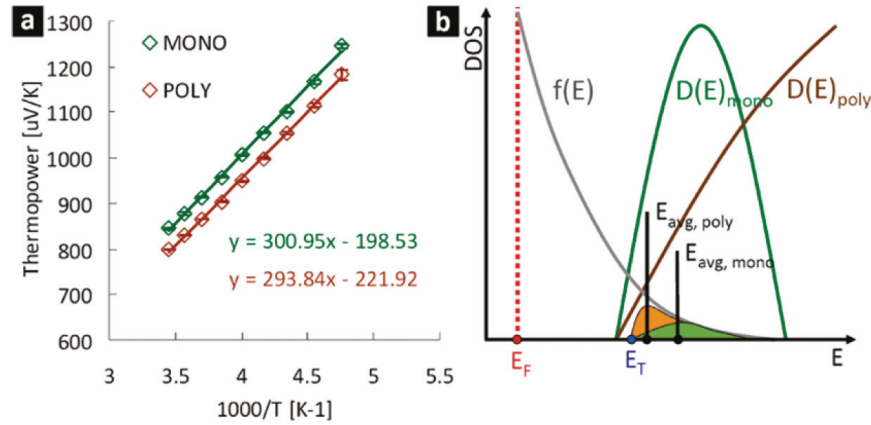


Figure 4.9 (a) Temperature-dependent thermopower measurements performed on both monodisperse and polydisperse nanocrystal solids. The y-intercept of the linear fit is higher in monodisperse nanocrystal solids due to the increase in heat of transport constant. (b) Schematic diagram (not to scale) of carrier distribution in monodisperse and polydisperse nanocrystal solid to estimate the average kinetic energy and the heat of transport constant.

Sharp peaks in DOS have been theoretically^[48-50] and experimentally^[51,52] predicted to increase thermopower. Nanocrystal solids inherently possess sharp DOS compared to that of the bulk counterpart. In nondegenerate PbTe nanocrystal solids, current analysis reveals that sharp distribution of DOS increases the heat of transport constant A , thereby increasing the thermopower. This study provides a general strategy for maximizing the thermoelectricity in materials composed of nanocrystals. Minimizing the size distribution of the nanocrystals sharpens the DOS peak, which is expected to increase not only the thermopower, but also the electrical conductivity, by reducing energy level variations. This, in turn, maximizes thermoelectric power factor ($S^2\sigma$) of semiconductor nanocrystal solid systems (with a given carrier concentration).

4.5 Conclusion

The purpose of this study was to apply temperature-dependent thermopower measurements on nanocrystal solids to investigate $E_F - E_T$ and the heat of transport constant A . By varying the size of the nanocrystals in a solid we have examined the change in $E_F - E_T$, which was primarily due to the change in the DOS gap. Furthermore, the change in the y-intercept of the temperature-dependent thermopower plot as a function of nanocrystal size as well as monodispersity enabled us to study additional terms reflecting the electronic structure and properties of nanocrystal solids and to explore a strong dependence of the heat of transport constant on the DOS distribution. Most of the studies on nanocrystal solids to date have focused on the introduction of electric fields or light to investigate charge carrier transport properties. Electrons and holes, however, are not only charge carriers, but also heat carriers. Therefore, by applying external heat, thermopower measurements can provide a unique perspective on carrier transport studies in nanocrystal solid systems.

References

1. Konstantatos, G.; Howard, I.; Fischer, A.; Hoogland, S.; Clifford, J.; Klem, E.; Levina, L.; Sargent, E. H. Ultrasensitive Solution-Cast Quantum Dot Photodetectors. *Nature* **2006**, *442*, 180-183.

2. Kang, M. S.; Lee, J.; Norris, D. J.; Frisbie, C. D. High Carrier Densities Achieved at Low Voltages in Ambipolar PbSe Nanocrystal Thin-Film Transistors. *Nano Lett.* **2009**, *9*, 3848-3852.
3. Wang, R. Y.; Fesser, J.; Lee, J. -S.; Talapin, D. V.; Segalman, R.; Majumdar, A. Enhanced Thermopower in PbSe Nanocrystal Quantum Dot Superlattices. *Nano Lett.* **2008**, *8*, 2283-2288.
4. Beard, M. C.; Hillhouse, H. W. Solar Cells from Colloidal Nanocrystals: Fundamentals, Materials, Devices, and Economics. *Curr. Opin. Colloid. In.* **2009**, *14*, 245-259.
5. Nozik, A. J. Quantum Dot Solar Cells. *Physica E* **2002**, *14*, 115-120.
6. Luther, J. M. *et al.* Schottky Solar Cells Based on Colloidal Nanocrystal Films. *Nano Lett.* **2008**, *8*, 3488-3492.
7. Gur, I.; Fromer, N. A.; Geier, M. L.; Alivisatos, A. P. Air-Stable All-Inorganic Nanocrystal Solar Cells Processed from Solution. *Science* **2005**, *310*, 462-465.
8. Sun, B.; Findikoglu, A. T.; Sykora, M.; Werder, D. J.; Klimov, V. I. Hybrid Photovoltaic Based on Semiconductor Nanocrystals and Amorphous Silicon. *Nano Lett.* **2009**, *9*, 1235-1241.
9. Greenham, N. C.; Peng, X.; Alivisatos, A. P. Charge Separation and Transport in Conjugated-Polymer/Semiconductor-Nanocrystal Composites Studied by Photoluminescence Quenching and Photoconductivity. *Phys. Rev. B* **1996**, *54*, 17628–17637.
10. Arango, A. C.; Oertel, D. C.; Xu, Y.; Bawendi, M. G. Heterojunction Photovoltaics Using Printed Colloidal Quantum Dots As a Photosensitive Layer. *Nano Lett.* **2009**, *9*, 860-863.
11. Ko, D.-K.; Urban, J. J.; Murray, C. B. Carrier Distribution and Dynamics of Nanocrystal Solids Doped with Artificial Atoms. *Nano Lett.* **2010**, *10*, 1842-1847.
12. Chandler, R. E; Houtepen, A. J.; Nelson, J.; Vanmaekelbergh, D. Electron Transport in Quantum Dot Solids: Monte Carlo Simulations of the Effects of Shell Filling, Coulomb Repulsion, and Site Disorder. *Phys. Rev. B* **2007**, *75*, 085325.
13. Van de Lagemaat, J. Einstein Relation for Electron Diffusion on Arrays of Weakly Coupled Quantum Dots. *Phys. Rev. B* **2005**, *72*, 235319.
14. Fritzsche, H. A General Expression for the Thermoelectric Power. *Solid State Commun.* **1971**, *9*, 1813–1815.
15. Rowe, D. M. *Thermoelectrics Handbook: Macro to Nano*; CRC Press, 2006.
16. Tilley, R. J. D. *Principles and Applications of Chemical Defects*; CRC Press, 1998.
17. Wood, C.; Emin, D. Conduction Mechanism in Boron Carbide. *Phys. Rev. B* **1984**, *29*, 4582-4587.
18. von Mühlennen, A.; Errien, N.; Schaer, M.; Bussac, M. N.; Zuppiroli, L. Thermopower Measurements on Pentacene Transistors. *Phys. Rev. B* **2008**, *75*, 115338.
19. Emin, D. Thermoelectric Power Due to Electronic Hopping Motion. *Phys. Rev. Lett.* **1975**, *35*, 882-885.

20. Baily, S. A.; Emin, D. Transport Properties of Amorphous Antimony Telluride. *Phys. Rev. B* **2006**, *73*, 165211.
21. Resel, R.; Gratz, E.; Burkov, A. T.; Nakama, T.; Higa, M.; Yagasaki, K. Thermopower Measurements in Magnetic Fields up to 17 Tesla Using the Toggled Heating Method. *Rev. Sci. Instrum.* **1996**, *67*, 1970-1975.
22. Cusack, N. E.; Neale, F. E. Thermoelectric Power Near the Critical Point of Expanded Fluid Mercury. *J. Phys. F: Metal Phys.* **1979**, *9*, 85-94.
23. Yao, M.; Endo, H. Thermoelectric Power of Expanded Fluid Mercury and Dilute Amalgams. *J. Phys. Soc. Jpn.* **1982**, *51*, 1504-1509.
24. Brochert, H. *et al.* Determination of Nanocrystal Sizes: A Comparison of TEM, SAXS, and XRD Studies of Highly Monodisperse CoPt₃ Particles. *Langmuir* **2005**, *21*, 1931-1936.
25. Reiker, T.; Hanprasopwattana, A.; Datye, A.; Hubbard, P. Particle Size Distribution Inferred from Small-Angle X-ray Scattering and Transmission Electron Microscopy. *Langmuir* **1999**, *15*, 638-641.
26. Kotlarchyk, M.; Chen, S.-H. Analysis of Small Angle Neutron Scattering Spectra from Polydisperse Interacting Colloids. *J. Chem. Phys.* **1983**, *79*, 2461-2469.
27. Urban, J. J.; Talapin, D. V.; Shevchenko, E. V.; Murray, C. B. Self-Assembly of PbTe Quantum Dots into Nanocrystal Superlattices and Glassy Films. *J. Am. Chem. Soc.* **2006**, *128*, 3248-3255.
28. Murphy, J. E. *et al.* PbTe Colloidal Nanocrystals: Synthesis, Characterization, and Multiple Exciton Generation. *J. Am. Chem. Soc.* **2006**, *128*, 3241-3247.
29. Mokari, T.; Zhang, M.; Yang, P. Shape, Size, and Assembly Control of PbTe Nanocrystals. *J. Am. Chem. Soc.* **2007**, *129*, 9864-9865.
30. Lu, W.; Fang, J.; Stokes, K. L.; Lin, J. Shape Evolution and Self Assembly of Monodisperse PbTe Nanocrystals. *J. Am. Chem. Soc.* **2004**, *126*, 11798-11799.
31. Talapin, D. V.; Murray, C.B. PbSe Nanocrystal Solids for n- and p-Channel Thin Film Field-Effect Transistors. *Science* **2005**, *310*, 86-89.
32. Law, M. *et al.* Structural, Optical, and Electrical Properties of PbSe Nanocrystal Solids Treated Thermally or with Simple Amines. *J. Am. Chem. Soc.* **2008**, *130*, 5974-5985.
33. Kucur, E.; Riegler, J.; Urban G. A. ; Nann, T. Determination of Quantum Confinement in CdSe Nanocrystals by Cyclic Voltammetry. *J. Chem. Phys.* **2003**, *119*, 2333-2337.
34. Colvin, V. L.; Alivisatos, A. P. Valence-Band Photoemission from a Quantum-Dot System. *Phys. Rev. Lett.* **1991**, *66*, 2786-2789.
35. Jones, Di. I.; Le Comber, P. G.; Spear, W. E. Thermoelectric Power in Phosphorous Doped Amorphous Silicon. *Philos. Mag.* **1977**, *36*, 541-551
36. Emim, D. Effect of Temperature-Dependent Band Shifts on Semiconductor Transport Properties. *Solid State Commun.* **1977**, *22*, 409-411.

37. Edmond, J. T. Electronic Conduction in As_2Se_3 , $\text{As}_2\text{Se}_2\text{Te}$ and Similar Materials. *Brit. J. Appl. Phys.* **1966**, *17*, 979-989.
38. Mahadevan, S.; Rao, K. J. Thermoelectric Power of As-Se-Te Glasses, *J. Non-Cryst. Solids*, **1979**, *34*, 53-62.
39. Moustakas, T. D.; Weiser, K; Grant, A. J. Anomalous Thermoelectric Power of Some Liquid Chalcogenide Systems. *Solid State Commum.* **1975**, *16*, 575-579.
40. Olkhovets, A.; Hsu, R. -C.; Lipovskii, A.; Wise, F. W. Size-Dependent Temperature Variation of the Energy Gap in Lead-Salt Quantum Dots. *Phys. Rev. Lett.* **1998**, *81*, 3539-3542.
41. Dai, Q. *et al.* Size-Dependent Temperature Effects on PbSe Nanocrystals. *Langmuir*, **2010**, *26*, 11435-11440.
42. Baleva, M.; Georgiev, T.; Lashkarev, G. On the Temperature Dependence of the Energy Gap in PbSe and PbTe. *J. Phys.: Condens. Matter* **1990**, *2*, 2935-2940.
43. Keffer, C.; Hayes, T. M.; Bienenstock, A. Debye-Waller Factors and the PbTe Band-Gap Temperature Dependence. *Phys. Rev. B* **1970**, *2*, 1966-1976.
44. Elliott, E. R. *Physics of Amorphous Materials*; Longman Scientific & Technical, 1990.
45. Spear, W. E. Doped Amorphous Semiconductors. *Adv. Phys.* **1977**, *26*, 811-845.
46. Beyer, W.; Medeišis, A.; Mell, H. Unusual Temperature Dependence of the Thermoelectric Power of Phosphorous-Doped Amorphous Silicon. *Commun. Phys.* **1977**, *2*, 121-125.
47. Hoang, K; Mahanti, S. D.; Jena, P. Theoretical Study of Deep-Defect States in Bulk PbTe and in Thin Films. *Phys. Rev. B* **2007**, *76*, 115432.
48. Hicks, L. D.; Dresselhaus, M. S. Thermoelectric Figure of Merit of a One-Dimensional Conductor. *Phys. Rev. B* **1993**, *47*, 16631.
49. Mahan, G. D.; Sofo, J. O. The Best Thermoelectric. *Proc. Natl. Acad. Sci.* **1996**, *93*, 7436-7439.
50. Shakouri, A. Thermoelectric, Thermionic, Thermophotovoltaic Energy Conversion. *Int. Conf. Thermoelect.* **2005**, 492-497.
51. Heremans, J. P.; Jovovic, V.; Toberer, E. S.; Saramat, A.; Kurosaki, K.; Charoenphakdee, A.; Yamanaka, S.; Snyder, G. J. Enhancement of Thermoelectric Efficiency in PbTe by Distortion of the Electronic Density of States. *Science* **2008**, *321*, 554-557.
52. Heremans, J.; Thrusch, C. M. Thermoelectric Power of Bismuth Nanowires. *Phys. Rev. B* **1999**, *59*, 12579-12583.

5. PbTe Nanocrystal Solids Doped with Ag₂Te Artificial Atoms

5.1 Introduction

The energy levels that electrons and holes can occupy in an isolated semiconductor NC are discrete and possess atomic symmetries (s, p, d, etc.) in analogy to energy levels in atomic systems.^[1,2] When these nanocrystals (NCs) are brought closely together and packed into a dense, periodic array, the electron wave functions on individual NCs can begin to overlap (electronic exchange coupling) and delocalize throughout the assembly. This leads to formation of a collective miniband,^[3] analogous to the manner by which electronic structure of bulk solids is built from coupled atomic states. In reality, however, NC solids often suffer from inherent disorder due to variations in NC size, shape, and surface termination and from packing disorder. When the energetic fluctuation associated with this disorder is larger than the energy of electronic coupling, the physical properties of these systems can more closely resemble that of noncrystalline materials, such as the well-known cases of transport in liquid metals and amorphous semiconductors.^[4,5] In such disordered systems, charge transport occurs via hopping between localized states^[6-9]

and macroscopic carrier transport is strongly influenced by the microscopic fluctuating energy landscape. However, understanding the role of these energy level fluctuations is extremely challenging to rationally investigate, a problem which has prevented a deep understanding of charge carrier transport in NC solids to date.

One method to explore the role of energy fluctuations in transport is to deliberately substitute host NCs with other classes of NCs of known electronic and dielectric properties, as a means of doping.^[10] This new concept of “artificial atom” doping enables us to tailor the electronic properties of NC solids. By adjusting the concentration of dopant NCs, a desired doping level can be readily achieved in NC solid systems. A systematic investigation of how doping affects the electronic properties requires monitoring both changes in Fermi energy level (E_F) as well as the amount of disorder which will change the details of the charge transport process. In this study, we apply temperature-dependent thermopower and conductivity measurements to investigate the effects of doping in NC solid systems. We utilize glassy NC solids (Bernal random packing of binary NC mixtures) to ensure that the introduction of dopant NCs does not trigger undesired structural transformations. Moreover, NC size, concentration, and deposition method were deliberately chosen to avoid the formation of ordered binary phases that will complicate interpretation of the carrier transport data.

5.2 Experimental Details

Monodisperse PbTe nanocrystals with average size of 7 ± 0.4 nm and first absorption features at 1780 nm are prepared using the previously mentioned procedure. For the synthesis of monodisperse silver telluride NCs, 7.17 g of AgCl (Aldrich, 99%) is dissolved in 50 mL tri-n-octylphosphine (TOP, Aldrich, 90%) and 4.79 g of tellurium shot (Aldrich, 99.999%) is dissolved in 50 mL TOP to prepare 1M Ag-TOP and 0.75 M TOP-Te, respectively. 8.13 g of oleylamine (Fluka, >70%) is heated to 160 °C and 5 mL of Ag-TOP and 2.5 mL of TOP-Te is promptly injected and aged at 140 °C overnight. The reaction is then quenched in a water bath and diluted with 10 mL of hexane. The dilute sample solution is centrifuged to discard the precipitate. NCs remaining in the supernatant are extracted and purified using hexane and methanol. Highly monodisperse NCs were obtained with average size of 3 nm and first absorption feature at 1160 nm. Both NC solutions are passed through 0.2 μ m filter twice and re-dissolved in a hexane/octane mixture and stored under nitrogen atmosphere. Mixtures of Ag₂Te/PbTe samples were also prepared for doping studies. Three different Ag₂Te/PbTe particle number ratios of 1/100, 1/10, and 1 (Ag₂Te/PbTe compound mass percent ratio of 1/97.50, 1/9.75, 1/0.97) were determined statistically by transmission electron microscopy (TEM, JEOL-2010F) observations. Optical absorption data (Analytical Spectral Devices QSP 350-2500) were acquired from the

sample dispersed in tetrachloroethylene (TCE, Aldrich, >90%).

For electrical conductivity measurements, a degenerately doped silicon substrate with a 200 nm thermal oxide is photolithographically patterned with Au/Cr (95 nm/5 nm) electrodes. The channel length and width is 5 μm and 5000 μm , respectively. NCs or binary mixtures of NCs were drop-cast on this pre-patterned substrate and subsequently treated with 1M hydrazine (Aldrich, anhydrous, 98%) in acetonitrile (Aldrich, anhydrous, 99.8%) overnight. Depositions and treatments are repeated several times to electronically activate the NC film with a final thickness of 80 ± 20 nm (SEM cross-section measurements, FEI Strata DB235). Temperature-dependent conductivity measurements were performed using a variable temperature microprobe system K-20 from MMR technologies coupled with HP 4145B semiconductor parameter analyzer.

Samples for thermopower measurements are deposited on a glass substrate with a 5 times more concentrated NC solution and chemically treated as mentioned above for electrical conductivity samples. Thermopower measurements are performed using MMR technologies K-20 and SB-100 with a high impedance amplifier (1000 gain). Each data point represents an average of 8 readings and 3 data points were collected at each designated temperature. Copper-constantan is used as a reference junction to monitor temperature difference. Both thermopower and conductivity

measurements were performed under < 8 mTorr vacuum with the temperature varying from 375K to 225K. Below 225K, samples were too electronically resistive for thermopower measurements.

5.3 Electronic Spectroscopy of PbTe Nanocrystal Solids

The experimental configurations of the temperature-dependent thermopower and conductivity measurements are illustrated in Figure 5.1(a) and (b). From the thermopower equation derived in chapter 4.3 (equation (28)), there are two critical pieces of information clearly revealed from thermopower measurements: carrier type and carrier density. The sign of the thermovoltage provides information about whether the material is n-type or p-type and the temperature-dependent measurement directly reveals the position of E_F with respect to E_T . This is obtained from the activation energy for thermopower $E_S (= E_F - E_T)$ by taking the intercept of the thermopower versus inverse temperature plot as shown from the equation in Figure 5.1(a). Electrical conductivity is given by the relation $\sigma = en\mu$ where e is carrier charge, n is carrier concentration, and μ is the mobility. For electrical transport to occur in semiconductors, charge carriers must first be excited to E_T . This activation energy for charge carrier generation is $E_T - E_F$. In the case of hopping transport within a strongly

fluctuating energy landscape, these charges need additional energy to surmount the highest energy barrier, represented as E_μ (activation energy for hopping mobility) in order to participate in electrical conduction. The activation energy for conductivity (E_σ) must therefore account for both contributions ($E_F - E_T$) and E_μ .^[23,26] Thus, electrical conductivity is expressed as

$$\sigma = eN_T \exp\left(\frac{E_F - E_T}{kT}\right) \mu_0 \exp\left(\frac{E_\mu}{kT}\right) \dots\dots\dots(32)$$

where N_T is the effective density of states at the transport level and μ_0 is the mobility prefactor. We are able to measure E_σ through temperature-dependent conductivity measurements as shown in the equation in Figure 5.1(b). Furthermore, by combining the data from both temperature-dependent thermopower and temperature-dependent conductivity measurements, we determine E_μ ($= E_\sigma - E_S$). This is critical information for understanding how transport in NC solids will be influenced by doping. Our experiments indicate that as we substitute dopant NCs into the host NC solid, we shift the E_F but also change E_μ with greater energy level fluctuations in the doped NC solid. This enables predictive modeling of how the introduction of dopants into NC films influences carrier density and transport behavior. Temperature-dependent conductivity measurements alone cannot separate both parameters in experiments on a doped NC film. The difference in E_S versus E_σ , as illustrated in Figure 5.1(c), is due to

the fact that mobility is thermally activated. This activation energy contributes to temperature-dependent electrical conductivity but not to thermopower because the mobility activation term in $\sigma(E)$ and σ cancel out in equation (8). E_S is, therefore, the energetic difference between E_F and the energy fluctuation minimum indicated in Figure 5.1(c). On the other hand, in order for charge carriers to participate in the conduction process, they need to surmount the highest energy barrier. Thus, E_σ is the highest energy peak from the E_F , as indicated in Figure 5.1(c). From the difference between these two activation energies, we can also estimate the amplitude of energy fluctuation, $\Delta E (= E_\mu)$, which strongly affect the transport process.

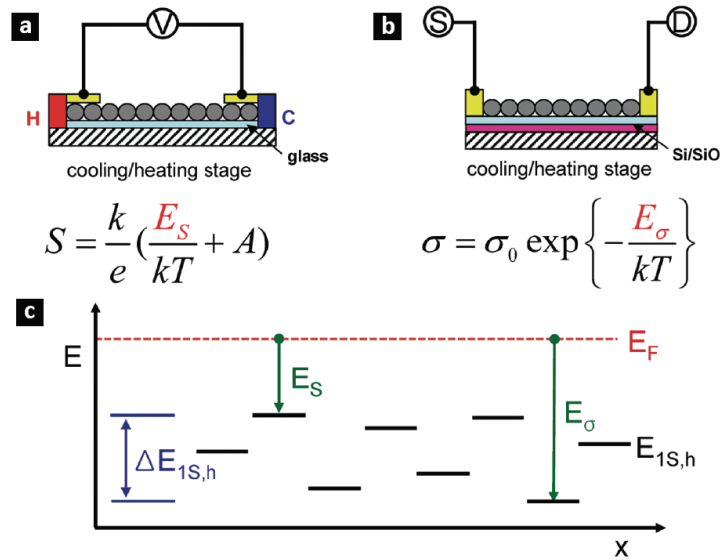


Figure 5.1 Temperature-dependent thermopower and electrical conductivity measurements on NC solids. (a, b) Schematic diagram in cross section of thermopower and electrical conductivity measurement devices. For transport involving thermally activated hopping of holes in a single transport level, general expressions for thermopower and conductivity are given below. (c) Sketch of energy level fluctuation of highest occupied electronic states $E_{1S,h}$ of NC solid affecting thermopower and conductivity.

Figure 5.2 shows the temperature-dependent thermopower and conductivity measurements performed on PbTe NC solids. Both thermopower and conductivity exhibit thermally activated behavior. Positive thermopower indicates that majority carriers are holes and that E_F is positioned below the midgap. E_S is calculated from the slope of thermopower versus inverse temperature as in Figure 5.2(b) and the position of E_F is estimated to be above the first hole transport level $E_{IS,h}$ by 75 meV. E_σ is similarly calculated from $\ln\sigma$ versus inverse temperature and is 163 meV as shown in Figure 5.2(c). From these two activation energies, we calculate an E_μ of 88 meV in close agreement with the variation in $E_{IS,h}$, estimated from the full width half-maximum (FWHM) of the first excitonic transition (~ 91 meV) from Figure 5.2(a). This also suggests that the charging energies of PbTe NCs are negligible in the transport process, which is reasonable for a high dielectric constant material ($E_C \sim 0.02kT$ at 300K).^[11] Based upon the conclusions from the transport data, we are able to construct an energy vs density of states diagram for PbTe NC solids, shown in Figure 5.2(d). The broadening of $E_{IS,h}$ is due to variation in quantum confinement (sizes), and these energy states do not necessarily reflect extended states. Oxidation is well-known to create acceptor levels near the valence band in bulk PbTe via chemisorption of oxygen on the surface. This is expected to be more prevalent in NC systems even under brief air exposure^[12] and is represented by broadly distributed

states near $E_{IS,h}$. These acceptor states trap electrons inside the NCs and increase the hole concentration leading to p-type NC films.

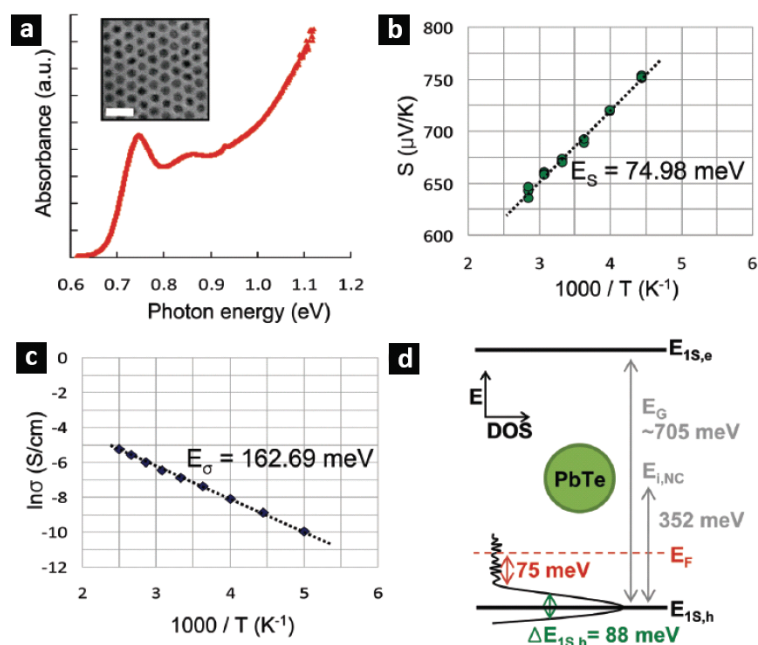


Figure 5.2 Thermopower and conductivity measurements of an lead telluride NC solid. (a) Optical absorption spectrum of PbTe NCs. Inset shows TEM image of monodisperse PbTe NCs used for measurements. Scale bar is 20 nm. (b) Plot of thermopower ($\Delta T = 1.5$ K) as a function of inverse temperature. (c) Plot of low-bias electrical conductivity (0.01 V) as a function of inverse temperature. (d) Schematic of energy vs density of states diagram of PbTe NC solid constructed from both measurements.

5.4 Electronic Spectroscopy of Ag_2Te Nanocrystal Solids

The analogous set of temperature-dependent thermopower and electrical conductivity measurements performed on Ag_2Te NC solids are shown in Figure 5.3.

Negative thermopower indicates that material is n-type, which is expected to result

from a nonstoichiometric ratio (excess in Ag).^[13] However, in the case of Ag₂Te NC solids, the thermovoltage measurement does not exhibit thermally activated behavior. Here, thermovoltages increase with respect to temperature, but with a weaker temperature dependence, which is typical behavior of degenerately doped semiconductors or metals.^[14] This suggests that the E_F lies within the broadened $E_{1s,e}$ electronic states and that no activation is necessary for carrier generation in the measured temperature range. This is supported by the fact that E_σ only comes from the hopping mobility contribution. Good agreement between the slope of 150 meV determined by the plot of $\ln\sigma$ versus $1/T$ in Figure 5.3(c) and the variation in $E_{1s,e}$ (~ 154 meV) obtained from the absorption spectrum in Figure 5.3(a) indicates that for electronic conduction only E_μ is needed. Similar to PbTe NC systems, the charging energy of Ag₂Te is negligible. Finally, the energy vs density of state diagram predicted for Ag₂Te NC solid with widely distributed donor levels near the $E_{1s,e}$ is shown in Figure 5.3(d).

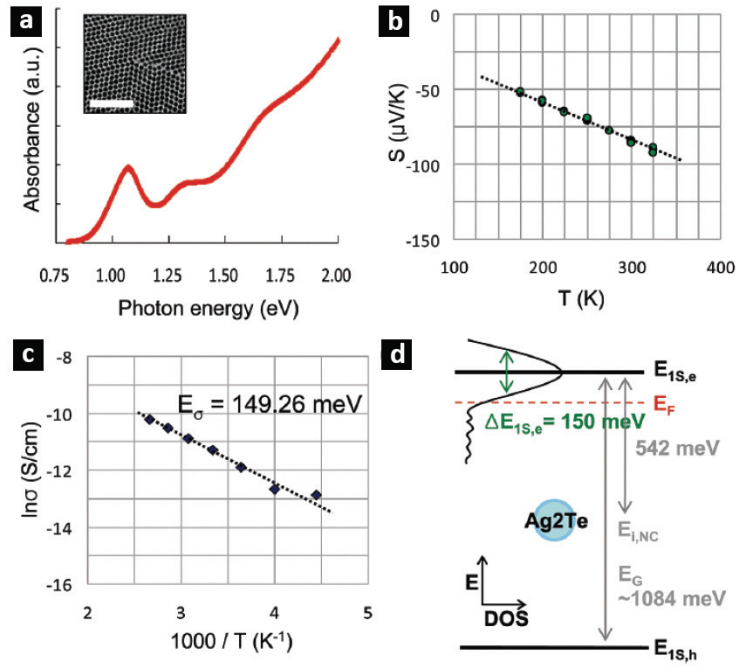


Figure 5.3 Thermopower and conductivity measurement on silver telluride NC solid. (a) Optical absorption spectrum of Ag₂Te NCs. Inset shows TEM image of monodisperse Ag₂Te NCs used in measurements. Scale bar is 50 nm. (b) Thermopower ($\Delta T = 1.7$ K) as a function of inverse temperature. (c) Low-bias electrical conductivity (0.01 V) as a function of inverse temperature. (d) Schematic of energy vs density of state diagram constructed from both measurements.

5.5 PbTe Nanocrystal Solids with Ag₂Te Nanocrystal Dopants

To investigate how the introduction of dopant NCs affects carrier concentration and transport characteristics, PbTe NC solids with three different Ag₂Te doping levels (represented as three different Ag₂Te/PbTe ratios, Figure 5.4) were studied.

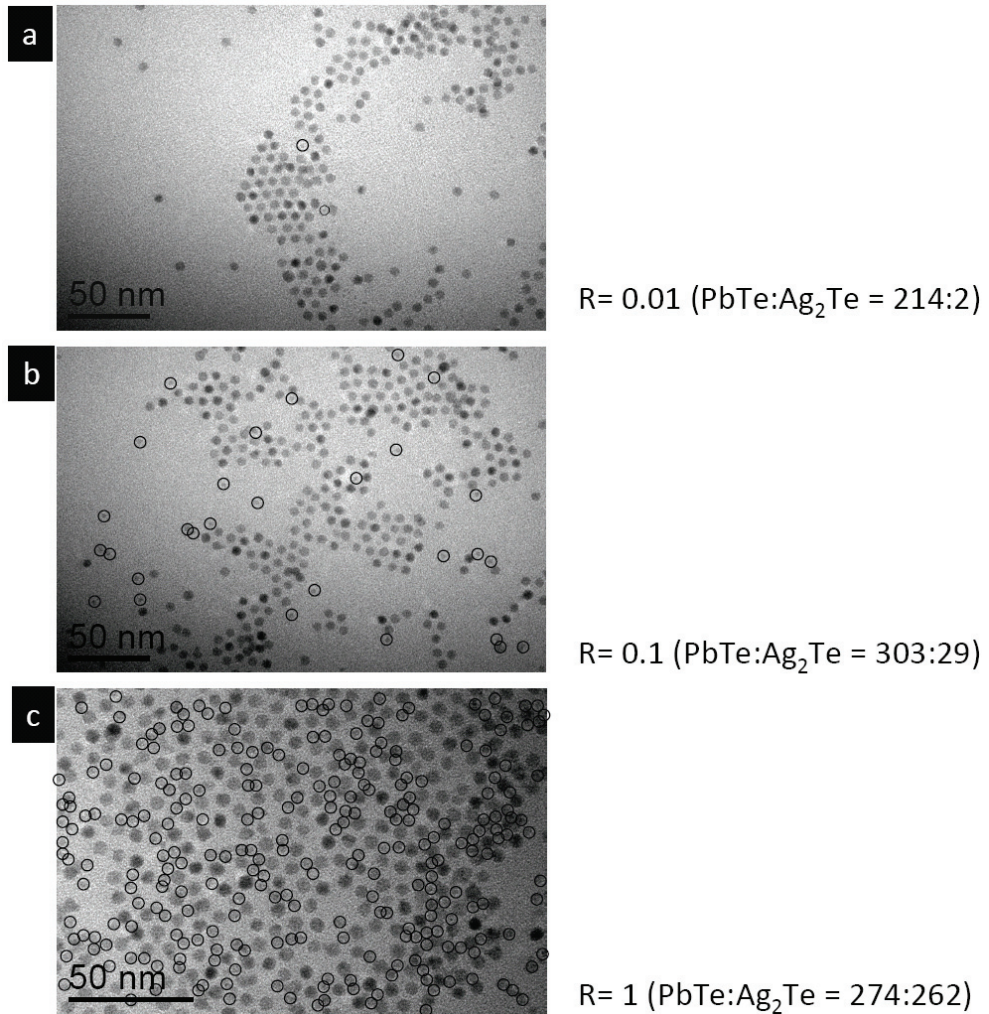


Figure 5.4 TEM image of diluted PbTe/Ag₂Te nanocrystal samples used for the statistical determination of mixture ratios. Mixture ratios of R= 0.01 (100 PbTe nanocrystals per 1 Ag₂Te nanocrystals), 0.1, and 1 is shown in (a), (b), and (c), respectively.

Structural characterizations of nanocrystal solid samples were performed using reflection-mode SAXS (Figure 5.5). Single component nanocrystal solid is found to form face-centered cubic (FCC) structures as shown in Figure 5.6 (a, b, c). Using the FCC packing model (Figure 5.6 (d)), the interparticle distance was

calculated from the first Bragg peak which represent (111) reflection from the out-of-plane direction. The NC center-to-center distance of PbTe NC solid is 7.83 nm where 1.33 nm is the oleic acid spacer distance. For Ag₂Te, NCs are separated by 4.19 nm which gives 1.39 nm of oleylamine spacer distance. On the other hand, solids formed from mixtures of PbTe and Ag₂Te nanocrystals did not show phase segregation. If the PbTe or Ag₂Te do phase segregate, the diffraction peak arising from PbTe nanocrystal domain (as shown in a red circle in Figure 5.5) and Ag₂Te nanocrystal domain (blue diamond) would superimpose and are not present for the solid with Ag₂Te/PbTe mixture (green triangle, R = 0.1). Using the packing model illustrated in Figure 5.6 (e) where, Ag₂Te nanocrystals occupy the tetrahedral sites of PbTe FCC structure, the PbTe to PbTe inter-particle distance increases to 8.72 nm compared to that of PbTe NC solids. The PbTe to Ag₂Te distance were calculated as 5.35 nm where 0.7 nm is the oleic acid / oleylamine ligand spacing.

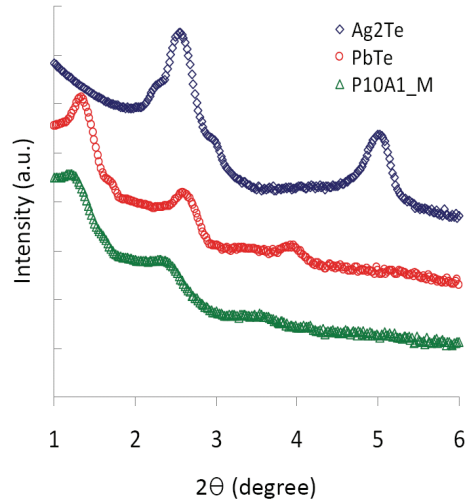


Figure 5.5 Reflection-mode SAXS studies on as-deposited (before hydrazine treatment) NC solid film. SAXS profiles of PbTe (red circle), Ag₂Te (blue diamond), and 10:1 mixture of Ag₂Te/PbTe (green triangle) NC solids. Mixtures of two NCs do not show phase segregation. If two NCs phase segregate during solidification, two superimposed Bragg peaks arising from PbTe and Ag₂Te domains would be anticipated and are not observed here.

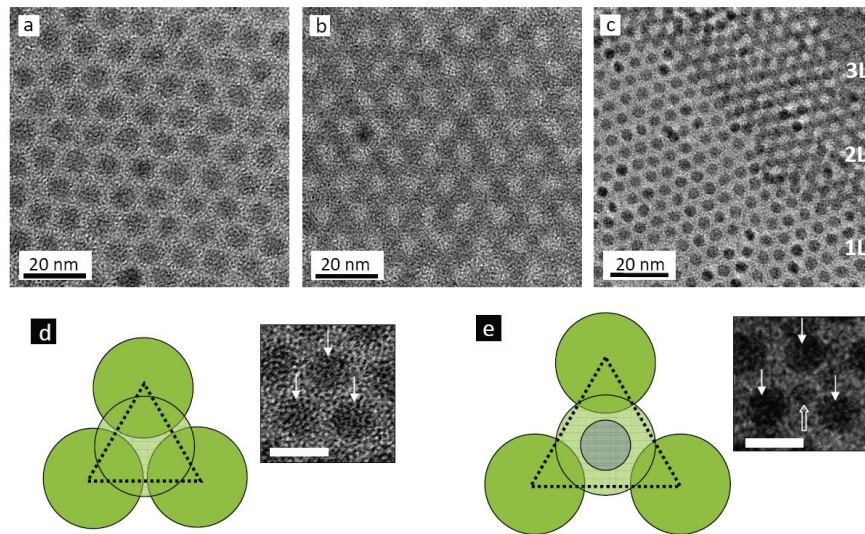


Figure 5.6 TEM images of (a) monolayer, (b) double layer, and (c) a triple layer of PbTe nanocrystal assemblies. The absence of empty space of the triple layer (denoted as 3L in (c)) indicates FCC packing. (d) FCC packing model to calculate the interparticle spacing. Inset shows the TEM image of PbTe nanocrystals. (e) Packing model used to calculate the interparticle spacing when Ag₂Te nanocrystals occupy tetrahedral sites. Inset shows the TEM image obtained from R = 0.1 mixture. Solid arrows indicate PbTe nanocrystals and the hollow arrow indicate the Ag₂Te nanocrystal. All scale bars in the inset are 10 nm.

As shown in Figure 5.7(a), all three samples are p-type, as deduced from the positive sign of the measured thermopower. Furthermore, all samples show thermally activated behavior with the activation energy decreasing as the doping ratio increases. This suggests that E_F shifts closer to $E_{IS,h}$ as we increase the $\text{Ag}_2\text{Te}/\text{PbTe}$ ratio indicating that NC films are more p-doped. When unintentionally doped p-type PbTe NC solids are doped with n-type Ag_2Te NCs, electrons and holes in the NC solid recombine until one or both types of carrier are depleted. In present study, thermopower measurements suggest that the predominance of holes makes the doped NC solid p-type resulting in a partially compensated semiconductor system for all three doping ratios. This compensation reduces the number of holes in the system, shifting E_F farther away from the hole transport level as supported from E_S of undoped (74.98 meV) and doped ($\text{Ag}_2\text{Te}/\text{PbTe} = 0.01$, 99.31 meV) PbTe NC solids. Surprisingly, adding more n-type Ag_2Te NC makes the NC solid more p-type. Although the exact alignment of energy levels and density of trap states need further examination, we expect that electrons in $E_{IS,h}$ in Ag_2Te are redistributed to nearby trap sites in PbTe NCs leaving behind mobile holes. As shown in Figure 5.7(c), this will dope the NC film p-type and Ag_2Te NCs act as p-type dopants. As we increase the dopant NC concentration, more Ag_2Te NCs which contain free holes in $E_{IS,h}$ are introduced, thus increasing the total number of mobile holes in NC film. On the other

hand, electrical conductivity remains roughly constant for all three ratios, as shown in Figure 5.7(b). In order to interpret this result, E_σ and E_μ were extracted as summarized in Table 5.1. As we introduce more dopant NCs, E_μ significantly increases due to stronger energy level fluctuations affecting charge transport. Thus, even if the carrier concentration is increased by doping in the NC solid, the mobility decreases to a similar extent, leading to invariance in electrical conductivities. One might suggest here that Ag_2Te NC may not directly participate in the conduction process and do not provide energy states that carriers can hop to. If this were the case, the average charge carrier hopping distance would be expected to increase and show a different temperature dependence in electrical conductivity, as captured in the models of variable range hopping (Mott model: $\ln\sigma \propto T^{-1/4}$, Efros-Shklovskii model: $\ln\sigma \propto T^{-1/2}$). However, our temperature-dependent conductivity data in Figure 5.7(b) suggests that, in our measurement temperature range, conductivity is simply thermally activated (nearest neighbor hopping, $\ln\sigma \propto T^{-1}$).

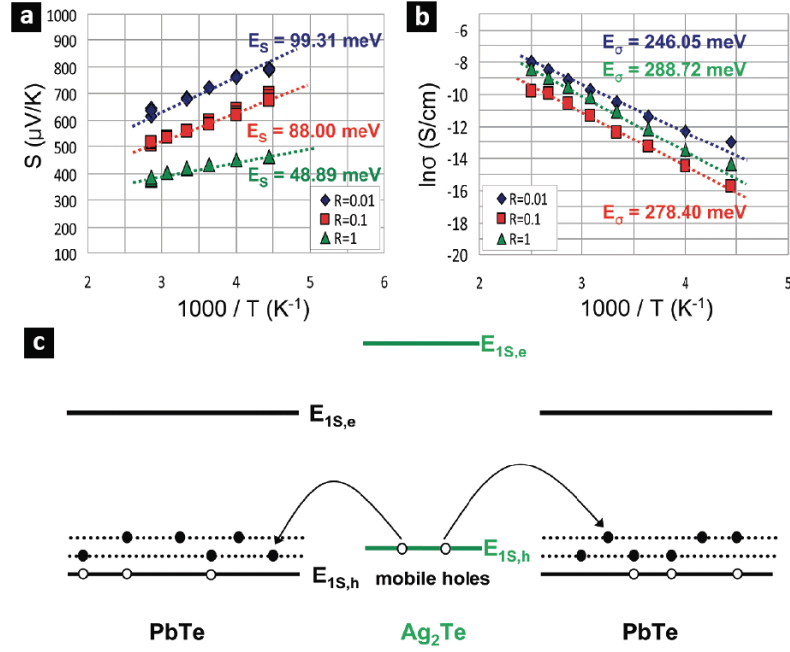


Figure 5.7 Investigation of Ag₂Te NC doping in PbTe NC solids. (a, b) Temperature-dependent thermopower ($\Delta T = 1.5$ K) and conductivity measurements varying three different Ag₂Te/PbTe ratios. (c) Schematic energy diagram of Ag₂Te/PbTe NC solid showing electrons in Ag₂Te filling the trap states of neighboring PbTe NCs after compensation. Adding Ag₂Te NC to PbTe NC film induces mobile holes in Ag₂Te, doping NC solid more p-type.

Ag ₂ Te/PbTe ratio	$S_{300\text{K}}$ (uV/K)	$\sigma_{300\text{K}}$ (S/cm)	E_s (meV)	E_σ (meV)	E_μ (meV)
0.01	682	2.79×10^{-5}	99.31	246.05	146.74
0.1	561	4.39×10^{-6}	88.00	278.40	190.40
1	418	1.54×10^{-5}	48.89	288.72	239.83

Table 5.1 Thermopower, electrical conductivity and their activation energies from Figure 5.7(a) and (b), and hopping mobility activation energies of three different Ag₂Te/PbTe ratios.

5.6 Conclusion

Temperature-dependent measurements of thermopower and electrical conductivity are a powerful probe directly revealing E_F , key to estimating the

concentration of mobile carriers in a solid and elucidating charge transport characteristics in systems with nanoscale heterogeneity. As demonstrated using this technique, the influence of “artificial atom” doping on the electronic structure of NC solids shows both interesting similarities and differences when compared to doping in traditional semiconductor systems. In bulk semiconductors, carrier concentration increases proportionally to the dopant concentration. However, mobility monotonically decreases with doping due to ionized impurity scattering. Similarly, in NC solid systems, carrier concentration increases as the number of dopant NC increases. Carrier mobility also decreases, but due to a different mechanism. Dopant NCs introduce greater fluctuations in energy states which increases E_{μ} . Here we have developed a generally applicable methodology for understanding doping of semiconductor nanocrystal solids using temperature-dependent thermopower and electrical conductivity measurements.

References

1. Steiner, D.; Aharoni, A.; Banin, U.; Millo, O. *Nano Lett.* **2006**, *6*, 2201–2206.
2. Jdira, L.; Overgaag, K.; Gerritsen, J.; Vanmaekelbergh, D.; Liljeroth, P.; Speller, S. *Nano Lett.* **2008**, *8*, 4014–4019.
3. Lazarenkove, O. L.; Balandin, A. A. *J. Appl. Phys.* **2001**, *89*, 5509–5515.
4. Elliot, S. R. *Physics of Amorphous Materials*; Longman: London, 1983.
5. Street, R. A. *Hydrogenated amorphous silicon*; Cambridge University Press: Cambridge,

1991.

6. Yu, D.; Wang, C.; Wehrenberg, B. L.; Guyot-Sionnest, P. *Phys. Rev. Lett.* **2004**, *92*, 216802.
7. Houtepen, A. J.; Kockmann, D.; Vanmaekelbergh, D. *Nano Lett.* **2008**, *8*, 3516–3520.
8. Romero, H. E.; Drndic, M. *Phys. Rev. Lett.* **2005**, *95*, 156801.
9. Mentzel, T. S.; Porter, V. J.; Geyer, S.; Maclean, K.; Bawendi, M. G.; Kastner, M. A. *Phys. Rev. B* **2008**, *77*, No. 075316.
10. Urban, J. J.; Talapin, D. V.; Shevchenko, E. V.; Kagan, C. R.; Murray, C. B. *Nat. Mater.* **2007**, *6*, 115–121.
11. Wise, F. W. *Acc. Chem. Res.* **2000**, *33*, 773–780.
12. Martin, J.; Nolas, G. S.; Zhang, W.; Chen, L. *Appl. Phys. Lett.* **2007**, *90*, 2221122.
13. Schnyders, H. S.; Saboungi, M. -L.; Rosenbaum, T. F. *Appl. Phys. Lett.* **2000**, *76*, 1710–1712.
14. Das, V. D.; Karunakaran, D. *Phys. Rev. B* **1984**, *30*, 2036–2041.

6. Solution-processable nanocomposite with enhanced thermopower

6.1 Introduction

Unlike mechanical heat engines, thermoelectric devices use a material's inherent charge carriers (electrons and holes) to convert heat directly into electricity and vice versa. Despite the simple and environmentally friendly operation, practical uses of thermoelectric materials have been limited by low energy conversion efficiency. The efficiency of a thermoelectric device is expressed in the dimensionless figure of merit ZT which is determined by the material's three unique thermoelectric, electrical, and thermal properties. Although there is no theoretical limit to the practically attainable ZT , maximizing one parameter counteracts the other two which has bounded the figure of merit in conventional bulk materials to near unity. One promising approach to improve ZT is by introducing interfaces^[1-5] to enhance thermopower while minimizing the reduction in electrical conductivity (and to suppress thermal conductivity). Interfaces in a material induce energy-dependent carrier scattering either by introducing potential barriers^[6-9] or wells^[10] to filter carriers with low energy. This was recently demonstrated in materials composed of

thin film superlattices,^[11,12] nanograins,^[13,14] and nanoinclusions^[15-17] which involve molecular beam epitaxy, phase separation, or hot-pressing with restricted material combinations. In this study, we develop the first solution-processable nanocomposites prepared from chemically-synthesized metal nanocrystals and a semiconductor matrix processed from a hydrazine-based metal chalcogenide precursor.^[18-21] A high density of interfaces was introduced using Pt nanocrystal inclusions to filter low energy holes in *p*-type Sb₂Te₃. Thermopower measurements on Pt-Sb₂Te₃ nanocomposites indicate an increase in thermopower with respect to pure Sb₂Te₃ films. Furthermore, Hall effect measurements reveal an increase in carrier concentration, which partially compensates for the decrease in mobility. Thus, at room temperature, a higher thermoelectric power factor was achieved. Nanocomposites constructed from this facile preparation method provide an excellent materials platform to explore diverse sets of nanocrystal-semiconductor matrix combinations.

6.2 Experimental details

Pt nanocubes (and mixtures of truncated octahedrons) with average size of 13.7 ± 2.5 nm were synthesized using a previously reported procedure.^[22] Solution-processable Sb₂Te₃ precursors were prepared by dissolving Sb₂Te₃ powder and four

fold excess of Te in anhydrous hydrazine according to the original recipe reported in literature.^[18,23] TEM micrographs and selected area electron diffraction (SAED) of Sb_2Te_3 film before and after annealing are shown in Figure 6.1. Figure 6.1 (a) and (b) shows as-deposited films without the heat treatment. Sb_2Te_3 crystallizes into rhombohedral structure after heating for 20 minutes at 200°C , as shown in Figure 6.1(c) and (d).

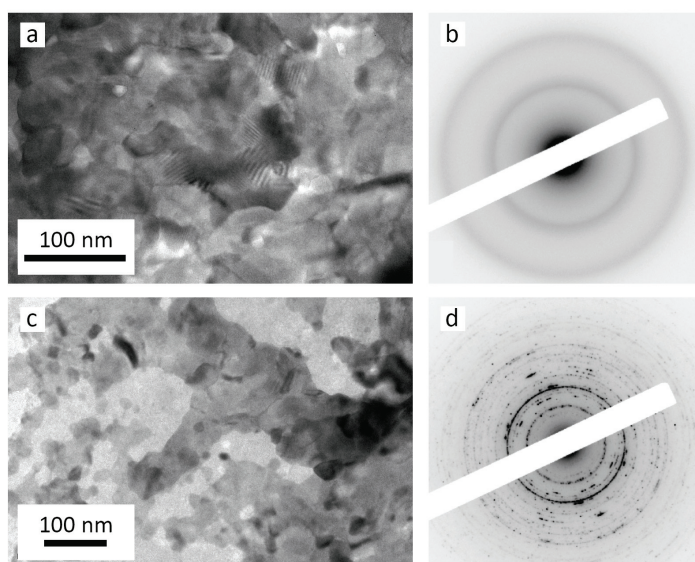


Figure 6.1 TEM micrographs and SAED patterns of films produced from solution-processable Sb_2Te_3 precursors. (a, b) are from as-deposited Sb_2Te_3 films. (c, d) shows Sb_2Te_3 films after annealing at 200°C for 20 minutes.

Pt nanocrystals can be easily transferred and dispersed in hydrazine-based Sb_2Te_3 precursor solutions. The Sb_2Te_3 precursor replaces the organic ligands on Pt nanocrystals^[23,24] enabling them to transfer into the hydrazine phase. As shown in

Figure 6.2(a), by simply mixing Pt nanocrystals in hexane and Sb_2Te_3 precursor in hydrazine, the hexane supernatant becomes colorless indicating that Pt nanocrystals have transferred to the hydrazine phase. A critical step in preserving the structure and composition of Pt nanocrystal is obtaining a stoichiometric Sb_2Te_3 matrix without high temperature annealing. As shown in Figure 6.2(d), annealing the nanocomposite film at 300°C triggers alloying between the nanocrystals and the semiconductor matrix. In order to remove excess Te, the film has to be heated up to 450°C .^[23] This detrimental process can be avoided by annealing the film at 200°C and using TOP treatment to remove elemental Te. Figure 6.2 (b) and (c) show TEM micrographs of as-deposited and 200°C annealed nanocomposite films, respectively.

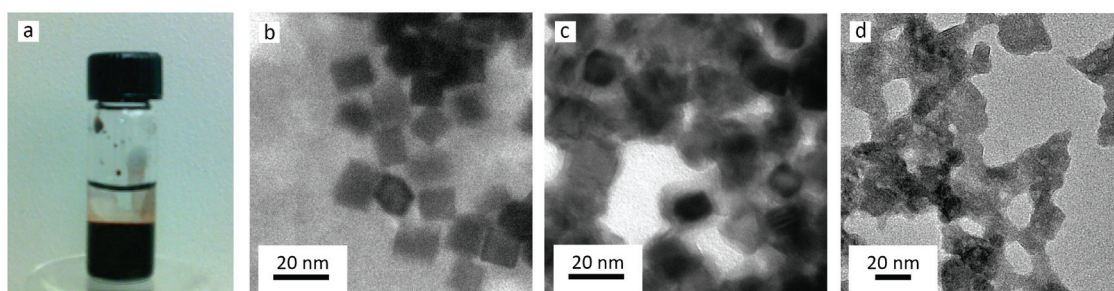


Figure 6.2 (a) Nanocomposite solution after mixing Pt nanocrystals in hexane and hydrazine-based Sb_2Te_3 precursor. Colorless hexane phase indicates that Pt nanocrystals have transferred to the hydrazine phase. (b, c, d) TEM micrographs of as-deposited, 200°C annealed, and 300°C annealed nanocomposite films, respectively.

In a typical procedure, nanocomposite solutions were prepared by vigorously

mixing 2 mL of Pt nanocrystals in anhydrous hexane (5 mg/mL) diluted with 2 mL of anhydrous toluene, and 4 mL of Sb₂Te₃ precursor solution in hydrazine (25 mg/mL) with additional an 2 mL of anhydrous hydrazine. Nanocrystals in the hexane / toluene phase transfer to the hydrazine phase and the supernatant hexane / toluene was removed. Multiple washing steps were performed by rinsing with anhydrous hexane. Final nanocomposite solution with 1:10 Pt to Sb₂Te₃ mass ratio was dropcast on to hydrophilized glass substrates which were prepared via 6 hrs of UV ozone treatment (Novascan PSD Pro UV system) followed by rinsing with DI water. The samples were dried at room temperature for 2 hours, heated to 200°C for 20 minutes, submerged in TOP solution overnight, and then the surface was rinsed with anhydrous hexane. The final thickness of the film was $1.8 \pm 0.2 \mu\text{m}$ confirmed by SEM cross-section (FEI Strata DB235). All procedures were performed in a nitrogen filled glovebox. For Sb₂Te₃ films, a Sb₂Te₃ precursor solution prepared without additional dilution was dropcast and treated with a similar procedure mentioned above for nanocomposite films. The film thickness was $1.7 \pm 0.1 \mu\text{m}$.

Powder XRD was performed on Rigaku Smartlab high resolution diffractometer and EDS spectrum was obtained from JEOL 2010F equipped with Bruker AXS Quantax system. TEM and SEM micrographs were obtained from JEOL JEM 1400 and JEOL 7500F HRSEM.

The nanocomposite (and Sb_2Te_3) film deposited on the glass substrate was mounted on the sample stage using silver paste (Leitsilber 200, Ted Pella). The thermopower measurements were conducted using MMR technologies K-20 and SB-100. Constantan was used as a reference material to monitor temperature difference (ΔT). For the Hall effect measurements, nanocomposite films with square van der Pauw geometry were prepared by selectively cleaning the perimeter with a wooden tip soaked with anhydrous hydrazine. Four small contacts were made at each corner using a silver paste. Four-point probe resistivity as well as Hall effect measurements were performed using MMR technologies H-50 with a 0.5 T magnet. All the measurements were conducted in an inert glove box atmosphere.

6.3 Pt- Sb_2Te_3 nanocomposite with enhanced thermoelectric power factor and carrier energy filtering

Sb_2Te_3 is the state-of-the-art bulk material that exhibits the highest ZT near 50°C. It is used as a p-type thermoelectric element, optimal for waste heat recovery from hot water pipes or the human body.^[4,25] As-prepared Sb_2Te_3 exhibits high carrier concentration (10^{19} - 10^{20} cm^{-3}) without doping which is an ideal system to readily optimize ZT. Sb_2Te_3 films can be prepared from solutions of Sb_2Te_3 and elemental Te

dissolved in anhydrous hydrazine.^[23] This serves as the solution-processable semiconductor matrix for the current study. The chalcogenide precursor also acts as the capping ligand for the nanocrystals which ensures the formation of an abrupt atomic junction with the semiconductor matrix upon hydrazine evaporation. This unique feature has motivated a rapidly developing area for processing all-inorganic nanocomposites previously referred to as metal chalcogenide complexes (MCCs)^[23] and chalcogenidometallate clusters (ChaMs)^[26]. By simply mixing Pt nanocrystals^[22] in hexane phase with the hydrazine-based Sb_2Te_3 solution, Pt nanocrystals are easily transferred to the Sb_2Te_3 solution. After several purification steps, this nanocomposite solution (Pt to Sb_2Te_3 mass ratio = 1:10) can be used to dropcast thin films for further thermoelectric and electronic characterizations.

The band alignment between Sb_2Te_3 and Pt nanocrystals is shown in Figure 6.3(a). Sb_2Te_3 , in general, is a degenerate semiconductor in which the Fermi level (E_F) is positioned inside the valence band.^[27] The band gap (E_g), electron affinity (E.A.), and the ionization potential (I.P.) of Sb_2Te_3 ^[28] and the work function (Φ) of Pt nanocrystals^[29] are taken from bulk values. The equilibrium band diagram for Pt- Sb_2Te_3 nanocomposite is shown in Figure 6.3(b), indicating the formation of band-bending potential well at the interface where low energy holes are scattered more strongly than the high energy holes.^[10]

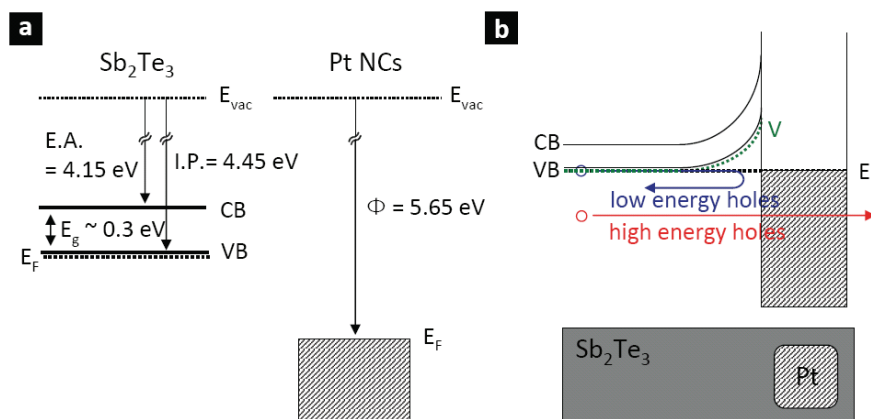


Figure 6.3 Band alignment in Pt-Sb₂Te₃ nanocomposites. (a) Band diagram of Sb₂Te₃ and Pt nanocrystals before contact. The bandgap (E_g), electron affinity (E.A.), and ionization potential (I.P.) of Sb₂Te₃ and the work function (Φ) of Pt are taken from bulk values. (b) Equilibrium band alignment of Sb₂Te₃ and Pt after contact. V in green dotted line indicates the band-bending potential induced at the interface.

The solutions of Sb₂Te₃ precursor crystallize into rhombohedral Sb₂Te₃ (JCPDS 015-0874) and pure hexagonal tellurium (JCPDS 036-1452) upon annealing at 200°C to remove excess and coordinating hydrazine. In order to obtain stoichiometric Sb₂Te₃, films have to be treated above 450°C,^[23] which induces alloying between nanocrystals and the semiconductor matrix. This detrimental process can be avoided by annealing only up to 200°C and soaking the film in a trioctylphosphine (TOP) solution overnight. TOP chemically dissolves elemental tellurium as shown by the absence of tellurium peaks in the power diffraction data (Figure 6.4(a)). Although, the diffraction arising from Pt nanocrystals could not be identified in the power diffraction due to low concentration, energy dispersive X-ray

(EDS) spectrum obtained from Pt-Sb₂Te₃ nanocomposite confirms that all Pt, Sb, and Te elements are present in nanocomposite films (Figure 6.4(b)). This critical step to preserve the structure and the composition of Pt nanocrystals, also recovers excess Te which can be reused to improve the atom efficiency of the reaction.

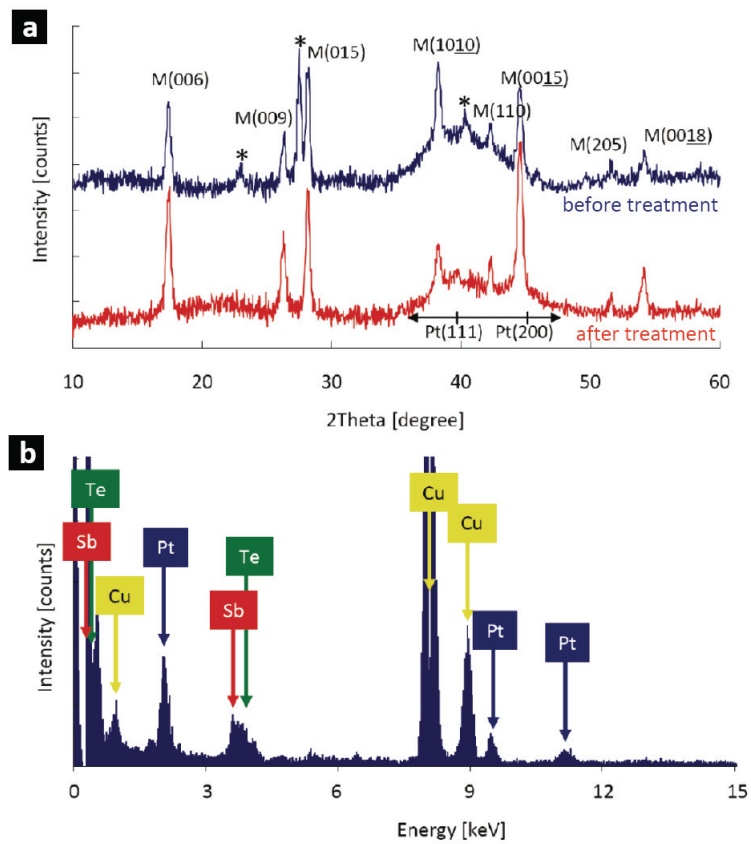


Figure 6.4 (a) Powder diffraction of Pt-Sb₂Te₃ nanocomposite before (blue) and after (red) TOP treatment. After TOP treatment, diffraction peaks arising from elemental Te, as indicated by black asterisk, disappear. Diffraction peaks arising from Pt nanocrystals cannot be identified due to low concentration. (b) EDX spectrum obtained from Pt-Sb₂Te₃ nanocomposite sample showing the presence of Pt, Sb, and Te elements.

Figure 6.5 shows the transmission electron microscope (TEM) image and selective area electron diffraction (SAED) of as-deposited, annealed (at 200°C), and TOP treated (after annealing) Pt-Sb₂Te₃ nanocomposites. The as-deposited sample shows Pt nanocubes surrounded with amorphous Sb₂Te₃. As the samples are heated to 200°C, Sb₂Te₃ crystallize and encapsulated Pt nanocrystals as depicted in Figure 6.5 (c) and (d). TEM images and SAED patterns confirm that, after TOP treatment, the identity of Pt nanocrystal inside crystalline Sb₂Te₃ is preserved.

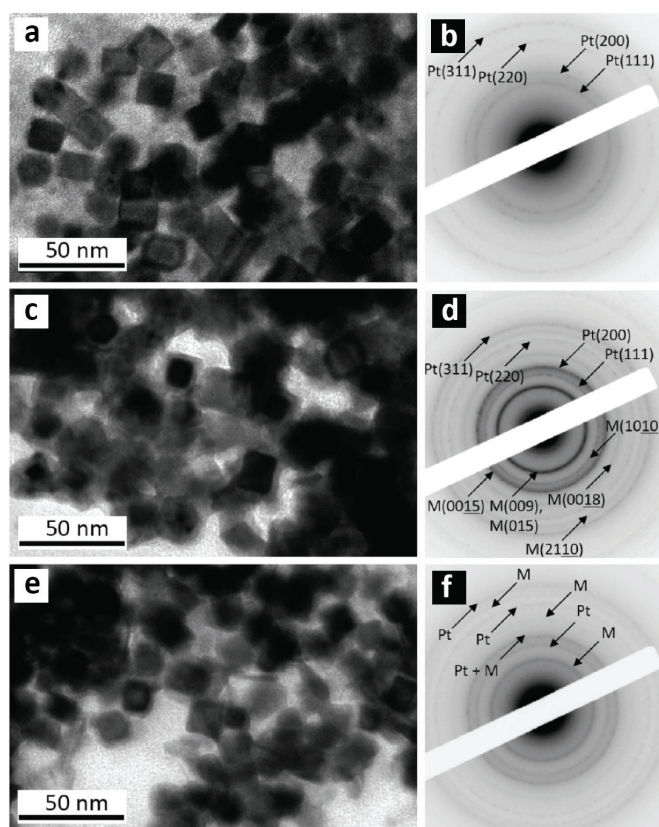


Figure 6.5. TEM micrographs (a, c, e) and SAED (b, d, f) of as-deposited (a, b), annealed (c, d), and TOP treated (e, f) nanocomposite samples. SAED in (b) only shows diffraction from Pt nanocrystals as indicated by black arrows. SAED in (d) shows additional Sb₂Te₃ patterns evolved after annealing and f shows pattern from both Pt and Sb₂Te₃ after TOP treatment.

Figure 6.6(a) shows the scanning electron microscope (SEM) image of the nanocomposite film dropcast on glass substrate for thermopower and Hall effect measurements. Thermopower measured on Pt-Sb₂Te₃ nanocomposites was compared with the films processed with the Sb₂Te₃ solution showing a 34% increase in thermopower (Figure 6.6(b)). It is also worthy to note the thermopower of 79 $\mu\text{V}/\text{K}$ in single crystal Sb₂Te₃ with the similar range in carrier concentration.^[30,31] Hall effect measurements performed on Pt-Sb₂Te₃ nanocomposites and Sb₂Te₃ films are shown in Table 6.1 and the determination of van der Pauw resistivity and Hall effect measurement accuracy in nanocomposite films is summarized in Table 6.2. For van der Pauw resistivity measurements, 1 mA of current was used to minimize the power dissipation (< 1 mW). The contact quality and the sample uniformity for the sheet resistivity measurements show less than 2% deviation (< 5% preferred). For Hall effect measurements, voltage offset (background voltage) and the carrier density uniformity indicates 6.3 % and 4.0 % deviation (< 5% preferred).

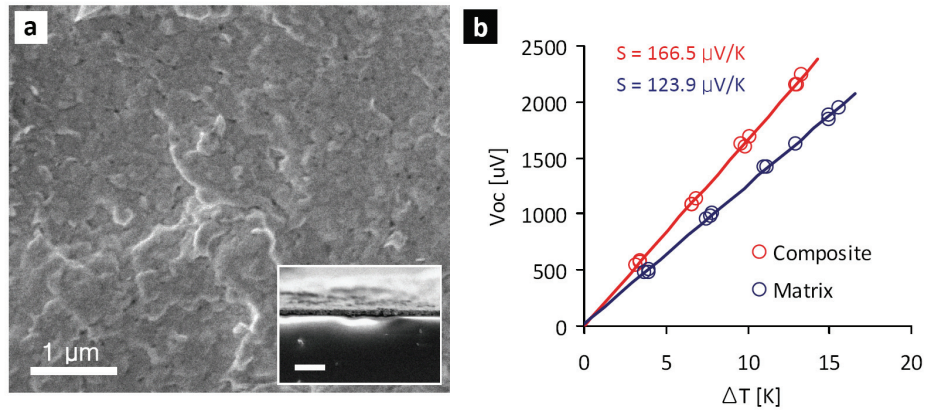


Figure 6.6. (a) SEM micrograph of Pt-Sb₂Te₃ nanocomposite. Inset show the cross section of the film with a scale bar of 5 μm. (b) Open-circuit voltage (V_{oc}) vs. temperature difference (ΔT) for composite and matrix samples. The slope of the linear fit gives the thermopower.

	Nanocomposite	Sb ₂ Te ₃
Resistivity [Ωcm]	$2.96 \times 10^{-2} \sim 4.41 \times 10^{-2}$	$1.33 \times 10^{-2} \sim 1.40 \times 10^{-2}$
Type of carriers	holes	holes
Carrier mobility [cm^2/Vs]	8.3 ~ 14.4	22.1 ~ 33.9
Carrier concentration [cm^{-3}]	$1.57 \times 10^{19} \sim 3.34 \times 10^{19}$	$1.31 \times 10^{19} \sim 2.03 \times 10^{19}$
Thermopower [$\mu\text{V}/\text{K}$]	136.8 ~ 166.4	107.3 ~ 123.8
Power factor at 300K [$\mu\text{W}/\text{cmK}^2$]	0.66 ~ 1.38	0.82 ~ 1.09

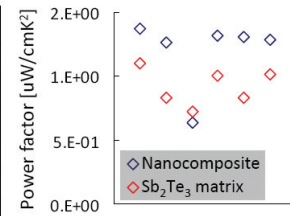


Table 6.1 Summary of van der Pauw resistivity, Hall effect, and thermopower measurements on Sb₂Te₃ matrix and Pt-Sb₂Te₃ nanocomposite at room temperature. Composite materials show lower hole mobility and higher thermopower than the matrix material, due to filtering of low energy holes. Carrier concentration is slightly increased in the nanocomposite compensating for the increase in resistivity due to mobility reduction. Higher power factor is achieved in Pt-Sb₂Te₃ nanocomposites. The plot on the right shows the power factor obtained from 6 nanocomposite and 6 Sb₂Te₃ matrix samples.

Compared to the Sb₂Te₃ film, the nanocomposite sample shows a 1.5- to 4-fold reduction in mobility, indicating that the introduction of Pt nanocrystals scatter holes. Interestingly, introducing Pt nanocrystal also slightly increases the carrier concentration (up to 2.5 times). This could be due to an overlap of band-bending

potential between Pt nanocrystals.^[10] This increases the distance between the Fermi energy level (positioned inside the valence band) and the valence band of Sb_2Te_3 , thereby increasing the total concentration of holes in the semiconductor matrix. Although the introduction of Pt nanocrystals increases the resistivity in nanocomposites, the increase in carrier concentration partially compensates for the reduction in mobility. Thus, the thermoelectric power factor ($S^2\sigma$) at room temperature showed an increase up to 1.7 times that of Sb_2Te_3 films. In addition to the increase in power factor, significant reduction in thermal conductivity is also expected in nanocomposites, which further increases ZT. Introduction of nanocrystals with a given size and distribution may selectively scatter mid- to long-wavelength phonons which transport a large fraction of heat.^[3] Engineering the shape of the nanocrystals may also illuminate how the thermal resistance is affected by the interfacial properties between nanocrystals and the matrix.

VAN DER PAUW RESISTIVITY				HALL EFFECT			
I12	I23	I34	I41	I13	I24	I13	I24
9.99450E-04	9.99450E-04	9.99560E-04	9.99520E-04	9.99520E-04	9.99600E-04	9.99600E-04	9.99560E-04
V43	V14	V21	V32	V24	V31	V24	V31
3.94780E-02	2.50740E-02	3.95310E-02	2.53140E-02	-1.40330E-02	1.44260E-02	-1.43870E-02	1.44770E-02
I21	I32	I43	I14	I31	I42	I31	I42
-1.00000E-03	-1.00000E-03	-1.00010E-03	-1.00010E-03	-1.00010E-03	-1.00010E-03	-1.00010E-03	-1.00010E-03
V34	V41	V12	V23	V42	V13	V42	V13
-3.91730E-02	-2.53790E-02	-3.91150E-02	-2.51420E-02	1.40340E-02	-1.39520E-02	1.44240E-02	-1.40230E-02
				FIELD +6569.9		FIELD -6463.4	
R12/43	R23/14	R34/21	R41/32	R/B1=R13/24p - R13/24n			
3.94997E+01	25.08779829	3.95484E+01	25.32615656	8.98299E-05			
R21/34	R32/41	R43/12	R14/23	R/B2=R24/31p - R24/31n			
3.91730E+01	2.53790E+01	3.91111E+01	2.51395E+01	-4.41785E-05			
				R/B3=R31/42p - R31/42n			
				9.55277E-05			
				R/B4=R42/13p - R42/13n			
				-4.59721E-05			
				OFFSET AND CARRIER DENSITY UNIFORMITY			
				R/B1 = R/B3	R/B2 = R/B4		
				6.34289E+00	4.06000E+00		
				CARRIER TYPE	holes		
				MOBILITY	8.2564	[cm ² /V-s]	
				SHEET CARRIER D.	5.24E+15	[/cm ²]	
				CARRIER DENSITY	3.08E+19	[/cm ³]	
CONTACT QUALITY							
R12/43=R21/34	R23/14=R32/41	R34/21=R43/12	R41/32=R14/32				
0.827157277	1.160730438	1.105765065	0.737066058				
SAMPLE UNIFORMITY							
R12/43 + R21/34=R34/21 + R43/12							
1.68224E-02							
R23/14 + R32/41=R41/32 + R14/23							
2.28999E-03							
FILM THICKENSS	1.71	[μm]					
SHEET RESISTIVITY	1.44E+02	[Ohm/sq]					
RESITIVITY	2.45E-02	[Ohm-cm]					

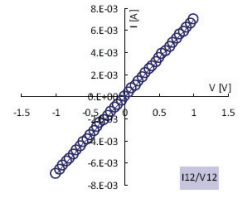


Table 6.2. Summary of measurement data for a van der Pauw resistivity and Hall effect measurement on nanocomposite films. *I12* indicates constant DC current between contact 1 and 2, *V12* denotes DC voltage measured between contact 1 and 2, and $R12/43 = V43 / I12$. $R13/24p$ denotes $V24 / I13$ divided by positive magnetic field (6569.9 G) and $R13/24n$ indicates $V24 / I13$ divided by negative magnetic field (-6463.4 G). Contact quality, sample uniformity, offset, and carrier density uniformity was assessed following the guidelines provided by NIST.^[32] I-V plots on the lower right show that Ohmic contacts are made between silver and nanocomposite film.

6.4 Conclusion

Nanocomposites where Pt nanocrystals are embedded in *p*-type Sb_2Te_3 matrices were obtained by facile fabrication through solution-process. A critical step in preserving the structure and the composition of Pt nanocrystals is the use of a TOP treatment to obtain a stiochiometric semiconductor matrix. The introduction of Pt

increases thermopower through filtering of low energy carriers while minimizing the reduction in electrical conductivity and thus, an enhancement of the power factor was achieved. The ability to choose different composition, size, shape, and concentration of nanocrystals and embedding them either in n-type or p-type semiconductor matrices provide the possibility of engineering both the carrier energy and phonon spectra to identify thermoelectric nanocomposites with $ZT > 1$.

References

1. Szczech, J. R.; Higgins, J. M.; Jin, S. Enhancement of the Thermoelectric Properties in Nanoscale and Nanostructured Materials. *J. Mater. Chem.* **2011**, *21*, 4037-4055.
2. Kanatzidis, M. G. Nanostructured Thermoelectrics: The New Paradigm? *Chem. Mater.* **2010**, *22*, 648-659.
3. Minnich, A. J.; Dresselhaus, M. S.; Ren, Z. F.; Chen, G. Bulk Nanostructured Thermoelectric Materials: Current Research and Future Prospects. *Energy Environ. Sci.* **2009**, *2*, 466-479.
4. Snyder, G. J.; Toberer, E. S. Complex Thermoelectric Materials. *Nature Mater.* **2008**, *7*, 105-114.
5. Medlin, D. L.; Snyder, G. J. Interfaces in bulk Thermoelectric Materials: A Review for Current Opinion in Colloid and Interface Science. *Curr. Opin. Colloid Interface Sci.* **2009**, *14*, 226-235.
6. Moyzhes, B.; Nemchinsky, V. Thermoelectric Figure of Merit of Metal-Semiconductor Barrier Structure Based on Energy Relaxation Length. *Appl. Phys. Lett.* **1998**, *73*, 1895.
7. Nishio, Y.; Hirano, T. Improvement of the Efficiency of Thermoelectric Energy Conversion by Utilizing Potential Barriers. *Jpn. J. Appl. Phys.* **1997**, *36*, 170-174.
8. Popescu, A.; Woods, L. M.; Martin, J.; Nolas, G. S. Model of Transport Properties of Thermoelectric Nanocomposite Materials. *Phys. Rev. B* **2009**, *79*, 205302
9. Vashaee, D.; Shakouri, A. Improved Thermoelectric Power Factor in Metal-Based Superlattices. *Phys. Rev. Lett.* **2004**, *92*, 106103.

10. Faleev, S. V.; Léonard, F. Theory of Enhancement of Thermoelectric Properties of Materials with Nano-inclusion. *Phys. Rev. B* **2008**, *77*, 214304.
11. Zide, J. M. O.; Vashaee, D.; Bian, Z. X.; Zeng, G.; Bowers, J. E.; Shakouri, A.; Gossard, A. C. Demonstration of Electron Filtering to Increase the Seebeck Coefficient in $\text{In}_{0.53}\text{Ga}_{0.47}\text{As}/\text{In}_{0.53}\text{Ga}_{0.28}\text{Al}_{0.19}\text{As}$ Superlattices. *Phys. Rev. B* **2006**, *74*, 205335.
12. Zide, J. M. O.; *et al.* High Efficiency Semimetal/Semiconductor Nanocomposite Thermoelectric Materials. *J. Appl. Phys.* **2010**, *108*, 123702.
13. Heremans, J. P.; Thrush, C. M.; Morelli, D. T. Thermopower Enhancement in Lead Telluride Nanostructures. *Phys. Rev. B* **2004**, *70*, 115334.
14. Martin, J.; Wang, L.; Chen, L.; Nolas, G. S. Enhanced Seebeck Coefficient Through Energy-Barrier Scattering in PbTe Nanocomposites. *Phys. Rev. B* **2009**, *79*, 115311.
15. Paul, B.; V, A. K.; Banerji, P. Embedded Ag-Rich Nanodots in PbTe: Enhancement of Thermoelectric Properties Through Energy Filtering of the Carriers. *J. Appl. Phys.* **2010**, *108*, 064322.
16. Heremans, J. P.; Thrush, C. M.; Morelli, D. Thermopower Enhancement in PbTe with Pb Precipitates. *J. Appl. Phys.* **2005**, *98*, 063703.
17. Sootsman, J. R.; Kong, H.; Uher, C.; D'Angelo, J. J.; Wu, C. -I.; Hogan, T. P.; Caillat, T.; Kanatzidis, M. G. Large Enhancement in the Thermoelectric Power Factor of Bulk PbTe at High Temperature by Synergistic Nanostructuring. *Angew. Chem. Int. Ed.* **2008**, *47*, 8618-8622.
18. Mitzi, D. B. Solution Processing of Chalcogenide Semiconductors via Dimensional Reduction. *Adv. Mater.* **2009**, *21*, 3141-3158.
19. Mitzi, D. B.; Kosbar, L. L.; Murray, C. E.; Copel, M.; Afzali, A. High-Mobility Ultrathin Semiconducting Films Prepared by Spin Coating. *Nature*, **2004**, *428*, 299-303.
20. Mitzi, D. B.; Yuan, M.; Liu, W.; Kellock, A. J.; Chey, S. J.; Deline, V.; Schrott, A. G. A High-Efficiency Solution-Deposited Thin-Film Photovoltaic Device. *Adv. Mater.* **2008**, *20*, 3657-3662.
21. Milliron, D. J.; Raoux, S.; Shelby, R. M.; Jordan-Sweet, J. Solution-Phase Deposition and Nanopatterning of GeSbSe Phase-Change Materials. *Nature Mater.* **2007**, *6*, 352-356.
22. Kang, Y.; Ye, X.; Murray, C.B. Size- and Shape-Selective Synthesis of Metal Nanocrystals and Nanowires Using CO as a Reducing Agent. *Angew. Chem. Int. Ed.* **2010**, *49*, 6456-6159.
23. Kovalenko, M. V.; Spokoyny, B.; Lee, J.-S.; Scheele, M.; Weber, A.; Perera, S.; Landry, D.; Talapin, D. V. Semiconductor Nanocrystals Functionalized with Antimony Telluride Zintl Ions for Nanostructured Thermoelectrics. *J. Am. Chem. Soc.* **2010**, *132*, 6686-6695.
24. Kovalenko, M. V.; Scheele, M.; Talapin, D. V. Colloidal Nanocrystals with Molecular Metal Chalcogenide Surface Ligands. *Science*, **2009**, *324*, 1417-1420.

25. Rowe, D. M. Review: Thermoelectric Waste Heat Recovery as a Renewable Energy Source. *Int. J. Innov. Eng. Sys. Power.* **2006**, *1*, 13-23.
26. Tangirala, R.; Baker, J. L.; Alivisatos, A. P.; Milliron, D. L. Modular Inorganic Nanocomposite by Conversion of Nanocrystal Superlattices. *Angew. Chem. Int. Ed.* **2010**, *49*, 2878-2882.
27. Kulbachinskii, V. A.; Dashevskii, Z. M.; Inoue, M.; Sasaki, M.; Negishi, H.; Gao, W. X.; Lostak, P.; Horak, J.; de Visser, A. Valence-band Changes in $\text{Sb}_{2-x}\text{In}_x\text{Te}_3$ and $\text{Sb}_2\text{Te}_{3-y}\text{Se}_y$ by transport and Shubnikov-de Hass Effect Measurements. *Phys. Rev. B* **1995**, *52*, 10915-10922.
28. Martin, M. A.; Aliyu, M. M.; Quadery, A. H.; Amin, N. Prospects of Novel Front and Back Contacts For High Efficiency Cadmium Telluride Thin Film Solar Cells From Numerical Analysis. *Sol. Energ. Mat. Sol. C.* **2010**, *94*, 1496-1500.
29. Lide, D. R. *CRC Handbook of Chemistry and Physics*, CRC Press, 2008.
30. Drašar, Č.; Steinhart, M.; Lošťák, P.; Shin, H. -K.; Dyck, J. S., Uher, C. Transport Coefficients of Titanium-Doped Sb_2Te_3 Single Crystals. *J. Solid State Chem.* **2005**, *178*, 1301-1307.
31. Dhar, S. N.; Desai, C. F. Sb_2Te_3 and $\text{In}_{0.2}\text{Sb}_{1.8}\text{Te}_3$: A Comparative Study of Thermoelectric and Related Properties. *Phil. Mag. Lett.* **2002**, *82*, 581-587.
32. Hall Effect Measurements, *The National Institute of Standards and Technology*, Physical Measurement Laboratory, (<http://www.nist.gov/pml/semiconductor/hall.cfm>)

7. Conclusion and future work

7.1 Conclusion

In this thesis, we have studied energy (charge and heat) transport and conversion in semiconductor nanocrystal solids. This work focuses on the measurement and the interpretation of temperature-dependent thermopower and electrical conductivity of PbTe and Ag₂Te nanocrystals as well as PbTe nanocrystal solids doped with Ag₂Te nanocrystals. The main results are presented in the following categories.

1. The slope of the thermopower versus inverse temperature plot obtained from PbTe nanocrystal solids reveals the Fermi energy level with respect to the transport energy which is key in estimating the carrier concentration in semiconductors.
2. The y-intercept of the thermopower versus inverse temperature plot obtained from PbTe nanocrystal solids reflects the sharpness of the electronic density of state distribution. This reveals the origin of enhanced thermopower in nanostructures with modified density of states compared to that of the bulk.

3. Temperature-dependent conductivity combined with thermopower measurements were performed on each of the PbTe and Ag₂Te nanocrystal solids to reveal the Fermi energy level and the energetic disorder affecting the carrier mobility.

4. Temperature-dependent conductivity combined with the thermopower measurement were performed on PbTe nanocrystal solids mixed with Ag₂Te nanocrystal dopants. Increasing the concentration of nanocrystal dopants decreased the distance between the Fermi level and the first hole transport level (increase in hole concentration), and increased the activation energy of hopping (decrease in hole mobility).

Another scope of this thesis focuses on the development of solution-processable nanocomposite with enhanced thermopower via carrier energy filter. The conclusions are summarized in the following.

1. Nanocomposites composed of Pt nanocrystals embedded in a hydrazine-based solution-processable Sb₂Te₃ semiconductor demonstrated an increase in thermopower due to carrier energy filtering.

2. Thermopower, van der Pauw resistivity and Hall effect measurements reveal an increase in the thermoelectric power factor in Pt-Sb₂Te₃ nanocomposites compared to that of the pure Sb₂Te₃ film.

3. The above work highlights the ability to choose different composition, size, shape, and concentration of nanocrystals and embedding them either in *n*- or *p*-type semiconductor matrices to engineer both the carrier energy and phonon spectra with the ease of material processing.

7.2 Future work: Electronic contributions to the thermal conductivity

Electrons and holes, which are both charge and heat carriers, affect three primary material parameters: electrical conductivity (charge), thermoelectricity (charge and heat), and thermal conductivity (heat). In previous chapters, we have theoretically and experimentally explored the first two terms in semiconductor nanocrystal solids. As a last discussion of this thesis, we will focus on the electronic contribution to the thermal conductivity. In metals or degenerate semiconductors, the electronic thermal conductivity (k_e) is related the electrical conductivity (σ) by the

Lorentz number ($L = \pi^2 k_B^2 / 3e^2 = 2.45 \times 10^{-8} \text{ W}\Omega\text{K}^{-2}$). This is known as the Widemann-Franz law ($k_e = L\sigma T$) which is commonly applied to bulk thermoelectric materials to extract the electronic contribution to the thermal conductivity. However, in nanostructures with a sharp distribution of density of states, the Lorentz number can significantly deviate from the theoretical value and the Widemann-Franz law loses its validity.^[1] This is shown in an ideal electronic structure, as depicted in Figure 7.1(a), where the high energy portion of electrons that carries large amounts of heat are cut-off due to the discontinuity of the density of states and therefore no longer contributes to the thermal conductivity.^[2] An accurate theoretical method to estimate or an experimental method to practically measure electronic thermal conductivity may, in combination with the strategy to achieve lowest lattice thermal conductivity, lead to a design of an efficient thermoelectric material.

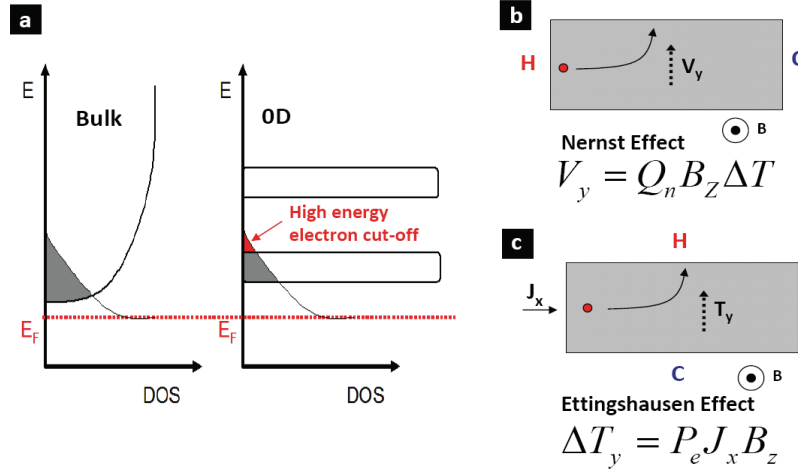


Fig. 7.1 Failure of Wiedemann-Franz law and alternative methods to extract electronic thermal conductivity. (a) Schematic description of electron population in 3D and 0D material systems. Schematic illustration of (b) the Nernst and (c) the Ettingshausen effect.

One method, proposed as a future work of this thesis, is to directly measure the electronic thermal conductivity exclusively via the Nernst and Ettingshausen effects. The Nernst effect arises from the combination of Seebeck and Hall effects. When the charge carriers thermally diffuse due to an applied temperature difference, an applied external magnetic field (B_z) deflects the carrier perpendicular to the direction of the current flow, causing the build up of an electric field. This electric field is proportional to the applied temperature gradient (ΔT) as well as the magnetic field (B_z) and the proportional constant is defined as Nernst coefficient, Q_n in $V_y = Q_n B_z \Delta T$. Similarly, the Ettingshausen effect is induced when the current is applied in the presence of a magnetic field. The deflected carrier causes a temperature gradient perpendicular to the current flow, given by the equation: $\Delta T_y = P_e J_x B_z$. The

proportional constant P_e is the Ettingshausen coefficient. These two effects are shown in Fig. 7.1(b) and (c). The Nernst and Ettingshausen coefficients are related through the Bridgeman relationship as $P_e k_e = Q_n T$, where k_e is the electronic thermal conductivity. Through measurements of these two magneto-thermal effects, electronic contribution to thermal conductivity can be directly extracted.

Reference

1. Minnich, A. J.; Dresselhaus, M. S.; Ren, Z. F.; Chen, G. Bulk Nanostructured Thermoelectric Materials: Current Research and Future Prospects. *Energy Environ. Sci.*, **2009**, *2*, 466-479.
2. Humphrey T. E.; Linke, H. Reversible Thermoelectric Nanomaterials, *Phys. Rev. Lett.*, **2005**, *94*, 096601.